Università degli Studi di Torino

PhD Programme in Chemical and Materials Sciences XXXII Cycle

Aluminum alloys for Additive Manufacturing: alloys microstructure, rapid solidification processes, testing of products

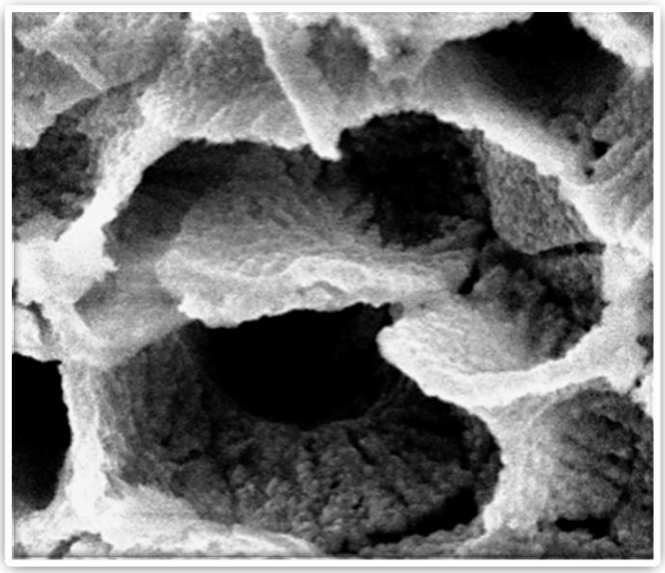

Silvia Marola

Supervisor:
Prof. Livio Battezzati

Università degli Studi di Torino

PhD Programme in Chemical and Materials Sciences XXXII cycle

Aluminum alloys for Additive Manufacturing: alloys microstructure, rapid solidification processes, testing of products

Candidate: **Silvia Marola**

Supervisor: Prof. **Livio Battezzati**

Jury Members: Prof. **Jürgen Eckert**
Montanuniversität Leoben
Department of Materials Physics

Prof. **Riccardo Casati**
Politecnico di Milano
Dipartimento di Meccanica

Prof. **Marcello Baricco**
Università di Torino
Dipartimento di Chimica

Head of the Doctoral School: Prof. Alberto Rizzuti
PhD Programme Coordinator: Prof. Mario Chiesa

Torino, 2019

Contents

Preface

This work refers to part of the research activities performed in the framework of the STAMP (Sviluppo Tecnologico dell'Additive Manufacturing in Piemonte) project. This project, funded by Regione Piemonte, started in 2016 and encompassed the collaboration of 26 partners coming from both industrial and academic facilities present in the region. The aim of STAMP was to promote Additive Manufacturing technologies in the area by considering the whole production process starting from design and material selection of components to machines, control and standardization of the process.

Aluminum alloys were suggested for the project by the industrial partners. In particular, the focus of Università di Torino, in collaboration with the other research groups (Politecnico di Torino and Istituto Italiano di Tecnologia), was to develop new compositions specifically selected for Additive Manufacturing.

In this framework, in this thesis the topic of material selection was faced trying to understand at first which is the behaviour of conventional Al alloys when subjected to the high cooling rates occurring during the Additive Manufacturing processes. Once obtained an in-depth knowledge of the solidification mechanism, what was done was to propose new compositions along with a new route to test materials reducing both the amount of material and the time necessary for the testing. In the end, the presence of residual stresses in components produced by Additive Manufacturing was evaluated using both conventional and unconventional non-destructive techniques.

The thesis begins with a short introduction giving the principal information on Additive Manufacturing, rapid solidification and Aluminum alloys and deepening the main topics faced during these three years. Then the rapid solidification processes and experimental procedure employed are described, moving then to the description of the various research topics encountered. In Part I the solidification mechanism of a commercial AlSi10Mg alloy is defined through the comparison of what obtained with

other rapid solidification techniques. In Part II a new route to test new compositions studied specifically for Additive Manufacturing is proposed along with some modification of the AlSi10Mg alloy that will improve its mechanical properties. In Part III residual stresses present in rapidly solidified samples are investigated using two non-destructive techniques, X-Ray Diffraction and Raman spectroscopy. In conclusion, an overall summary of the results obtained in the thesis is drawn along with some future perspectives.

1. Introduction

1.1. Additive Manufacturing

The term Additive Manufacturing (AM) refers to a group of innovative technologies developed in the last thirty years taking inspiration from the progress of rapid prototyping, more precisely the StereoLithographic Apparatus (SLA) patented in 1984 [1].

The first research activities directly related with metal AM were conducted on polymeric laser powder-bed systems and led to patent Selective Laser Sintering (SLS) in 1986. The first 3D printed metallic part was produced in 1990 by Manriquez-Frayre and Bourell using SLS. Starting from this year, thanks to the development of laser sources, it was possible to achieve complete melting of the metallic powders in the powder bed, for this reason nowadays the techniques employed for the production of metallic components are commonly referred as Selective Laser Melting (SLM) [2].

In ***Fig. 1.1*** are reported the most significative events that led to the development of metal AM, further details can be found elsewhere [3].

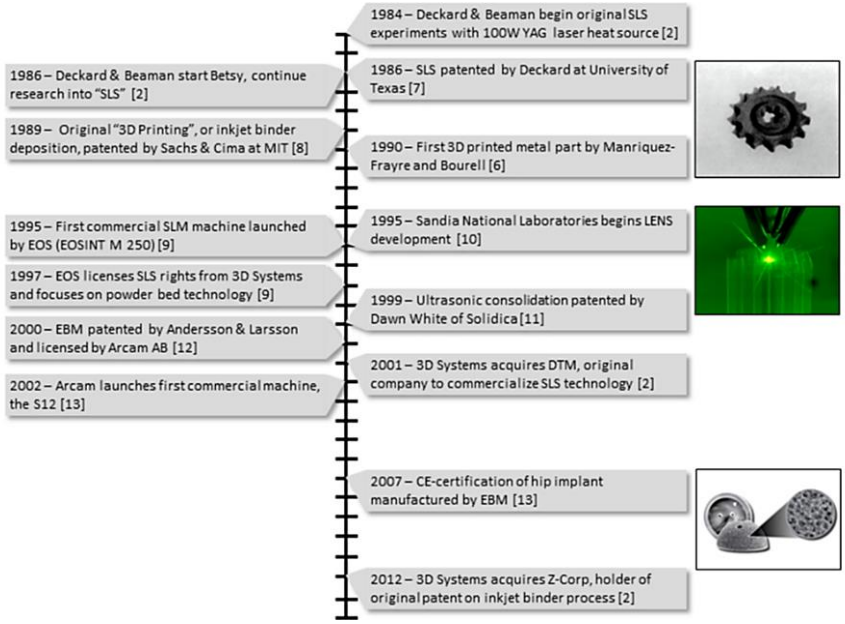

Fig. 1.1 *Development of metal AM through its significant events [2].*

Currently AM is defined as:

"a process of joining materials to make objects from 3D model data, usually layer upon layer, as opposed to subtractive manufacturing methodologies" [4].

The feedstock material used to produce the 3D object can be found in form of powder, wires or sheets according to the production process employed. In particular, in [4] the four classes of machines associated to the production of metallic components are identified:

- Powder Bed Fusion (PBF);
- Direct Energy Deposition (DED);
- Binder Jetting;
- Sheet lamination.

In PBF processes a focused energy source (either laser or electron beam) selectively melts in a layer by layer fashion the powders previously spread on a building platform according to a CAD (Computer Aided Design) model.
Similarly, in DED it is possible to use laser or electron beam as energy input, however in this case the feedstock is provided, either in form of powder or wire, directly into the melt pool.
Binder jetting is basically a powder metallurgy (PM) process in which a binder is deposited on the metal powder, then the part is cured in such a way that the powders are hold together and, in the end, sintered to obtain the final component.
Sheet lamination consists in stacking 2D slices adhesively or metallurgically to form a 3D component.
In this work, attention will be focused on PBF processes employing laser as energy source.
The step necessary to produce a final component with AM technologies along with a schematic representation of a Laser-Powder Bed Fusion (L-PBF) machine are represented in ***Fig. 1.2.***

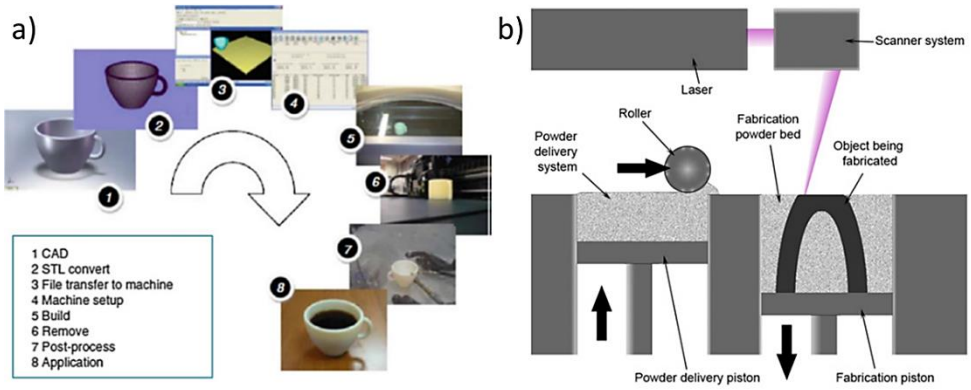

Fig. 1.2 *Steps that lead to the production of a 3D component [6] with AM (a) and a schematic representation of a L-PBF machine (b) [1].*

As clearly visible from ***Fig. 1.2-a*** several steps are required to obtain the object ready for the final application. Firstly, the part must be designed to obtain a CAD model whereby a .stl file (STereoLithography file) is created. At this stage generally the support structures, fundamental to hold unsupported geometries and prevent the distortion of the part, are generated with a dedicated software. The complete build file, including both the part and the supports, is then sliced in layers of the desired thickness and sent to the machine software. In the early stages of the process, powders are sieved and fed into the dispenser in the building chamber, that is usually filled with an inert gas to maintain a controlled level of Oxygen, fundamental to avoid formation of defects due to the presence of oxides.

Once the process is started, the metallic powders are spread with a blade on the building platform, usually made of an alloy similar to that of the job in progress, that can be preheated at different temperatures. A high-power laser selectively melts the powders belonging to the sliced CAD data layer. Once the first layer is completed the building platform drops down one layer in thickness, is recoated with new powder and the process is repeated until the entire job is completed, as schematically drawn in ***Fig. 1.2-b***.

At the end of the job, all the unmolten powder particles must be removed in order to detach the finished part from the building platform and perform the post processing treatments required for the final application [5,6].

L-PBF is known to give a great freedom in design with respect to conventional manufacturing routes, allowing to produce near-net shape components with high accuracy and detail resolution, sufficiently good surface quality and mechanical properties. The great freedom in design of this technique allows the production of objects having complex shapes or internal features difficult, if not impossible, to produce by means of conventional manufacturing routes, moreover complex geometries and assemblies can be simplified.

Despite the advantages associated with Additive Manufacturing routes, it is important to keep in mind also the drawbacks of the process. First, it is important to consider that even if AM can provide great flexibility in design there are still limitations in what can be produced, e.g. minimum wall thickness, dimension of the internal channels and positioning of support structures. Moreover, as clear from the several steps involved in the production, a lot of work is necessary both before and after the job to obtain the final component. So, due to the complexity of the process, the collaboration of several experts is required to obtain the best result possible in terms of design, quality of the final part and mechanical properties.

The main process parameters that can be adjusted to improve the quality of the final component are the laser power, the scanning speed, the hatch spacing and the layer thickness [7], these are shown schematically in ***Fig. 1.3***.

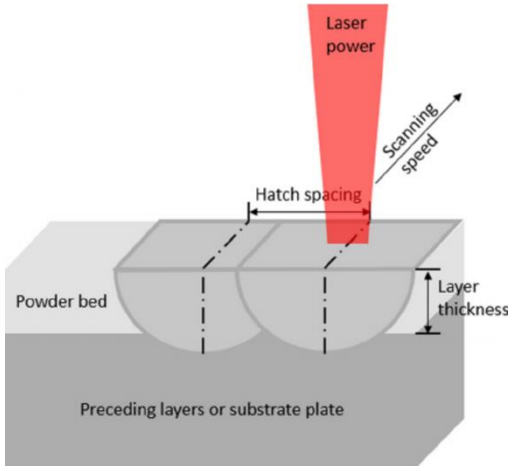

Fig. 1.3 *L-PBF main processing parameters [7].*

It is worth to keep in mind that even if AM processes are defined as fast, the part is produced by melting thin layers of material; so, depending on the final height of the component, the production can take days or even weeks to be completed. This, in addition with the high cost of both machinery and feedstock material, makes the process expensive in comparison with conventional manufacturing routes.

This is why the main fields of application for these processes are the automotive, aerospace and biomedical ones in which the strong necessity of complex shapes is supported by a consistent economic investment [8].

Different kind of materials are processable by AM technologies, however it is important to select the best processing route for every specific material. The most widespread alloys for L-PBF are Titanium alloys, Cobalt-Chromium alloys, Stainless steels, Nickel-based superalloys and Aluminum alloys. A list of the most known alloys processable by L-PBF is reported in ***Table 1.1*** along with some references.

Table 1.1 *Overview of the most employed alloys in L-PBF.*

Family	***Alloy***	***References***
Aluminum	*Al-Si alloys*	*[9–21]*
	A6061	*[22]*
	A2024	*[23]*
	Scalmalloy	*[24–30]*
	Al-Cu	*[31]*
Cobalt-Chrome	*Co-Cr*	*[32–34]*
Copper	*Copper*	*[35]*
	Bronze	*[36]*
Gold	*Gold*	*[37]*
Nickel Superalloys	*Inconel 718*	*[38,39]*
	Inconel 625	*[40,41]*
	Hastelloy X	*[42]*
Steels	*Stainless steel 316L*	*[43–48]*
	Stainless steel GP1	*[49]*
	Stainless steel PH1	*[50,51]*
	Stainless steel CX	*[52]*
	Maraging steel MS1	*[53–56]*
Titanium	*Ti6Al4V*	*[57–62]*

The defects that can be found in components produced by AM are widely studied in the literature [1,2,8,63,64]. In ***Fig. 1.4*** a flow chart representing how the basic input parameters can influence defects formation and affect the final component produced by AM is reported.

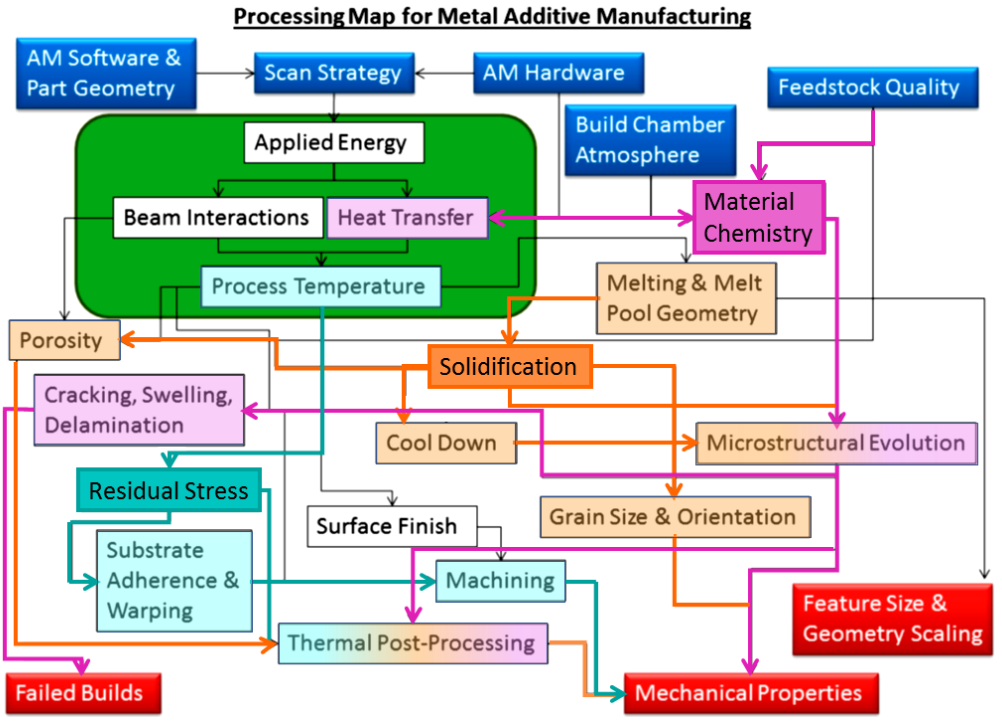

Fig. 1.4 *How input parameters affect defects formation and final properties of the components processed by AM [2].*

The most common defects encountered in samples produced by AM can be divided in compositional, microstructural or dimensional defects. An overview of the different defects encountered is reported in ***Fig. 1.5***.

The different volatility of the alloying elements plays a fundamental role in the formation of compositional defects. In fact, during the process, the molten pool can reach sufficiently high temperatures to cause a significant evaporation of the most volatile elements in the alloy. The compositional change associated to the selective evaporation can lead to alteration both in the solidification process and in the properties intimately related to the composition of the alloy (as corrosion resistance or specific mechanical properties). To avoid the excessive evaporation of alloying elements, it is

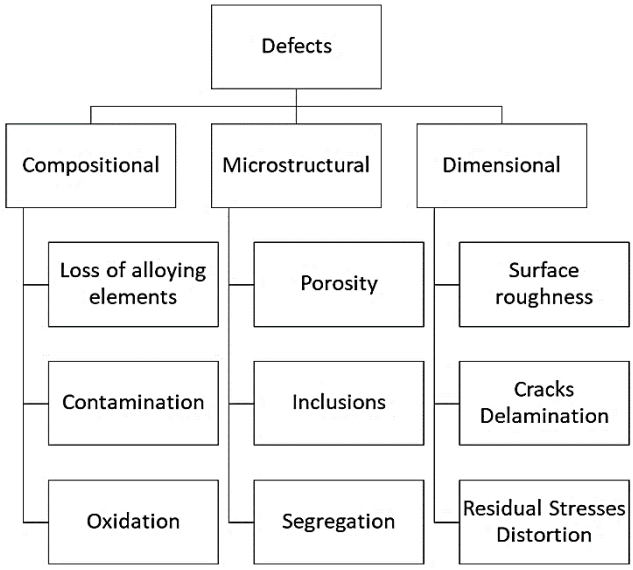

Fig. 1.5 *Overview of defects that can be encountered in parts produced by AM.*

necessary to control adequately the process parameters that influence geometry and temperature of the molten pool (e.g. laser power, scanning speed, laser spot size…).

Obviously, to avoid compositional defects, it is necessary to avoid contaminations that can occur both because of incorrect storage of the powders and during the production process.

To avoid contaminations during the production process, it is necessary to verify that there are no powder residues deriving from a previous job, especially if different alloys were employed, and that there is no interaction between the alloy to be processed and the inert gas employed during the process (especially if the selected gas is N_2).

Oxidation is the more significant compositional defects, it can occur when the melt pool or the powder are not correctly shielded from humidity and air. The presence of oxidation, as that of other compositional defects, can be limited through regular maintenance of the AM machine and correct control of both feedstock and process parameters employed for part production.

Other common defects that can be found in components produced by AM are the microstructural defects (porosities, cracks and elemental segregation). It is important to reduce or eliminate these defects since they ruin the mechanical properties of the alloys.

Talking about porosities in additively manufactured samples, three types of pores can be distinguished: keyhole pores, gas pores and pores deriving from lack of fusion. Keyhole pores can be found when employing high power density and derive from an instability of the process. These porosities can show different shapes and dimensions according to the process parameters employed and can contain gases or alloy vapours. When porosities contain gases or alloy vapours, they can become spherical in shape and are classified as gas pores. The gases not directly coming from evaporation of alloying elements can be related both to the presence of gases entrapped in the powders during the atomization process and to inclusion in the alloy of the inert gas employed during the process to avoid oxidation. The last type of porosity that can be found in samples produced by AM derives from the lack of fusion of parts of alloy principally because of the inadequate penetration of the molten pool in the substrate or in the layers previously deposited. Pores deriving from lack of fusion generally have elongated shapes and large dimensions that can cause stress concentration at the edges of the pores. In some cases, unmolten powder particles can be found inside these pores. The level of porosities in the alloy, as well as the level of other defects, can be controlled through a careful control of the process parameters employed during the production process.

Due to the high thermal gradients arising during the process, components produced by AM display a homogeneous microstructure on the macroscopic scale and a non-homogeneous microstructure on the micrometric scale; and often if during the production a mixture of different powders is employed, instead of pre-alloyed powders, segregation of some elements can be found in melt pools [31,65,66]. Obviously, segregation of some elements can negatively affect the mechanical properties of the alloy.

One of the most evident defects of additively manufactured components is the low surface finish. Roughness can be due to several causes such as feedstock material, geometry of the part and process parameters and be related to partially melted powder particles, incomplete fusion of the layer or “stair step” effect. The “stair step” effect is caused by the approximation obtained when trying to reproduce layer by layer a curved or inclined surface.

Surface roughness reduction depends on the interaction of several parameters. For this reason, it is necessary to optimize the process parameters for every machine and alloy employed.
Because of the high thermal gradients arising during the process, components produced by AM can have cracks, delamination and distortion. All these defects have a catastrophic effect on the final components and can be related to the presence of non-uniform residual stresses in the alloys.
In components produced by AM it is possible to distinguish three types of cracks. Solidification cracks can be found along grain boundaries and are formed mainly because of residual stresses due to contractions induced both thermally and by alloy shrinkage during solidification. Liquation cracking can be found in partially melted areas. The fast heating of the alloy below the *liquidus* temperature may cause precipitation along grain boundaries. During cooling, in the partially molten zones tensional stresses occur making precipitates to act as crack initiator. The third typology of cracks is delamination, that consists in the detachment of two consecutive layers because of the elevated residual stresses occurring during the additive process in between them.
Apart from being responsible of cracks formation in materials processed by AM, residual stresses can also induce distortions of the components leading to a loss of geometric tolerances and ruining the performances of the final part. To avoid the formation of excessive residual stresses is necessary to control carefully the process parameters and the position of support structures in such a way to minimize distortions. Control of process parameters is required to reduce the thermal gradient developing from the fast laser-material interaction, while the presence of support structures is required to hold unsupported geometries and again reduce the rate of thermal extraction from the molten pool.
Materials processed by L-PBF display some common features:

- the microstructure is a combination of small grains, non-equilibrium phases and new chemical compounds, such as metastable intermetallics, that are formed during the process;

- parts produced by L-PBF can exhibit better mechanical properties with respect to wrought products due to their finer microstructure and the formation of non-equilibrium phases;
- since parts are produced along specific directions the final products display some anisotropy;
- re-melting and solidifying of the previously melted layers can cause distortion of the part and residual stresses with the need of performing stress relieving treatments;
- surface roughness of parts produced by L-PBF is higher than that of conventionally produced parts; in particular, surface roughness of vertical surfaces is lower than that of curved, inclined or top ones. To reduce the surface roughness secondary operations, e.g. shot peening, machining, abrasive jet machining, are necessary.

1.2. Rapid solidification

Materials processing plays a central role in material science, since it has a strong effect on structure, properties and performances of the products [67]. For this reason, during the ’80, extensive research activity was conducted to provide a basic understanding of the main phenomena that occur during rapid solidification (RS) processing (i.e. mechanism and kinetics of nucleation and growth; connections between RS modes and resulting structures; characterization of fine-scale RS structures; structure/properties relationships contributing to the novel properties observed) [67–70].
Rapid solidification processes are defined as

processes having cooling rate larger than 10^2 K/s [67].

These cooling rates are typically achieved with processes involving solidification of small droplets (e.g. atomization), melt spinning of continuous or discontinuous ribbons or in-situ melting and solidification of thin surface layers. A schematic representation of these processing techniques is depicted in ***Fig. 1.6***.

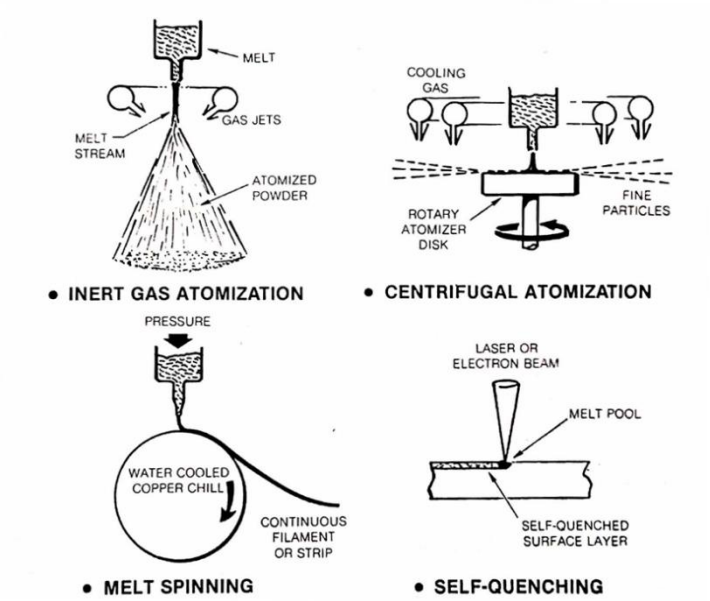

Fig. 1.6 *Principal techniques associated to rapid solidification [67].*

The techniques presented in ***Fig. 1.6*** however are not able to provide bulk products, but only powders (e.g. atomization) or thin layers (e.g. melt spinning and self-quenching). The production of 3-dimensional shapes using rapidly solidified powders was performed through classical consolidation techniques, such as hot isostatic pressing, hot extrusion and incremental solidification.

For the purposes of this thesis, incremental solidification, also known as layerglazing, is of particular interest as ancestor of AM; in fact in ***Fig. 1.7*** it is possible to find all the elements that were already described in section 1.1 when describing the different AM techniques, i.e. laser or electron beam, powder or wire feed.

In layerglazing a

"bulk rapidly solidified structure is built-up incrementally on a rotating mandrel, simply by laserglazing one thin layer of feedstock directly upon another in a continuous manner" [71]

as schematically represented in ***Fig. 1.7***.

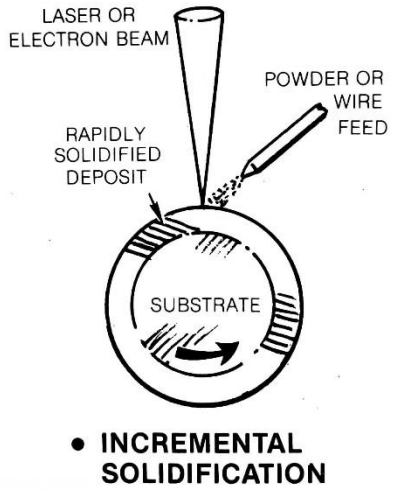

Fig. 1.7 *Schematic representation of incremental solidification or layerglazing [67].*

The changes in the microstructural features observed upon rapid solidification are schematically represented ***Fig. 1.8***.

Moving from equilibrium solidification to processes having cooling rates higher than 10^2 K/s, but maintaining the local interfacial equilibrium at the solid-liquid interface, it is possible to observe a refinement in the

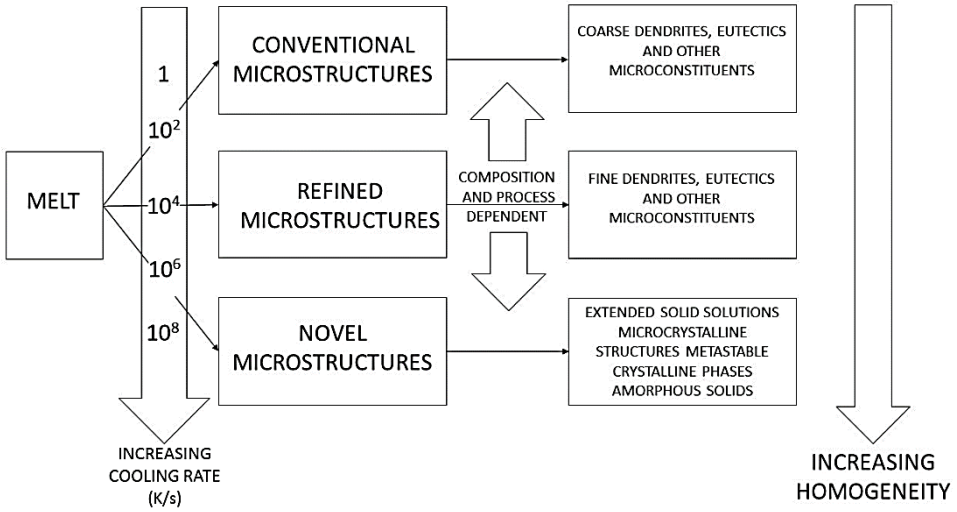

Fig. 1.8 *Approximate classification of microstructural consequences upon rapid solidification [67].*

microstructural features resulting from differences in the growth process.
Further increasing the cooling rate (i.e. cooling rate > 10^6 K/s) and so moving towards non-equilibrium solidification, nucleation can be depressed to temperatures far below the *liquidus* temperature. This undercooling is responsible for the formation of novel microstructures displaying some peculiar features such as the extension of solid solubility, the formation of microcrystalline structure and metastable phases. In presence of a sufficiently high cooling rate and suitable alloy compositions, it is possible to obtain metallic glasses. These novel features are responsible for an increase in the mechanical properties of the materials.

Different microstructural morphologies will result from differences in the thermal gradient (G) and solidification rate (R). As depicted in ***Fig. 1.9***, it is possible to distinguish three solidification front morphologies when

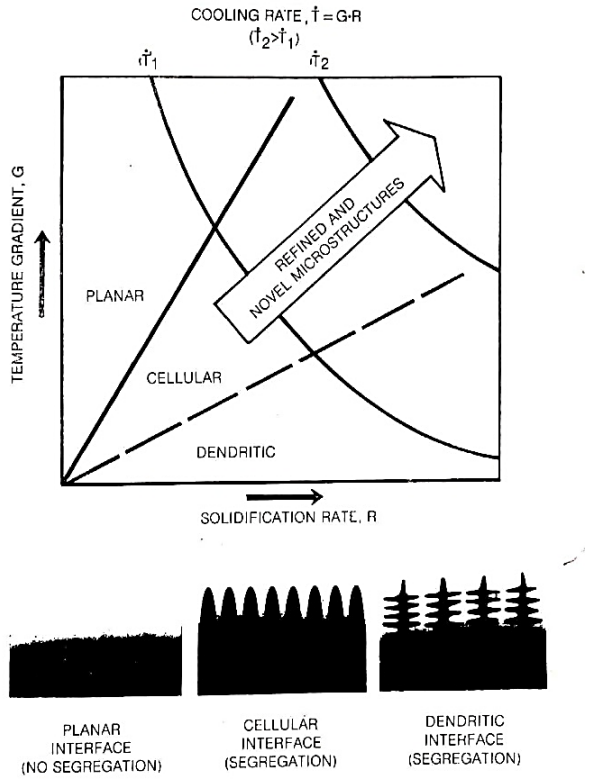

Fig. 1.9 *Solidification morphology dependence on thermal gradient (G) and solidification rate (R) [67].*

assuming conditions of local interfacial equilibrium at the interface.

So, a steep thermal gradient combined with low solidification rates will result in the stabilization of the planar-front growth and consequently in compositional homogeneity. Increasing R, the solute gradient at the interface will increase, leading to a destabilization of the planar-front resulting in micro-segregation and formation of cellular or dendritic microstructures.

The product $G \cdot R$, represented in the *G*, *R* space reported in ***Fig. 1.9***, is a measure of the cooling rate ($\dot{T}$), so the microstructural refinement indicated by the arrow in ***Fig. 1.9*** is the resultant of an increase in cooling rate.

1.3. Aluminum and Aluminum alloys

Aluminum (Al) is one of the most used metal for industrial applications due to its light weight (it has a density of only 2.70 g/cm^3) coupled with the high strength obtainable for some Al alloys [72,73].
Of course, the mechanical, physical and chemical properties of Al alloys will vary a lot according to their compositions and microstructures. The principal physical properties of Al are reported in ***Table 1.2***.

Table 1.2 *Principal physical properties of Aluminum [72].*

Property	***Unit***	***Value***
Atomic number	-	*13*
Atomic mass	-	*26.982*
Crystal structure	-	*fcc*
Lattice parameter (a)	*nm*	*0.40494*
Melting point	*°C*	*660*
Boiling point	*°C*	*2467*
Density (ρ)	*g cm^{-3}*	*2.70*
Elastic modulus (E)	*GPa*	*70*
Mean specific heat 0-100°C	*J kg^{-1} K^{-1}*	*917*
Thermal conductivity 20-100°C	*W m^{-1} K^{-1}*	*238*
Coefficient of thermal expansion 0-100°C	*10^{-6} K^{-1}*	*23.5*
Electrical resistivity at 20°C	*μ Ω cm^{-1}*	*2.67*

Usually, to improve the properties of pure Al, what is done is to alloy selected elements to Al such as Copper (Cu), Manganese (Mn), Silicon (Si), Magnesium (Mg) and Zinc (Zn). The impurities that can be found in Al alloys are generally below 0.15wt%.
Aluminum alloys are conventionally divided in two categories: wrought alloys and cast alloys. A further distinction of Al alloys can be provided considering the primary mechanism of property development.
The Aluminum Association system developed a different nomenclature for wrought and cast Al alloys in which the first ones are described by a four-digit system and the latter by a three-digit system followed by a decimal value.

In ***Table 1.3*** and ***Table 1.4*** are reported the classifications given by the Aluminum Association system for both wrought and cast alloys according to the composition of the alloy.

Table 1.3 *Classification of wrought Al alloys according to their composition [73].*

Series for wrought alloys	
1xxx	*Pure Al, ≥ 99.00%*
2xxx	*Cu as principal alloying element, other elements such as Mg may be specified*
3xxx	*Mn as principal alloying element*
4xxx	*Si as principal alloying element*
5xxx	*Mg as principal alloying element*
6xxx	*Mg and Si as principal alloying elements*
7xxx	*Zn as principal alloying element, other elements such as Cu, Mg, Cr, Zr may be specified*
8xxx	*Miscellaneous composition: may contain Sn, Li and Fe*
9xxx	*Reserved for future use*

The Aluminum Association system, moreover, developed a further distinction considering the heat treatments performed on the alloys to give an indication on the mechanical properties of alloys and how they are achieved. This nomenclature system consists in letters and digit added as suffixes to the alloy number and is reported schematically in ***Fig. 1.10***.
In this thesis attention will be focused on cast alloys of the 3xx.x series, in particular the AlSi10Mg alloy, an alloy similar to the A360.2; that will be discussed more in detail in section 2.1.

Table 1.4 *Classification of cast Al alloys according to their composition [73].*

Series for cast alloys	
1xx.x	*Pure Al, ≥ 99.00%*
2xx.x	*Cu as principal alloying element, other elements may be specified*
3xx.x	*Si as principal alloying element, other elements such as Cu and Mg may be specified*
4xx.x	*Si as principal alloying element*
5xx.x	*Mg as principal alloying element*
6xx.x	*Unused*
7xx.x	*Zn as principal alloying element, other elements such as Cu, Mg may be specified*
8xx.x	*Sn as principal alloying element*
9xx.x	*Unused*

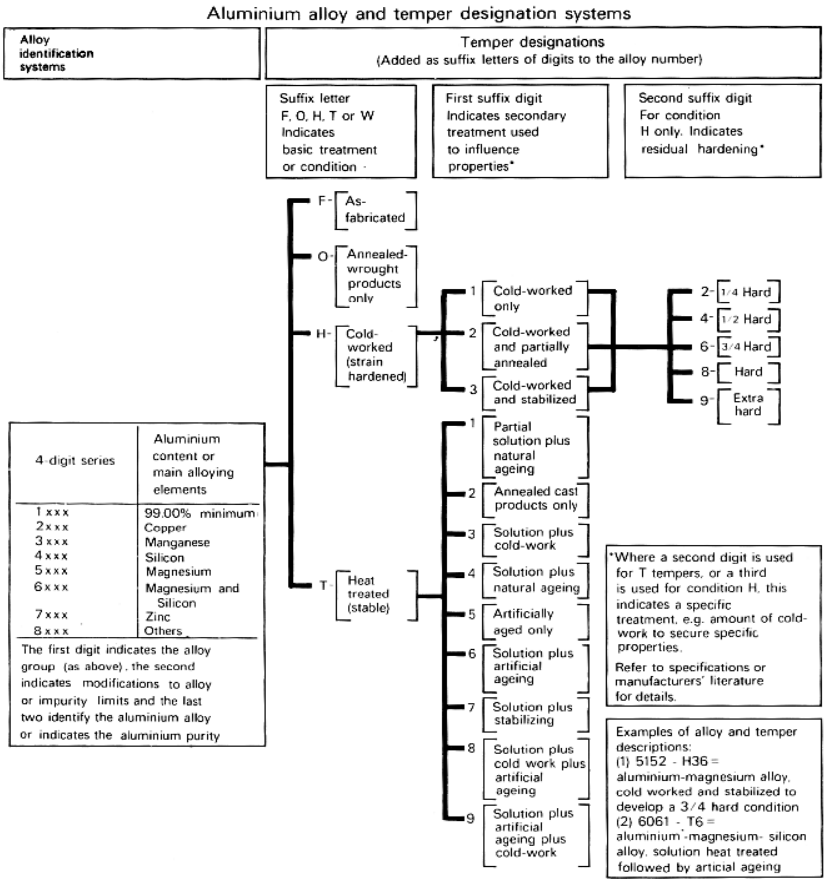

Fig. 1.10 *Heat treatment designation system according to the Aluminum Association system [72].*

1.4. Some open points in Additive Manufacturing

Despite the increasing research activities concerning AM processes, at the beginning of my PhD course the knowledge of these innovative rapid solidification processes was still limited.

The PhD was performed in the framework of the STAMP (Sviluppo Tecnologico dell'Additive Manufacturing in Piemonte) regional project dealing with the technological development of AM in Piedmont. This project, performed in partnership with several local industries and research facilities, had as one of its principal tasks the investigation of new Al alloys suitable for AM processes.

In this thesis, the work performed in the framework of the project will be described analysing three topics not widely studied in literature at the beginning of the PhD.

First, it was noticed the lack in literature of the solidification mechanism occurring during the L-PBF process. This was considered the first key feature to be analysed since, knowing the solidification mechanism, it will be possible to tailor new materials in function of the process instead of adjusting the process for known alloys.

Once deepen the knowledge on the solidification mechanism, another limiting factor was identified, being the limited material palette available for producing components through AM, especially when considering Al alloys. New compositions for AM were studied exploiting the knowledge of the effects arising from RS (e.g. extended solid solubility, formation of novel microstructures, …). Moreover, a new route to test alloys for AM was proposed, reducing time and costs of testing.

The presence of residual stresses was identified as a bottleneck in the application of parts processed by L-PBF. Few literature works were found in which the residual stress of components was measured and even fewer works employing techniques suitable for industrial application were found. So, to better understand this topic, several tests were performed with conventional and unconventional techniques easily employable for industrial purposes.

Detailed motivation for each topic will be reported in the following sections and in the following chapters each point will be deeply described.

1.4.1. Understanding the solidification mechanism

Starting from 2010, several authors have studied the optimum process parameters to build high density components by AM using Al-Si alloys, focusing their attention mostly on the peculiar microstructure resulting from the fast laser-material interaction and investigating the effects of thermal treatments on these novel microstructural features [9,11,15–21,74–88]. Nevertheless, detailed knowledge of the mechanism of formation of the microstructural features during fast cooling was not fully described. What is known, is that, after fast melting the crystal growth front moves rapidly across the melt pool producing a microstructure made of cells (or columns) and fine eutectic. The primary phase is apparently supersaturated and the eutectic coupled growth is confined in thin volumes around the cells [17,89,90] so the amount of trapped solute and that of retained eutectic are crucial parameters to be clarified.

Exploiting the fact that the extension of Si solubility in Al-Si alloys has been studied since the early development of rapid quenching technique in the ’80 to investigate surface hardening, it was aimed to advance in the interpretation of the microstructure of L-PBF Al-Si alloys on the basis of the available information on rapid solidification and new experiments. Using the changes in lattice parameter of Al, the thermodynamic of metastable phases and the kinetics of precipitation in samples produced by splat quenching, melt spinning and atomization [91–99] along with studies on dendritic growth under rapid solidification conditions [98,100–103], a correlation was sought for microstructures produced by different RS techniques spanning a large range of cooling rates. Moreover, experimental results on supersaturation, calorimetric responses and dimensions of the microstructural features were exploited along with the literature to propose a solidification mechanism.

1.4.2. Enlarge the material palette

Once investigated the solidification mechanism associated to L-PBF processes, the next step was to investigate how it is possible to improve the properties of the AlSi10Mg alloy.

From a literature search, it was evident that despite the increasing demand of new materials compatible with L-PBF processes and the amount of research work [31,66,104,105], the palette of materials available is still limited [63,106]. One of the main issues associated to the development of new alloys for AM is the necessity to have powders of appropriate size and shape. In order to test new materials, either powders of suitable composition should be produced, or commercial powders should be mixed for direct alloy synthesis under the laser beam. Mixing powders of different elements or alloys is fast and allows flexibility in designing new alloys, however, fluctuation in composition may occur, especially if powders having different melting point and reflectance are employed [13,65,105,107,108]. In both cases building samples for microstructure evaluation and property screening is demanding in terms of time and material consumption.

To optimize the process parameters for L-PBF and reduce the amount of material consumption, Laser Single Scan Tracks (SSTs) could be useful. SSTs consist in scanning powders with a laser along a single line to verify if the melt pool originating from the laser-material interaction is continuous and stable [109]. As reported in literature [110–114], the process window providing a stable melt pool in SSTs is likely to produce a 3D object with high density. However, the microstructural features of SSTs have not been investigated in detail, including the role of fluctuation in elemental composition which may be expected because of the fast laser-material interaction.

In AM melt pools are rapidly solidified by the underlying alloy, as shown by the refined microstructures and supersaturation found in the products. Since rapid solidification techniques are well established, e.g. Melt Spinning (MS), it appears also useful to test the outcome of solidification of new materials by MS to quickly determine their microstructure and the main properties before performing L-PBF synthesis. Melt spun products are obtained from a

homogeneous melt, even if different powders are mixed, because of the inherent stirring which occurs in induction melting, whereas SSTs mimics the conditions encountered in L-PBF. Therefore, MS seems suited for alloy selection whereas SSTs for defining the laser processing parameters.
Following up the comparison of rapidly solidified AlSi10Mg alloy described in chapter 3, the next step was to modify the composition of the alloy to improve its mechanical properties. This was done by both adding typical hardeners (e.g. Cu and Ag) [72,115] and grain refiners (Er, TiB_2 and Sr) [116–128] of Al alloys to the AlSi10Mg alloy and evaluating the effect of rapid solidification on the microstructure and nanoindentation hardness of the new compositions.
The final goal of these tests was to validate a new route for testing materials suitable for AM limiting the time and amount of material necessary for material design. In particular, the possibility to employ MS and SSTs as tools to predict the microstructure and properties of a component produced by L-PBF was explored.

1.4.3. The problem of residual stresses

As already introduced in section 1.1, the steep thermal gradients arising during the Additive Manufacturing processes as well as the alternating thermal expansion and contraction of the alloys due to heating and cooling in the subsequent layers can result in the formation of residual stresses.
Residual stresses are defined as

"self-equilibrating internal stresses existing in a free body which has no external forces or constraints acting on its boundary" (UNI EN 15305:2008).

Residual stresses can be classified according to the scale at which they occur. Stresses of type I are those varying over large distances, i.e. the dimension of the part, and can result in macroscopic deformation of the part. Type II and type III stresses instead occur due to the presence of different phases and dislocations at the atomic scale. Here attention will be focused primarily on type I residual stresses [129,130].

The magnitude of residual stresses arising in the alloy will vary according to the properties of the different alloys and to the process parameters employed during AM; moreover, as reported for welding, these are highly non-uniform in space and, of course, will vary a lot with time during the process.

The presence of residual stresses can be advantageous, for instance the presence of compressive stresses on the surface of a component is helpful in increasing the overall load resistance and preventing crack growth from the surface [129]. But high residual stresses can have detrimental effect on parts produced by AM leading to distortion, cracking and delamination. To prevent the distortion of the part, a careful positioning of the support structures is required, moreover it is important to fully optimize the process parameters for the job, i.e. high laser power, low scan speed, thicker layers, shorter scan vectors and the use of preheating can reduce the cooling rate and so the thermal gradient arising in the alloy. Other key factors to consider in predicting the formation of high residual stresses are the properties of the material to be processed such as thermal diffusivity, thermal expansion, yield stress, Young's modulus and melting point as well as the presence of significant metallurgical phenomena, e.g. allotropic transformations.

Despite the fact that residual stresses are one of the main problems in the production of complex components by AM, research activities on this topic are still limited [129,131–145].

Residual stresses can be measured with several techniques, the most suited one should be chosen according to the type of part under study taking in consideration sampling volume, accuracy and destructiveness.

In ***Fig. 1.11*** are reported the principal techniques employed conventionally to perform residual stress measurements along with their destructiveness.

Among the different techniques for residual stress determination, here attention was focused on X-Ray Diffraction (XRD), a non-destructive technique analysing a limited volume of sample depending on the penetration of the X-ray in the material. In particular, residual stress measurements with XRD were carried out to investigate if changes in process parameters were able to affect the final stress of the components.

Moreover, following the work performed by Li et al. in [79], residual stress in the AlSi10Mg alloy was investigated also with Raman spectroscopy, a

technique not listed in ***Fig. 1.11*** which can be used in specific cases such as Al-Si alloys.

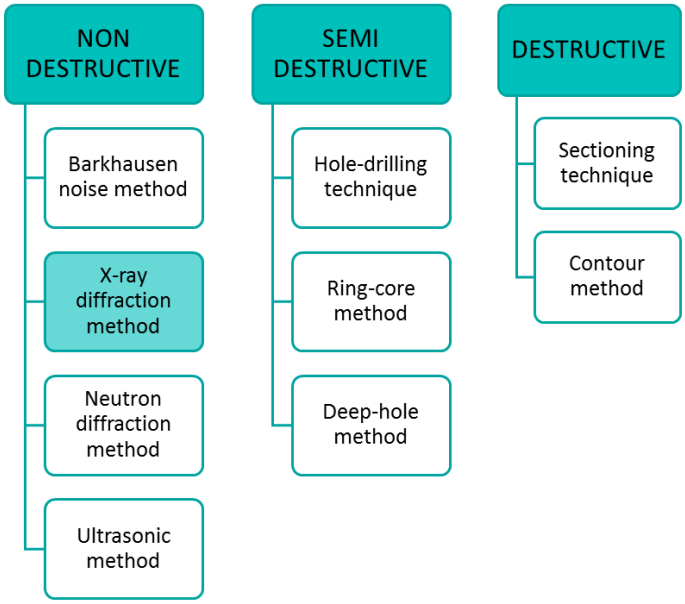

Fig. 1.11 *Classification of the techniques that can be used for the determination of residual stresses along with their destructiveness [130].*

Raman spectroscopy is known to provide information on microscopic strain of Si by analysing the shift of its transverse optic (TO) mode; as reported in ***Fig. 1.12*** a blue shift (higher wavenumber) is indicative of compressive stress and a red shift (lower wavenumber) is indicative of tensile stress [146–154]. In principle this technique would allow to get fast and in a non-destructive way information on the stress level present in Si containing alloys.
Nevertheless, Raman shift is well known to be influenced also by the size of Si crystals, especially when the nanometre range is reached, as reported in [155–166]. In their work, Campbell and Fauchet [167] explain that a distribution of tensile stresses in a Si sample can produce a Raman spectrum identical to that resulting from a sample containing small Si crystals, but in this second case it is possible to observe also a broadening of the peak. This is related to the fact that optical properties of crystals change alongside with their dimension, in particular, if crystals having dimension lower than 10 nm are considered, quantum size and confinement effects (i.e. the interruption

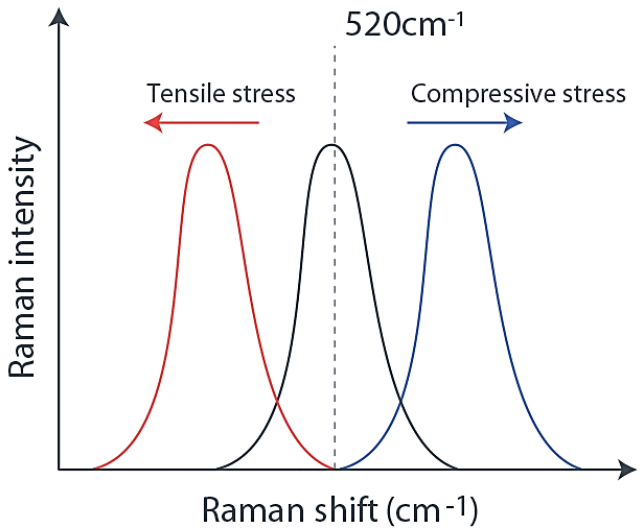

Fig. 1.12 *Schematic representation of the effect of residual stresses on the position of the transverse optic mode of Si (image from the www.nanophoton.net website).*

of phonon propagation due to the limited periodicity of crystals along with the relaxation of the selection rule $q = 0$ and the scattering contribution from the whole Brillouin zone beside the centre) become important leading to a bandgap increase and to a strong modification of optical and electrical properties.

So, to understand if the Raman shift observed in samples produced by means of rapid solidification was correlated to the presence of stresses or phonon confinement, a systematic study was performed and a correlation was sought with the residual stress values obtained conventionally analysing the residual stress of the face centred cubic Al by XRD.

2. Materials and methods

2.1. AlSi10Mg alloy

In Aluminum-Silicon (Al-Si) alloys of the 3xx.x series, according to the quantity of Si present in the alloy, it is possible to distinguish among eutectic alloys, i.e. having Si content of 12.7wt% (green line in ***Fig. 2.1***), hypoeutectic alloys, i.e. those with Si content lower than 12.7wt% (blue box in ***Fig. 2.1***), and hypereutectic alloys, i.e. those in which the amount of Si is larger than 12.7wt% (yellow box in ***Fig. 2.1***).

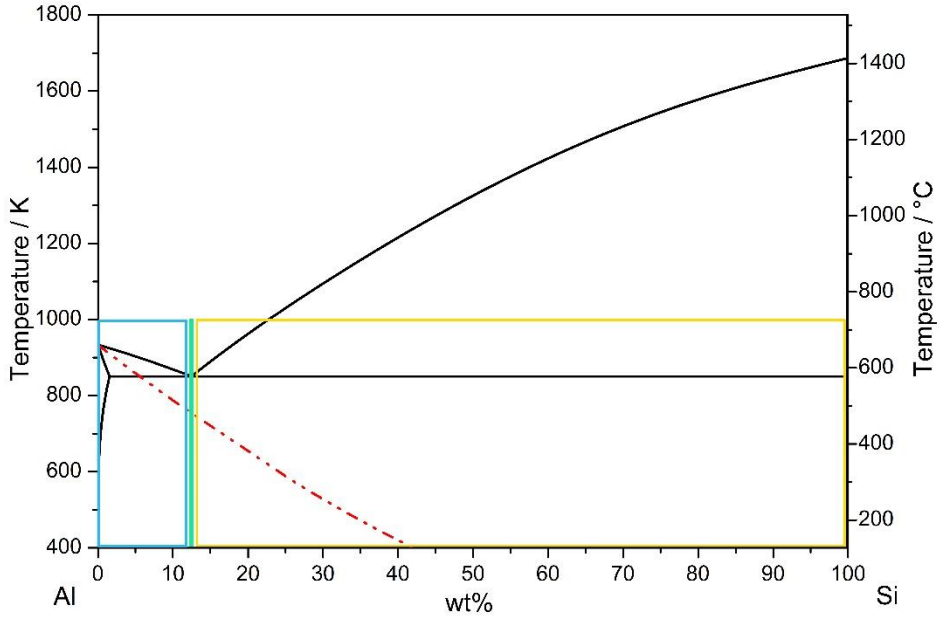

Fig. 2.1 *Al-Si phase diagram in which the blue box represents hypoeutectic compositions, the yellow one the hypereutectic compositions and the green line the eutectic composition. The red dash-dot line represents the T_0 curve for the Al rich part of the phase diagram.*

Al-Si alloys are typically employed in aerospace and automotive industries due to their good mechanical properties coupled with their low weight and high heat conductivity. These alloys are widely used for casting due to their good castability, weldability and corrosion resistance.

In this thesis, attention will be focused on the AlSi10Mg alloy, that is a hypoeutectic Al-Si alloy conventionally used for casting.

The presence of Si in the AlSi10Mg alloy is at the origin of the good castability of the alloy; this, coupled with the small solidification range of the near-eutectic composition, favours the processability of AlSi10Mg by L-PBF [106]. Moreover, Si improves the fluidity of the alloy, leads to higher wear resistance, strength and hardness and influences the thermal expansion coefficient and specific density of the alloy according to its content.

Magnesium in Al-Si alloys is usually added to harden the alloy through the precipitation of Mg_2Si, which gives a strengthening of the matrix without affecting the other mechanical properties [73].

When solidifying in equilibrium condition, hypoeutectic Al-Si alloys display a microstructure made of dendrites of α-Al surrounded by lamellar Al-Si eutectic, as depicted in ***Fig. 2.2***. The amount of eutectic present in the alloy will vary according to the amount of Si present in the alloy following the lever rule.

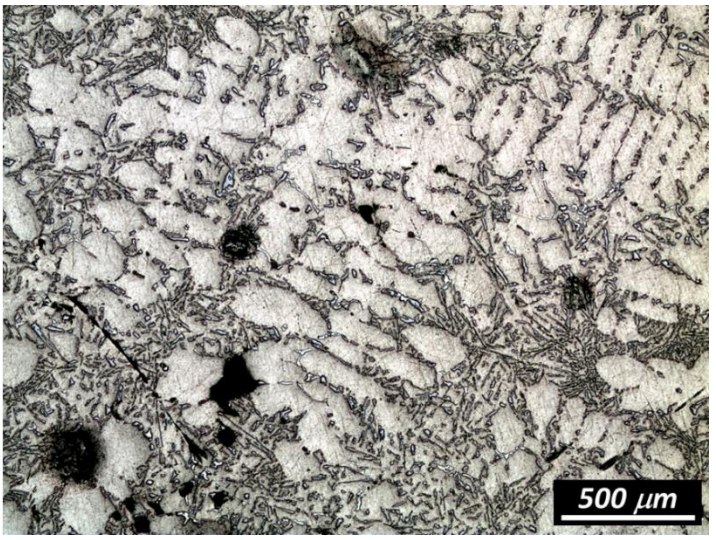

Fig. 2.2 *Optical micrograph representing the equilibrium microstructure of the AlSi10Mg alloy used in the present work. The microstructure is made of primary α-Al dendrites and lamellar Al-Si eutectic.*

2.2. Production techniques employed

2.2.1. Arc Melting

Master alloys, when necessary, were prepared using an arc furnace. The electric arc Buehler furnace is made of a vacuum system (consisting in a rotative and a turbomolecular pump), a cylindrical room, an electrode made of a Tungsten-based alloy, a current generator (necessary for the production of the electric arc) giving a current from 20 to 400 A, a water-cooled Copper plate having crucibles of different size and shape where elements are molten and an entry for the gas flux (usually Argon 99.999% pure) necessary to limit the amount of Oxygen from the melting chamber (***Fig. 2.3***).

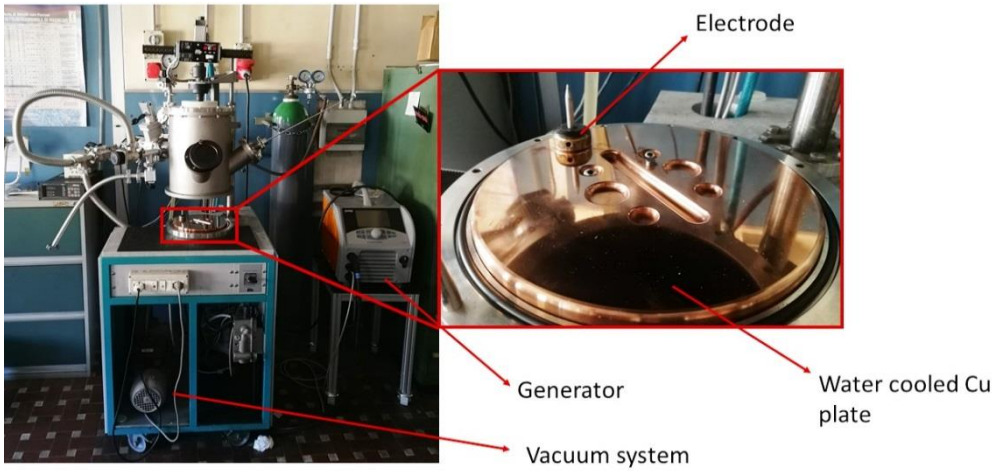

Fig. 2.3 *Buehler arc furnace along with its components.*

2.2.2. Copper Mould Casting

Casting is a traditional manufacturing process consisting in pouring a liquid metal inside a mould of the desired shape to let it solidify. In the case of Copper Mould Casting (CMC), the Cu mould assures fast heat extraction from the molten alloy to obtain RS.

The instrumental apparatus employed for CMC is depicted in ***Fig. 2.4***. A quartz crucible is surrounded by an induction coil used to melt the material and the Cu mould is aligned with the nozzle of the crucible. All the

components mentioned are surrounded by inert atmosphere to avoid oxidation of the alloy. Once the alloy is completely molten a gas overpressure ejects the alloy into the mould and the heat is dissipated through the Cu walls of the mould.

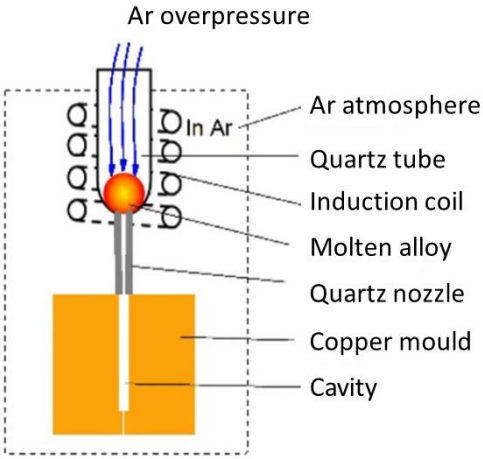

Fig. 2.4 *Copper Mould Casting apparatus [168].*

Here, due to the difficulties encountered in melting powders by induction, a Tantalum (Ta) foil positioned inside the quartz crucible was employed as a susceptor to help the melting process. The presence of the Ta foil, even if fundamental to melt the powders, does not allow to see when the liquid is homogeneous, so to have a homogeneous liquid the alloy was kept well above the melting temperature.

The Cu moulds employed to produce the samples have conical ($ø = 1\ mm$) and cylindrical shape ($0.5\ mm \leq ø \leq 5\ mm$), ***Fig. 2.5***.

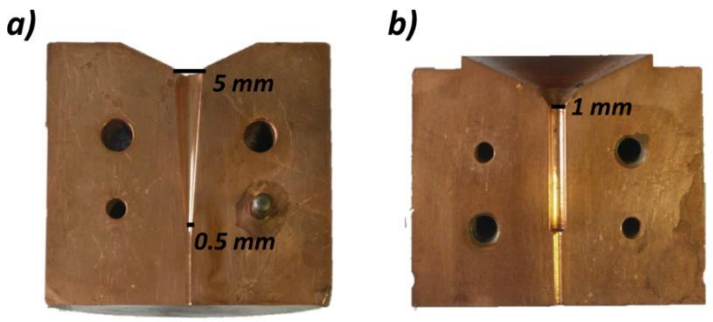

Fig. 2.5 *Conical (a) and cylindrical (b) Cu moulds employed to produce CMC samples.*

An example of sample produced by means of CMC using the conic mould is reported in ***Fig. 2.6***.

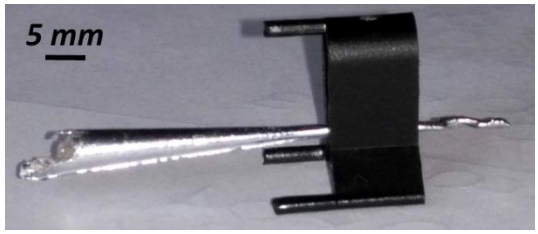

Fig. 2.6 *AlSi10Mg cone produced by Copper Mould Casting.*

2.2.3. Melt Spinning

Melt Spinning is a rapid solidification processing route (solidification rates ranging between 10^4 and 10^7 K/s) consisting in the expulsion of a molten alloy onto a rotating Cu wheel to produce ribbons. The MS apparatus is made of a furnace, composed by a crucible surrounded by an induction coil, and a rotating Cu wheel. An example of Melt Spinning apparatus is represented in ***Fig. 2.7***.

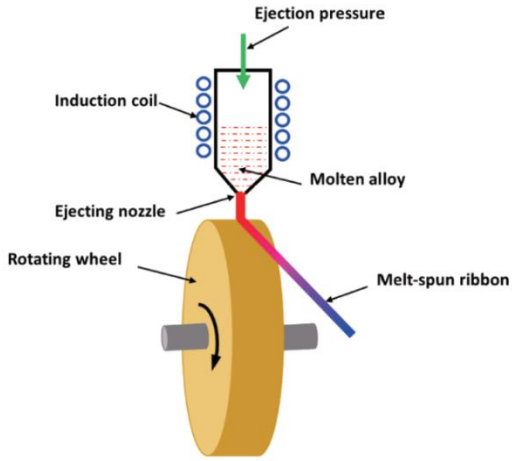

Fig. 2.7 *Schematic representation of a Melt Spinning apparatus [169].*

Also for MS, to melt AlSi10Mg powders was necessary to introduce a susceptor into the crucible. More specifically in this case Boron Nitride (BN) crucibles were employed and to avoid contaminations of the alloy, a Ta foil

was introduced in between two layers of BN, as schematically depicted in ***Fig. 2.8***.

Once molten, the alloy is ejected by an Ar gas overpressure onto the Cu wheel rotating at a predefined velocity.

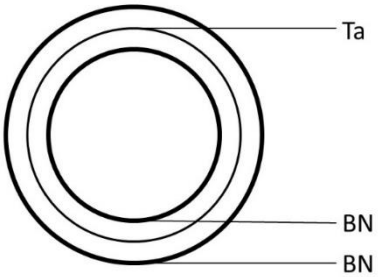

Fig. 2.8 *Cross section of the crucible employed in Melt Spinning experiments to melt the powders.*

The ribbons obtained display different morphologies on the two sides, so distinction will be made between air side, that correspond to the part of the ribbon that exchange heat with the inert atmosphere, and wheel side, corresponding to the side of the ribbon directly in contact with the Cu wheel during solidification.

An example of MS ribbon is shown in ***Fig. 2.9***.

Fig. 2.9 *AlSi10Mg ribbon obtained by Melt Spinning.*

2.2.4. Laser Powder Bed Fusion process

The AM samples were prepared by Direct Metal Laser Sintering (DMLS), that is the EOS trademark for L-PBF, with an EOSINT M270 Dual Mode version property of IIT and Polytechnic of Turin located in the IAM (Integrated Additive Manufacturing) laboratory in Polytechnic.
In this machine, a high-power Ytterbium (Yb) fibre laser system is used to selectively melt layers of powders under an inert Argon (Ar) atmosphere with a continuous power up to 200W.
The functioning of the DMLS machine, showed in ***Fig. 2.10***, was already described in section 1.1.

Fig. 2.10 *EOSINT M270.*

This machine employs different parameters for the core of a component, for its lower and upper surfaces, parallel to the building plane, and for the lateral outer surface, called contour. Core and Skin correspond to the 2-dimensional surfaces scanned by the laser source, while the contour is associated to a 1-dimensional closed-type line. First, the contour of the layer structure is exposed; then the inner area delimited by the contour is scanned through hatching: the laser beam moves line after line several times, and the distance between the lines is called hatching distance. Finally, a second exposure of the exterior part contour is carried out to make sure that the part edges correspond exactly to the CAD model, and that the part can thus be built with

the correct dimensions. Layer thickness and scanning strategy are also fundamental parameters. The thinner the powder layer, the greater the degree of interlayer bonding and, so, the higher the final density that can be obtained. However, if a too thin layer is chosen the rate of manufacturing will be too slow and the production time considerably longer.

Regarding the scanning strategy associated to the core and to the skin (made up of three layers), a certain degree of rotation between the layers is suggested to obtain better overlap. This should make the mechanical properties of the parts more isotropic in comparison with other scanning strategies made of layers with unidirectional vectors or with a cross-ply pattern. In the present case the direction of scanning is rotated of 67° in between consecutive layers [18].

The samples produced for characterization purposes are cubes of $15x15x13\ mm$ including supports. The dimensions of samples without supports are $15x15x10\ mm$. Images of L-PBF sample with and without supports are presented in ***Fig. 2.11***.

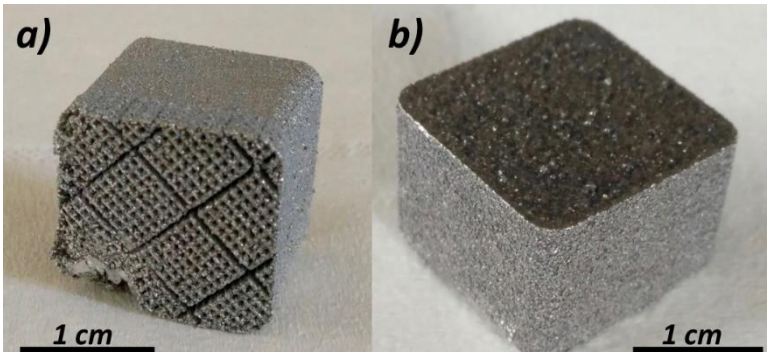

Fig. 2.11 *Cubes produced by L-PBF: detail of the supports (a) and top and side surfaces (b).*

2.3. Characterization techniques

2.3.1. Optical Microscopy

Optical microscopy (OM) is used to characterize the microstructure of samples.
The OM employed in this work is a Leica DFC295 coupled with the Leica Application Suite (LAS) software. The magnifications achievable with this instrument are 50X, 100X, 200X, 500X and 1000X.

2.3.2. Scanning Electron Microscopy

The Scanning Electron Microscope (SEM) gives information both on the composition (backscattered electrons) and on the morphology (secondary electrons) of metallographic samples. Moreover, with Energy Dispersive X-Ray spectroscopy (EDX), it is possible to obtain qualitative and quantitative information on the elements present in the samples.
The SEM used for this work is a LEICA STEREO SCAN 420. In this specific instrument, electrons are generated by a Tungsten filament and accelerated applying a potential difference in the range of 1 to 30 kV.

2.3.3. Field Emission Scanning Electron Microscopy

To obtain images with higher resolution a Field Emission Scanning Electron Microscope (FESEM), having a range of magnifications from 10X to 300kX, was employed. With FESEM information can be collected through secondary electrons, backscattered electrons and characteristic X-Ray as already described for the conventional SEM, moreover it is possible to acquire images with the In-Lens detector, allowing to obtain clearer and less electrostatically distorted images with respect to a conventional SEM. The In-Lens acquisition system exploits a magnetic field to collect secondary electrons with high efficiency; in particular, it allows to obtain images with high contrast at low voltages and small working distances.
FESEM micrographs displayed in the following sections were acquired with a ZEISS SUPRA TM 40 equipped with Energy Dispersive X-ray spectrometer

(EDX, Oxford INCA Energy 450). High magnification images were acquired applying an accelerating potential of 5 kV with the 30 μm aperture and fixing the working distance at 7 mm. Images were generally acquired both using secondary electrons and In-Lens detectors.

2.3.4. X-Ray Diffraction

X-Ray Diffraction (XRD) is a powerful non-destructive technique that investigate the structure of crystalline materials using a monochromatic beam of X-Rays. The fundamental law describing the principles of this technique is the Bragg's law:

$$n\lambda = 2d \sin\theta$$

where λ is the wavelength of the incident X-Rays beam, n is an integer representing the scattering order, d is the interplanar distance of the plane's diffracting family and θ is the Bragg's angle, corresponding to half the angle between incident and diffracted beam.

Each diffraction pattern is a fingerprint of the material under study and allows to determine which are the phases present in a sample as well as their crystallographic structure.

This technique can be used directly on all crystalline solids (from powders to bulk samples) without the necessity of specific pre-treatments. However, the acquisition time necessary to obtain a good diffraction pattern can be quite long, depending on the quality required for the subsequent analysis.

XRD measurements described in the following sections for phase identification and lattice parameter calculation have been performed in Bragg-Brentano configuration, ***Fig. 2.12***, with a Panalytical X'Pert X-Ray

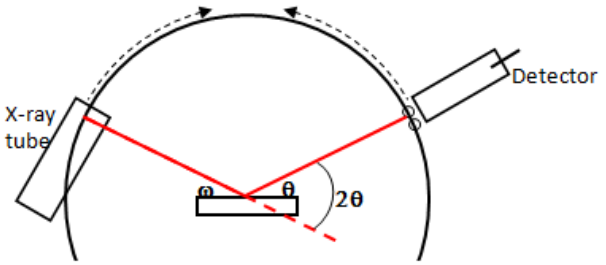

Fig. 2.12 *Schematic representation of the Bragg-Brentano configuration.*

diffractometer by Philips, using the K_α emission line of a Cu filament ($\lambda_{Cu} = 1.5418$ Å) as incident radiation. To produce the radiation an X-Ray tube with a voltage of 40 kV and a current of 30 mA has been used.

Stress measurements were performed in the ω-method (also called iso-inclination method) in which the specimen is tilted of an angle Ψ, lying on the same plane of 2θ, about the ω axis; following the procedures reported in the UNI EN 15305:2008 and in the SAE HS-784:2003 standards. ω values correspond to the sum of Ψ plus θ. In ***Fig. 2.13*** is reported a schematic drawing of the ω-configuration in which S_1, S_2 and S_3 represent the sample coordinate system, θ is the Bragg angle, 2θ is the diffraction angle, ωR represents the rotation about the ω axis, ϕR is the rotation about the ϕ axis, X is the X-Ray tube, SP is the specimen and D is the detector.

The ω-method was applied both with negative and positive Ψ-offset, when negative offset is applied the decreased incidence angle can cause the "defocusing effect" to increase, leading to a broadening of the diffraction lines and a decrement of the intensity of the peaks.

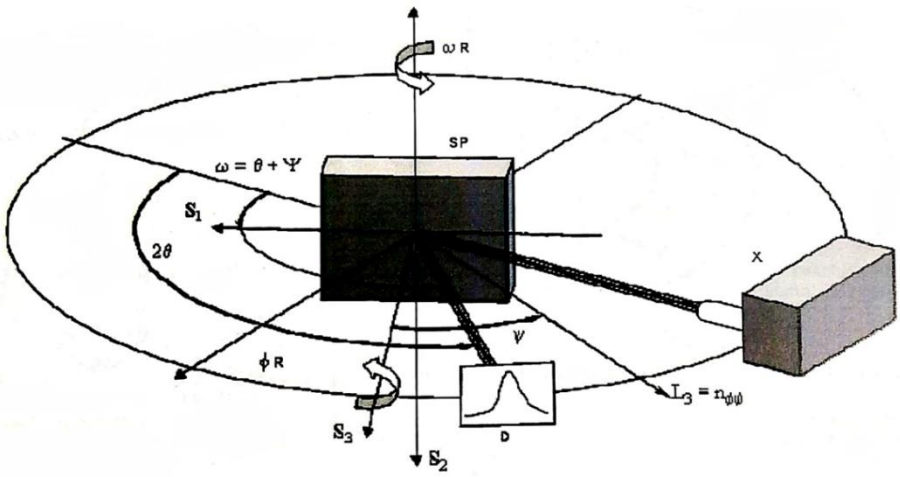

Fig. 2.13 *Schematic representation of the ω-configuration (UNI EN 15305:2008).*

The value of residual stress was calculated assuming plane stress conditions, i.e. implying the component of stress normal to the sample surface to be negligible; using the following equation, representing the basic relation between lattice strain and stresses,

$$\varepsilon_{\phi\Psi} = \left(\frac{1+\nu}{E}\right)_{hkl} \sigma_\phi sin^2\Psi - \left(\frac{\nu}{E}\right)_{hkl} (\sigma_1 + \sigma_2)$$

in which $\varepsilon_{\phi\Psi}$ is the strain vector, ν is the Poisson ratio, E is the Young modulus, σ_ϕ is the surface stress component to be determined, Ψ is the tilting angle selected during the measurements and σ_1 and σ_2 are stress components.

It is possible to describe the effective strain normal to the specimen surface as

$$\varepsilon_{\phi\Psi} = \frac{d_{\phi\Psi} - d_0}{d_0} = \frac{\Delta d}{d_0}$$

Where d_0 is the unstressed interplanar spacing and $d_{\phi\Psi}$ corresponds to the measured interplanar spacing. When $\Psi = 0$, $d_{\phi 0}$ will correspond to the measured spacing approximate in the direction of the surface normal.

From these equations it is evident that, if the stress is biaxial, the distribution of $d_{\phi\Psi}$ as a function of $sin^2\Psi$ will follow a linear trend. The intercept of the linear fit will correspond to the interplanar spacing at $\Psi = 0$

$$d_{\phi 0} = d_0 \left[1 - \left(\frac{\nu}{E}\right)_{hkl} (\sigma_1 + \sigma_2)\right]$$

while the slope of the fit will correspond to the residual stress in the specimen

$$\sigma_\phi = \left[\left(\frac{E}{1+\nu}\right)_{hkl} \frac{1}{d_0} \left(\frac{\partial d_{\phi\Psi}}{\partial sin^2\Psi}\right)\right]$$

Intercept and slope values along with their errors were determined through linear regression on the experimental data imposing a 95% confidence level to the linear fit.

In performing the calculation for residual stresses, it is important to underline that the elasticity constant to be used is the one specific for the (hkl) plane under analysis and that this value can differ considerably from the macroscopic value of a bulk specimen. The elastic constants specific for the (hkl) plane under consideration were calculated with the Reuss approach, that assumes all the grains to develop equal stresses, using the following

formulae in which the ratios -v/E and (1+v)/E are described in terms of elastic compliances

$$\left[\frac{-\nu}{E}\right]_{constant\ stress} = S_{12} + \frac{h^2k^2 + k^2l^2 + l^2h^2}{(h^2 + k^2 + l^2)^2}\left(S_{11} - S_{12} - \frac{1}{2}S_{44}\right)$$

$$\left[\frac{1+\nu}{E}\right]_{constant\ stress} = S_{11} - S_{12} - 3\frac{h^2k^2 + k^2l^2 + l^2h^2}{(h^2 + k^2 + l^2)^2}\left(S_{11} - S_{12} - \frac{1}{2}S_{44}\right)$$

Residual stress measurements were performed with the Panalytical X'Pert X-Ray diffractometer by Philips, using the K_α emission line of a Cu filament ($\lambda_{Cu} = 1.5418$ Å) as incident radiation, focusing on the (422) reflection of the face centred cubic (fcc) Al. The values of elastic compliances used to calculate the elastic constants for the (422) reflection of Al are reported in ***Table 2.1***.

Table 2.1 *Values of elastic compliances used for the calculation of the elastic constants for the (422) reflection of Al.*

S_{11} [Pa^{-1}]	S_{12} [Pa^{-1}]	S_{44} [Pa^{-1}]	Reference
$1.59*10^{-11}$	$-5.80*10^{-12}$	$3.52*10^{-11}$	[170]

The measurements at different Ψ angles, reported for clarity in ***Table 2.2***, were performed in the 2θ range from 135° to 141° with a step size of 0.0334° and with a time per step of 500 s.

Table 2.2 *Positive and negative Ψ offset and corresponding $\sin^2\Psi$ employed to measure the residual stresses by XRD.*

Negative Ψ offset [°]	$\sin^2\Psi$	Positive Ψ offset [°]	$\sin^2\Psi$
-50.768	0.6000	0.000	0.0000
-45.000	0.5000	+18.435	0.1000
-39.232	0.4000	+26.565	0.2000
-33.211	0.3000	+33.211	0.3000
-26.565	0.2000	+39.232	0.4000
-18.435	0.1000	+45.000	0.5000
0.000	0.0000	+50.768	0.6000

To determine the exact position of the diffraction peaks, experimental data were fitted with a Pseudo-Voigt function using the X'Pert Highscore software

by Panalytical. Residual stress values, obtained at both positive and negative Ψ offset, were averaged to provide a mean stress value.
Of course, instrument alignment was carefully checked prior to start the residual stress measurements (as suggested by the SAE HS-784:2003 and by the UNI EN 15305:2008 regulations). In order to verify instrumental alignment, measurements were performed on unstressed Ni and Al powders; moreover, trials of residual stress measurements were performed on a standard IN718 specimen provided us by GE Avio to verify if the procedure used for the calculation was correct. Measurements on the IN718 specimen were performed on the (311) reflection of Ni using the same acquisition parameters already described for the Al, the only difference being the angular range of the analysis (from 86° to 94°). In ***Table 2.3*** are reported the values of elastic compliances employed for calculating the elastic constants on the (311) reflection of Ni.

Table 2.3 *Values of elastic compliances used for the calculation of the elastic constants for the (311) reflection of Ni.*

S_{11} [Pa^{-1}]	S_{12} [Pa^{-1}]	S_{44} [Pa^{-1}]	Reference
$7.99*10^{-12}$	$-3.12*10^{-12}$	$8.44*10^{-12}$	[171]

Moreover, to be sure to align the samples always in the same way, a home-made sample holder exploiting a micrometric screw for the regulation of sample positioning was built, ***Fig. 2.14***.

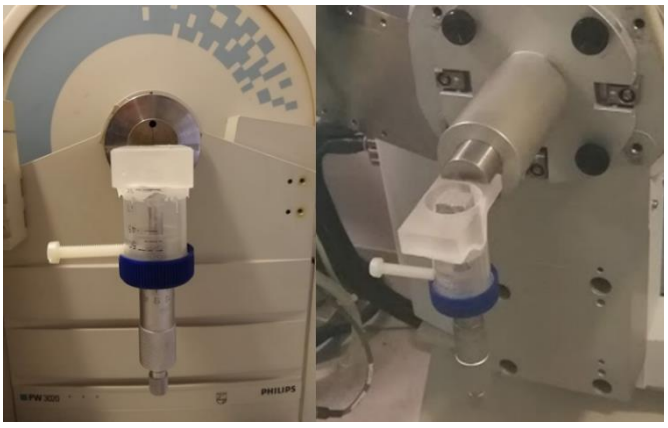

Fig. 2.14 *Home-made sample holder specifically designed for residual stress measurements.*

2.3.5. Differential Scanning Calorimetry

Differential Scanning Calorimetry (DSC) is a thermo-analytical technique based on the measure of the differences in heat flux between sample and reference when the sample undergoes a physical transformation during a controlled heating or cooling defined by a thermal program chosen by the operator. The amount of heat that will flow to the sample will depend on the transformation being endothermic (higher heat flux) or exothermic (lower heat flux).
DSC measurements are performed in an inert atmosphere in order to avoid unwanted reactions (e.g. oxidation) or contaminations; here measurements were performed under a constant flux of Argon (Ar).
The measurements described in the following sections were performed using a TA Q100 DSC. Measurements were performed to observe both precipitation phenomena at lower temperatures and melting and solidification of the alloy under study.
Measurements exceeding the melting temperature were performed in Al_2O_3 pans and those at lower temperature in Al pans equilibrating the heat flux during the measurements both at low and high temperature.

2.3.6. Nanoindentation

To evaluate the hardness of the alloys, nano-indentation tests were conducted with a TI950 Nanoindenter (Hysitron) at the Istituto Italiano di Tecnologia (IIT). The most common method to analyse the hardness and modulus values from an indentation curve is the Oliver-Pharr method. The Oliver-Pharr method requires no imaging of the indentation, instead it is based on contact mechanics [172]. The tests were performed by applying and removing a controlled load to the specimens using a geometrically well-defined probe, producing traditional force versus displacement curves. The analysis of these curves provided information regarding the mechanical properties of the sample. A diamond Berkovich tip indenter was used, that is a 3-sided diamond pyramid with an included angle of 142.3°, where the angle from the normal to a face is 65.35°. For MS samples indentation was performed every 4 μm on a grid having a width of 40 μm and variable length

according to the specimen thickness. On SST the grid was performed covering completely the melt pool spacing the indentation marks of 7.5 μm one from each other. For all samples the load velocity was 100 μN/s, maximum load was fixed to 2.5 mN and kept for 5 s. Load charge and discharge was done at the same velocity. For the *XZ* section of the as built AlSi10Mg+Cu L-PBF platelet the load was increased at 250 μN/s up to a maximum load of 2.5 mN that is removed after 5 s and then decreased at the same rate on a grid with 384 indentations (4 along *X* and 96 along *Z*), distant 10 μm from each other.

2.3.7. Raman Spectroscopy

Raman spectroscopy is a technique based on the inelastic scattering of light photons and it is commonly used to investigate vibrational, rotational and other low frequency modes of a Raman-active system in order to identify intra-atomic interactions. For a molecule to be Raman active, the electric polarizability needs to change if exposed to an external electromagnetic field. In a typical Raman spectrometer, a monochromatic laser beam is produced, this is focused on the sample surface and interacts with it creating an excited virtual state of the molecules in the sample. This state, being unstable, immediately returns to equilibrium emitting the photon as scattered light.
When the focused laser light hits the sample, incident photons usually undergo through Rayleigh elastic scattering leaving unchanged the state of the molecules in the sample. However once every 10^6-10^8 photons the scattering will be inelastic, resulting in the emission of a photon with either higher (Anti-Stokes) or lower (Stokes) energy with respect to the incident one and in the change of the vibrational or rotational modes of the molecules of the samples, ***Fig. 2.15***.
When photons are emitted with energy lower than that of the incident ones, the molecule will be at a higher energy state, meaning that there is a shift towards lower frequencies called Stokes shift (or downshift). Vice versa if the photons are emitted with energy higher with respect to the incident ones, there will be a shift towards higher frequency called anti-Stokes shift (or upshift). The ratio of Stokes and anti-Stokes scattering depends on the population of different states, i.e. at room temperature the ground state will

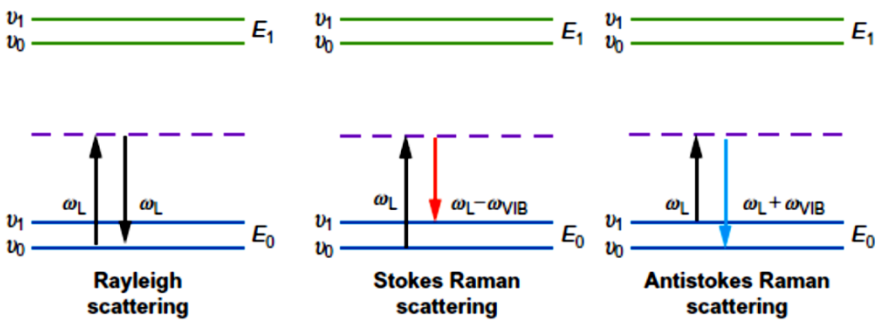

Fig. 2.15 *Scheme for photon scattering modes resulting from laser-material interaction in Raman spectroscopy [173].*

be more populated, so Stokes lines will be more intense with respect to anti-Stokes lines. Therefore, usually Raman spectrometer are equipped with filters that allow to measure only the Stokes scattering.

A schematic representation of the elements composing a Micro-Raman equipment is reported in ***Fig. 2.16***.

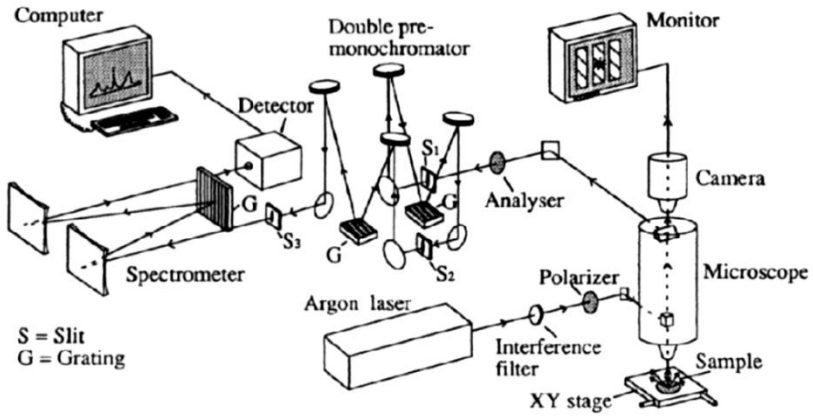

Fig. 2.16 *Scheme of the elements composing a Micro-Raman [147].*

In order to solve Raman spectra, a widely acknowledged confinement model proposed by Richter et al. [174] and extended by Campbell and Fauchet [167] to describe the behaviour of porous Si can be employed.

When very small nano-crystals are considered, the lattice excitations due to light scattering, are limited to the finite space occupied by the crystal itself. For these reasons, a phonon is considered confined in the crystallite volume.

The model is developed considering a Stokes scattering process in an infinite crystal, in which the wavevector difference is transferred to a phonon with wavevector $\overrightarrow{q_0}$. The wave function of that generic phonon is

$$\Phi(\overrightarrow{q_0}, \vec{r}) = u(\overrightarrow{q_0}, \vec{r})e^{-i\overrightarrow{q_0}\vec{r}}$$

where $u(\overrightarrow{q_0}, \vec{r})$ has the periodicity of the lattice, while the phonon in the nano-crystal becomes

$$\Psi(\overrightarrow{q_0}, \vec{r}) = W(\vec{r}, L)\Phi(\overrightarrow{q_0}, \vec{r}) = \Psi'^{(\overrightarrow{q_0}, \vec{r})}u(\overrightarrow{q_0}, \vec{r})$$

with $W(\vec{r}, L)$ as the phonon weighting function. $\Psi'^{(\overrightarrow{q_0}, \vec{r})}$ can be expanded in a Fourier series having coefficients

$$C(\overrightarrow{q_0}, \vec{r}) = \frac{1}{2\pi^3}\int d^3r\Psi'^{(\overrightarrow{q_0}, \vec{r})}e^{-i\overrightarrow{q_0}\vec{r}}$$

The Raman scattering intensity is then described by a continuous superimposition of Lorentz curves with bandwidth γ centred at the theoretical wavenumber $\omega(q)$ of the phonon dispersion curve and weighted by the $|C(\overrightarrow{q_0}, \vec{r})|^2$ factor.

Assuming a spherical Brillouin zone, neglecting scale factors and assuming $\overrightarrow{q_0}$ for one phonon scattering, the Raman intensity can be written as

$$I(\omega) \propto \int d^3q \frac{|C(\overrightarrow{q_0})|^2}{\big(\omega - \omega(q)\big)^2 - \left(\frac{\gamma}{2}\right)^2}$$

Through the phonon dispersion relation, the wavelengths can be easily calculated as

$$\big(\omega(q)\big)^2 = 2Ya\left[\frac{2}{m_a} \pm \sqrt{\left(\frac{2}{m_a}\right)^2 - 2\frac{1 - cos(qa)}{m_a^2}}\right]$$

In which Y is the Young modulus specific for porous Si (51.35 GPa), a is the lattice parameter for Si crystals (0.5431 nm) and m_a is the atomic mass of Si ($1.66 \cdot 10^{-27} \cdot 14$ kg).

The wave vectors $\vec{q}$ can also be represented as discretized values of the phonon momentum, although it should be kept in mind that the larger is the

wavelength of the phonons, the smaller is the corresponding wavevector ($\frac{4.49}{L}$). The allowed wavevectors will span in the range $\frac{4.49}{L}, \frac{7.72}{L}, \frac{10.90}{L}, \dots, \frac{2\pi}{a}$.
Various Fourier coefficient and weighting functions were considered, but in all the considered literature [163,165,167,175] the Gaussian profile was considered as the one that agrees better with the experimental data.
The coefficient and the weighting function were hence defined as:

$$|C(0,q)|^2 \sim e^{\left(-\frac{q^2L^2}{16\pi^2}\right)} \qquad W(r,L) = e^{\left(-\frac{8\pi^2 r^2}{L^2}\right)}$$

In this model, smaller nanocrystals will correspond to broader and more shifted Raman peaks.
This method was further expanded by Amato and Brunetto [165,175]. They considered a material composed by Si nano-crystals not having a defined dimension and proposed a log-normal distribution describing the dimensions of the nano-crystals inside the sample with the help of Transmission Electron Microscope (TEM) observations. In this way L is no longer considered as a deterministic fitting parameter but as a log-normal stochastic variable.
The distribution of the sizes become then governed by this formula

$$dF(x) = \frac{1}{\sigma\sqrt{2\pi}} exp\left\{-\frac{[ln(x)-\chi]^2}{2\sigma^2}\right\} d\, ln(x)$$

in which, since $\chi = ln(x)$ is related to the most probable value of x and since x represents the dimension L of the nano-crystals, it is easier to represent x as the logarithm of the said most probable value, corresponding to the mode of the distribution (addressed from now on as ρ).
Analysis of the Raman spectra were performed writing a program in the Mathcad software in order to fit the Raman signals obtained experimentally. At the beginning of the program, a three-point smoothing was added to improve the signal to noise ratio according to this formula

$$y_i = 0.25y_{i-1} + 0.50y_i + 0.25y_{i+1}$$

This procedure was followed by normalization and removal of the baseline, calculated as the minimum value of the raw data.
The Longitudinal Optical (LO) vibrational mode was approximated inside the fitting function as a Cauchy-Lorentz distribution function. The fitting

program, created following the Levenberg Marquardt method through the minimization of mean squared errors, creates a function through numerical integration, in accordance with the Campbell and Fauchet model, and calculates the frequency range through the conversion of the Raman shift.
The instrument used for the characterization of the AlSi10Mg samples is a Renishaw Invia Raman Microscope coupled with a blue laser source having wavelength of 442 nm. Measurements were performed limiting the laser power to 10% and focusing the light through a 50X objective, spectra were acquired exploiting the accumulation of 20 acquisition of 5 s each.

3. Part I: Solidification mechanism in AlSi10Mg

3.1. Experimental procedure

To investigate the solidification mechanism occurring in AlSi10Mg alloy when subjected to rapid solidification, several test samples have been produced employing techniques spanning a large range of cooling rates, i.e. Copper Mould Casting, Melt Spinning and Laser Powder Bed Fusion.
All samples were produced starting from the same commercial gas atomized powder, provided by EOS GmbH, having the chemical composition reported in ***Table 3.1***.

Table 3.1 *Chemical composition in wt% of the AlSi10Mg gas atomized powders provided by EOS GmbH.*

Alloy	***Si***	***Fe***	***Cu***	***Mn***	***Mg***	***Zn***	***Ti***	***Al***
AlSi10Mg	*9 - 11*	*≤0.55*	*≤0.05*	*≤0.45*	*0.2 – 0.45*	*≤0.10*	*≤0.15*	*Bal.*

Cubic L-PBF samples having sides of 15 mm were fabricated with an EOSINT M270 Dual Mode version employing the process parameters reported in [8] and repeated for clarity in ***Table 3.2***.
L-PBF samples were analysed both in the as built condition (AB) and after the stress relieving treatment (SR), i.e. an annealing performed at 300°C for 2h suggested by EOS to reduce the residual stresses arising during the process.
Pellets of powders were produced by gentle pressing and used for CMC and MS. Induction melting was performed with the help of a susceptor surrounding the crucibles as described in sections 2.2.2 and 2.2.3.
AlSi10Mg melt spun samples were obtained ejecting the molten alloy on a Cu wheel rotating at either 10 m/s or 15 m/s (MS-N10 and MS-N15 respectively).
Samples by CMC were obtained ejecting the melt into a conical mould having diameter varying from 5 mm to 1 mm (depicted in ***Fig. 2.5-a***).
Samples for micrographics observations were embedded in conductive resin, mechanically polished down to 40 nm and etched for 10 s using Keller's solution (i.e. 2.5 ml of HNO_3, 1.5 ml of HCl and 1 ml of HF in 95 ml of distilled water). Micrographs were acquired both at the optical and electron

microscope. Secondary electron imaging was carried out both in SEM and FESEM using a LEICA STEREO SCAN 420 and a ZEISS SUPRA TM 40 respectively.

Table 3.2 *Process parameters employed to produce cubic samples of AlSi10Mg alloy [8].*

Parameters	***Skin***	***Core***	***Contour***
Scan speed (v) [mm/s]	*900*	*800*	*900*
Laser power (P) [W]	*120*	*195*	*80*
Hatching distance (h_d) [mm]	*0.1*	*0.17*	*-*
Layer thickness [μm]	*30*	*30*	*-*
Laser spot size [mm]	*0.10*	*0.10*	*0.10*
Temperature of the building platform [°C]	*100*	*100*	*100*

XRD measurements were performed in Bragg-Brentano configuration using a PANalytical X'Pert PRO diffractometer by Philips, using the K_α emission line of a Cu filament ($\lambda_{Cu} = 1.5418$ Å). Patterns were acquired in the 2θ range from 20° to 140° at a step of 0.0167°. L-PBF sample before and after the stress relieving treatment were analysed on the top (AM_AB top and AM_SR top), side (AM_AB side and AM_SR side) and inner surface after cutting and mechanical polishing (AM_AB in and AM_SR in). The CMC cone was analysed along its cross section and the MS ribbons were analysed on both air and wheel sides. For all samples, including a portion of the alloy cooled from 660°C to room temperature at 3°C/min representing the solidification in near equilibrium condition, the face centred cubic (fcc) Al lattice parameter was computed with the $\cos\theta\cot\theta$ method.

Thermal analyses were carried on a TA Q100 Differential Scanning Calorimeter in the temperature range from 50°C to 450°C at the heating rate of 5 and 20°C/min equilibrating the heat flux at both temperatures to investigate the precipitation sequence. Investigation of melting and solidification of the alloy was conducted in the temperature range from 50°C to 660°C at a heating rate of 20°C/min.

3.2. Results

3.2.1. Comparison of results obtained with the different techniques

The micrographs of the microstructures obtained in AlSi10Mg samples produced by means of different rapid solidification techniques are reported in ***Fig. 3.1***. CMC samples were analysed after sectioning the cone along its principal axis. A thin area, smaller than 1 μm, near the outer surface of the cone appears to be almost featureless. This can be understood considering the fast rate of solidification occurring when the molten alloy is directly in contact with the Cu mould. Then, α-Al cells and columns are seen, surrounded by fibrous eutectic (***Fig. 3.1-a***). Their size increases from 1 to more than 5 μm from the tip to the base and from the outer surface to the core of the cone (***Fig. 3.1-b***).

It is well known, [176], that the microstructure of melt spun ribbons varies from the wheel side to the air side (***Fig. 3.1-c***). Here, the microstructure starts almost featureless at the wheel side, becoming then primary plus eutectic with subdivided fine Si particles and ending at the air side as primary Al cells surrounded by fibrous eutectic. The length scale of the cells observed along all the ribbon thickness is finer with respect to those observed in CMC samples, being of approximately 1-2 μm (***Fig. 3.1-d***).

As widely reported in literature [16,19,74,76,177], the microstructure of the L-PBF as built AlSi10Mg part has a transition from a very fine cellular-dendritic structure to a coarser dendritic structure going from the centre to the border of the melt pools. This is clearly visible in ***Fig. 3.1-e***, where the primary Al cells are surrounded by fibrous Si eutectic and change in size because of the heat flux generated during subsequent laser scans. Looking across a melt pool, three areas can be recognized: a finer microstructure in the centre (mpc), a coarser cellular microstructure in the transition zone from the centre of the melt pool to its border (mpb), and coarser Si particles in the heat affected zone around the melt pool in the layer previously deposited (haz).

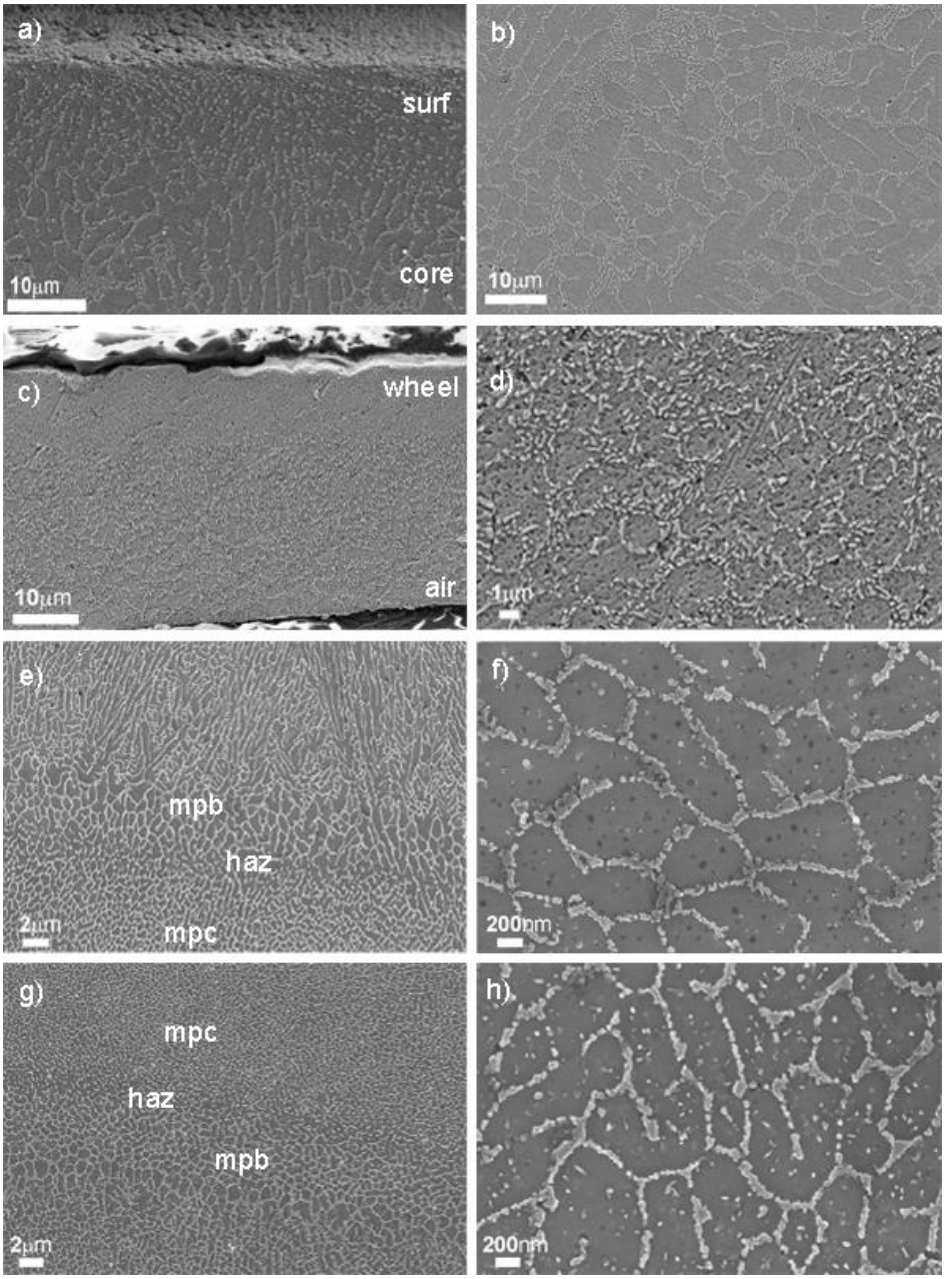

Fig. 3.1 *Micrographs of AlSi10Mg samples obtained by: CMC both on the surface of the cone (a) and in the core (b), MS_N10 at low (c) and high magnification (d), AM_AB at low and high magnification (f) and AM_SR at low (g) and high magnification (h). The white arrows indicate the building direction in the L-PBF process. For comparison an image of the equilibrium microstructure of the AlSi10Mg alloy is reported in* ***Fig. 2.2****.*

The cellular-dendritic structure is to some extent columnar along the building direction following the path of heat subtraction via the substrate [9,19,89,178]. As evident in ***Fig. 3.1-f***, the cells contain occasional Si particles (white contrast) and voids of the same size (dark grey contrast) at points where Si particles were removed by etching.

From the set of images, it is apparent that the amount of Al-Si eutectic differs among various samples. Its percentage was determined by careful image analysis and averaging the results obtained from more than 10 micrographs taken at different magnification. The results obtained are compared with the expected equilibrium value calculated using the lever rule in ***Table 3.3***.

Table 3.3 *Percentage of Al-Si eutectic in samples obtained by means of different rapid solidification techniques. The percentage was evaluated in the core of the sample for CMC, at the air side for MS ribbons and across the whole sample for AM_AB.*

Sample	***Eutectic percentage***
Equilibrium (Phase Diagram)	*75%*
CMC	*34 ± 5%*
MS (average MS_N10 and MS_N15)	*20 ± 1%*
AM_AB	*17 ± 2%*

It is underlined that the microstructure changes when process parameters are modified, since the final result depends on the parameters defining the strategy for the L-PBF process which results in varied temperature gradient, solidification and cooling rate. Therefore, the results reported here on the amount of eutectic are quantitatively valid only for the processing parameters and instrumentation employed to produce the present samples. However, the methodology employed in this work appears well applicable to other sets of parameters.

After annealing for 2h at 300°C for stress relieving samples produced by means of AM, Si particles become coarser and precipitation of new Si particles inside the primary phase occurs, ***Fig. 3.1-h***. Moreover, the heat treatment has a homogenizing effect on the size of Si particles in the matrix, ***Fig. 3.1-g***.

The progressive refinement of the microstructural features with increasing cooling rate is apparent in ***Fig. 3.1*** both from the reduction of the primary Al cells size and the modification of the eutectic from plate-like, characteristic of the equilibrium solidification, to fibrous morphology. In CMC, even if a consistent refinement in the microstructure occurred from the base to the tip of the cone, the microstructure reported in ***Fig. 3.1-a*** and ***Fig. 3.1-b*** is coarser with respect to that obtained with other production routes and part of the eutectic is still lamellar. Full modification of the eutectic occurs both with MS and L-PBF. The portion of MS samples having eutectic morphology (***Fig. 3.1-d***) is similar to that produced by L-PBF, however, primary Al cells are larger.

Samples produced by MS show a peculiar gradient in microstructure from an apparently homogeneous solid solution on the wheel side to a cellular dendritic structure surrounded by Si eutectic on the air side (***Fig. 3.1-c***). The formation of a homogeneous solid solution without solute partitioning indicates the solidification occurred below the T_0 temperature, i.e. the temperature at which the free energies of the liquid and crystalline solutions are equal. The transition from partitionless primary to primary plus eutectic solidification gives clear evidence of the decrease in the solidification front velocity across the ribbon thickness which accompanies the local decrease in cooling rate [99,103]. This is brought about by two events:

i. the formation of a layer of solid solution causes release of latent heat with associated recalescence;
ii. the heat extraction through the quenching medium ceases when the ribbon is detached from it, therefore, cooling by convection and radiation to the surrounding atmosphere occurs.

In the samples produced by L-PBF with the present set of processing parameters, the microstructure is made of fine primary Al cells surrounded by Si eutectic (***Fig. 3.1-e***). The cells are elongated in the areas at the edge of the melt pool which underwent repeated fusion in the subsequent laser scans. Since in these samples there is no evidence of formation of a homogeneous solid solution alone, it is inferred that solidification has occurred above the T_0 temperature. The pre-existing Al-rich crystals are

heterogeneous nuclei upon which cells grow in condition of constitutional supercooling [9] leaving between them a Si-enriched melt which gives rise to the eutectic. The energy injected by the laser beam and the heat released upon solidification is continuously and effectively dissipated by conduction in the cool support and built objects, as suggested by the steady distribution of cell size and eutectic amount in the whole sample at variance to the solidification morphology of the melt spun ribbons.

The fraction of Al primary phase with respect to the eutectic changes substantially in samples produced by means of different rapid solidification techniques as quantified in [179], where increasing eutectic fraction from 20 to 60% were measured in atomized powders of size ranging from 10 to 100 μm. The eutectic fraction is always lower than the expected quantity computed by using the lever rule on the equilibrium Al-Si phase diagram. The Al-Si system has a skewed coupled zone for the eutectic with increasing growth rate [100] entailing the increase in supersaturation of Si in the primary Al. This occurs especially in L-PBF samples due to the high cooling rates achieved in solidification [2,64,74,81,180].

The primary cells as well as the featureless zone of the melt spun ribbons contain clear evidence of the presence of precipitated Si (***Fig. 3.1-d*** and ***Fig. 3.1-f***). It is deduced that it was produced in the solid state because of self-annealing caused by dissipation of latent heat of solidification. Coarsening of Si particles and precipitation of new ones inside the primary phase occur by heat treatment along with homogenization of the microstructure (***Fig. 3.1-g*** and ***Fig. 3.1-h***) in agreement with the literature [9,16,79].

Overall, the microstructure produced in AM is unique, differing from those obtained with established rapid solid solidification techniques. This results from the distinctive action of adding material track after track and layer after layer together with the fast and directional cooling rates obtained in this process also in the solid state.

Face centred cubic Al and diamond cubic Si phases were identified in XRD patterns of all samples. Occasionally, minor reflections of Al_2O_3 were found, i.e. the oxide produced by coalescence into fine particles of the surface skin of the starting powder particles and, possibly, some oxidation occurring in

the building chamber in spite of the protective atmosphere. Fcc Al reflections are always sharp, indicating the presence of large crystallites. Limited evidence of preferred orientation of crystals could be noticed for samples produced by means of CMC and L-PBF by measuring the X-ray line intensity, indicating that, even if columns can be seen in these samples, they are not predominant in the microstructure. The absence of textures in the L-PBF samples is related to the scanning strategy adopted [19], since in other works substantial texturing has been reported [17]. On the air side of samples produced by MS the patterns show preferential orientation on the (111) plane and to a lesser extent the (220) plane, while the wheel side show textures on the (200) plane and to a lesser extent the (311) plane.

Together with the microstructural features reported in ***Fig. 3.1***, these findings confirm the long-standing view that structural inhomogeneities occur in melt spun Al-Si alloys [91,95] in relation with local differences in heat subtraction.

The intensities of diamond cubic Si reflections are low with respect to those of fcc Al in all samples, in ***Fig. 3.2*** are reported the XRD patterns of the AM_AB and AM_SR samples as an example. Moreover, the higher is the cooling rate the broader and lower are the reflections pointing to increased supersaturation and reduced crystallite size. After annealing, Si reflections increase in intensity and become sharper (***Fig. 3.2-a***) [9,176]. Patterns of the L-PBF samples (AM_AB), taken on various surfaces, show enlargements of the (222) and (420) reflections with respect to the (311) and (331) reflections occurring at close angles, respectively (***Fig. 3.2-b*** and ***Fig. 3.2-c***). This result indicates localized strain along those directions possibly caused by solute clusters.

The lattice parameters of the Al-rich phase are reported in (***Fig. 3.3***).

All rapidly solidified samples have smaller lattice parameter with respect to that solidified in equilibrium (dashed line in ***Fig. 3.3***). The lattice constant of the Al phase in ribbons is lower for the wheel side with respect to the air side. After stress relieving, all lattice parameters approach the equilibrium value.

The reflections of fcc Al and diamond cubic Si in XRD patterns (***Fig. 3.2-a***) are now employed as a tool for the interpretation of the events occurring during solidification.

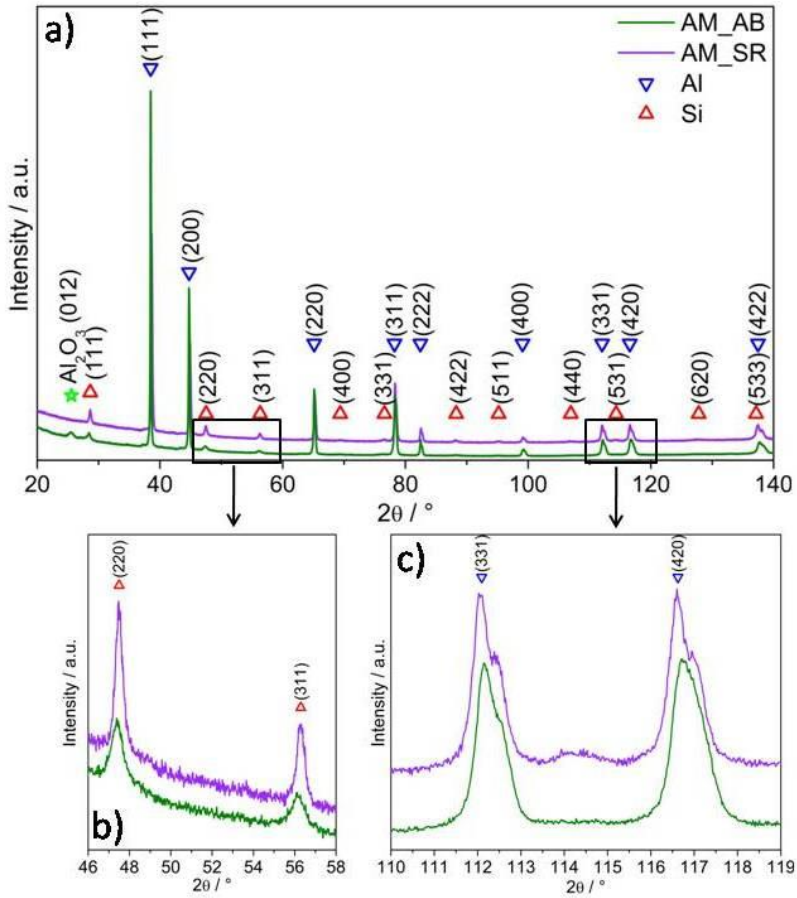

Fig. 3.2 *XRD patterns of AlSi10Mg samples produced by L-PBF before (AM_AB) and after stress relieving (AM_SR), (a). Detail of the (220) and (311) Si reflections, (b). Detail of the (331) and (420) Al reflections, (c).*

The intensity of Si reflections decreases on increasing the cooling rate because of Si supersaturation in the primary phase (***Fig. 3.2-b***).

Within the scatter of results due to the limited number of reflections detectable, the lattice constant corresponds to that of elemental Si. The broadening, much evident in the L-PBF and MS samples, relates to the fine scattering domains present in the Si particles after rapid solidification.

The lattice parameter of the Al primary phase (***Fig. 3.3***) testifies the varied quantity of solute Si. The reference lattice parameter is that of the

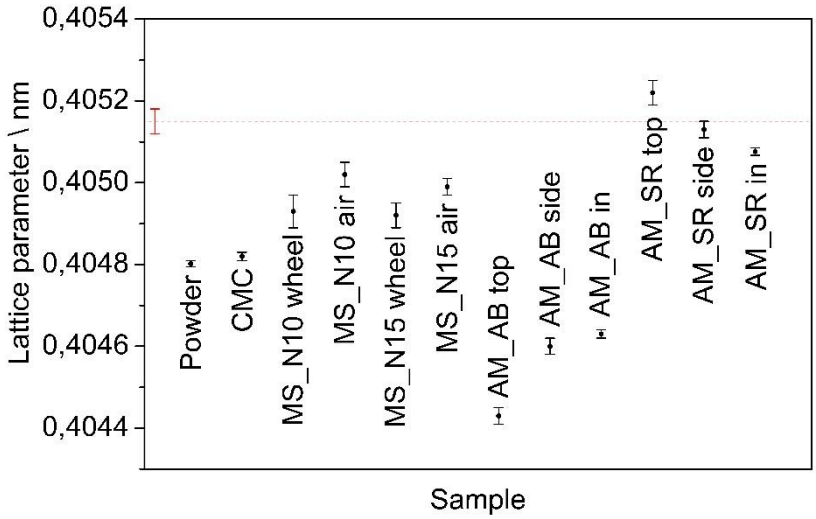

Fig. 3.3 *Comparison of the Al lattice parameter of the samples analysed in the present work. The dashed line corresponds to the reference valuefor an equilibrated alloy.*

equilibrium AlSi10Mg alloy, $0.40515 \pm 0.00003\, nm$, consistently larger with respect to that of pure Al, $0.40494\ nm$ [181]. Considering that solute Si and Fe decrease [181,182] while Mg increases the lattice parameter of Al [181,183], the increment of the equilibrium lattice parameter must be related to the presence of solute Mg in the Al phase. Si and Fe are contained in the eutectic and minority compounds. For all samples produced by means of rapid solidification, the decrement in lattice parameter indicates the excess Si is trapped inside the primary Al [16]. The lattice parameter of AM_AB is the lowest, confirming the high supersaturation of Si already suggested by the results on the percentage of eutectic. It is worth noticing that the lattice parameter corresponding to the top surface of the sample is the lowest of all. This is understood by considering that the last layer is not affected by further scans, while the layers underneath which are accessed when analysing the other surfaces are re-solidified several times. The lattice parameter calculated for the sample produced by L-PBF and subjected to stress relieving treatment are in accordance with what obtained for the sample solidified in equilibrium condition, indicating the complete precipitation of Si from the Al primary phase. It is interesting to notice that the lattice parameters of melt spun ribbons are slightly lower for the wheel

side with respect to the air side but higher with respect to that of the CMC sample, opposite to what expecting considering the cooling rate typically reached with the two techniques. This trend clearly differs from that of the eutectic fraction in the microstructures. The two set of data can be reconciled by considering that the microstructures seen in ***Fig. 3.1*** are the outcome of the solidification processes, whereas the XRD patterns refer to the crystal structure in samples cooled to room temperature. The as solidified CMC and L-PBF samples remain in contact either with the quenching medium or a cool portion of the same alloy down to low temperature: i.e. with a heat sink of high thermal conductivity which extracts heat continuously. On the other hand, in MS an initial fast heat exchange occurs when the molten alloy impinges onto the rotating Cu wheel, then the ribbon detaches from the wheel and the release of latent heat gives rise to recalescence, resulting in precipitation of Si which decrease the level of supersaturation. The occurrence of sharp XRD reflections of Si in patterns taken on the wheel side of ribbons support this reasoning.

The lattice parameter of the starting atomized powder which contain a mixture of primary cells and fibrous eutectic, is also low. Although the occurrence of recalescence phenomena was reported in powders as well [179], the average size of the powder particles is 3-4 μm, about one order of magnitude less than the thickness of ribbons, therefore, the average cooling

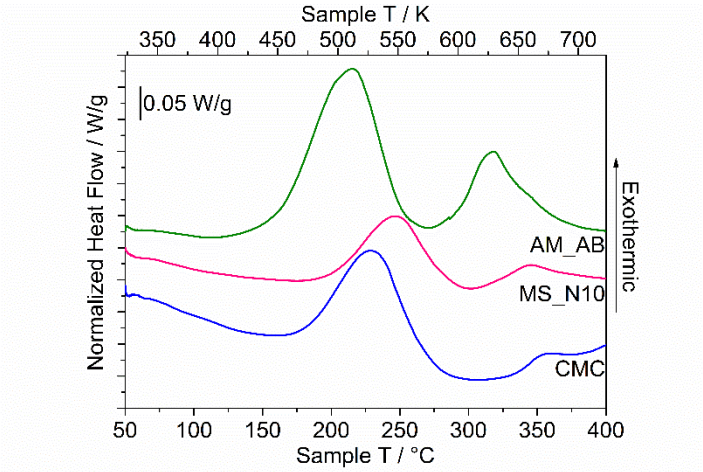

Fig. 3.4 *DSC traces showing precipitation signals for samples produced by CMC, MS (MS_N10) and L-PBF (AM_AB).*

rate of small particles in gas atomization can be faster than the average cooling rate during MS.

Vegard's law was employed to evaluate the amount of Si dissolved in the fcc Al, x_{Si} [94]:

$$a = -0.0174x_{Si} + 0.40515$$

The average concentration of solute Si resulted to be approximately 1 at% in MS samples, 2 at% in CMC samples and 4 at% in L-PBF samples.

DSC signals obtained at the scanning rate of 20°C/min for cast, melt spun and L-PBF samples are reported in ***Fig. 3.4*** and the relevant temperatures for all signals in ***Fig. 3.5***.

Exothermic signals are obtained in each case, the first one being more intense. The first peak of the as built L-PBF sample is centred at approximately 200°C, a second one at 317°C and a third one, seen as a shoulder on the previous signal, at 340°C. The signal at 317°C is present only in the sample produced by means of L-PBF. For the CMC and MS samples the first peak occurs at higher temperature, while the peak at 340°C is invariant

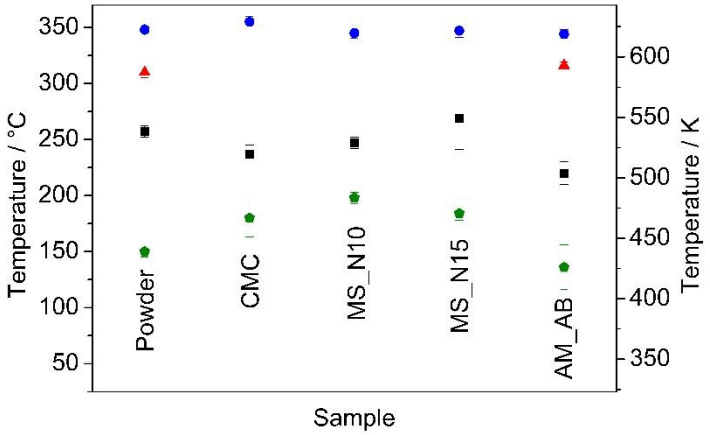

Fig. 3.5 *Comparison of the precipitation temperatures in samples produced by means of different rapid solidification techniques (heating rate of 20°C/min). Pentagons (green) represent the onset temperature for the precipitation of Si; squares (black) the maximum of the Si precipitation signal; triangles (red) the maximum of the Mg_2Si precipitation signal and circles (blue) the maximum of the precipitation signal related to impurities.*

in temperature. The onset and peak temperatures of the first signal rank in the sequence MS > CMC > L-PBF.

The enthalpy released in the first DSC signal changes with processing route: it decreases from 33 ± 9 J/g in L-PBF to 26 ± 2 J/g in CMC and 17 ± 2 J/g in MS samples. The total enthalpy released in the other minor signals of the L-PBF samples is of the order of 8 ± 4 J/g. The high temperature signal for CMC and MS samples provides 1-2 J/g. Since the amount of enthalpy released for the first precipitation signal by the samples produced by CMC and MS has less scatter with respect to that of L-PBF samples, the reproducibility of the L-PBF samples was verified by performing several measurements at 20°C/min with samples produced using the same process parameters in different runs and employing different batches of powder. The resulting thermograms, reported in ***Fig. 3.5***, show differences both among different jobs and parts of the same sample.

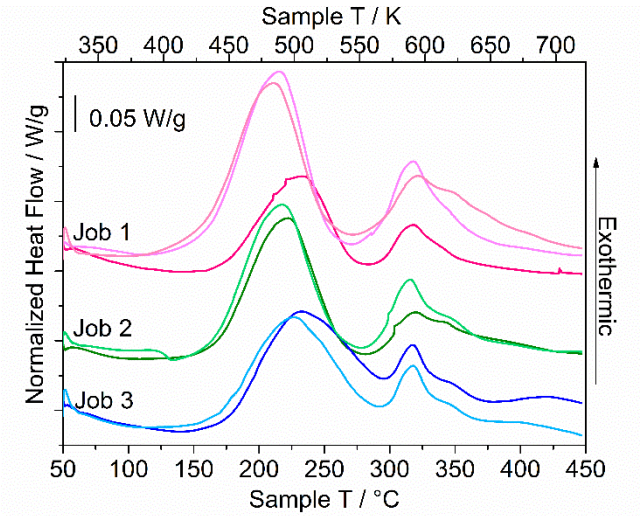

Fig. 3.6 *Thermograms of samples produced by SLM during different jobs and employing different batches of powder but the same process parameters.*

However, all of them have three precipitation signals at around 200°C, 317°C and 340°C. The onset temperatures and heats for precipitation signals are reported in ***Table 3.4***.

Table 3.4 *Temperatures and heats obtained from the DSC thermograms of* ***Fig. 3.5****.*

Job	*Onset peak 1 [°C]*	*Maximum peak 1 [°C]*	*ΔH peak 1 [J/g]*	*Onset peak 2 [°C]*	*Maximum peak 2 [°C]*	*ΔH peak 2 [J/g]*
Job 1a	*166*	*232*	*23*	*284*	*317*	*6*
Job 1b	*156*	*215*	*44*	*271*	*317*	*15*
Job 1c	*155*	*211*	*41*	*272*	*321*	*14*
Job 2a	*164*	*222*	*35*	*281*	*320*	*10*
Job 2b	*162*	*217*	*37*	*278*	*316*	*12*
Job 3a	*169*	*232*	*25*	*296*	*318*	*5*
Job 3b	*169*	*226*	*27*	*292*	*318*	*5*

The first DSC peak, given by all samples, is attributed to the precipitation of supersaturated Si from the primary phase, also in view of the numerous literature findings [81,97,184]. To enforce this, it is noted that a melt spun ribbon produced from an AlSi10 master alloy not containing Mg gave the same precipitation signal. For quantitative discussion of the heat effect, the thermodynamics of the Al-Si system is considered as recently assessed [185]. ***Fig. 3.7*** reports the enthalpy of mixing Si to Al in the fcc structure and the enthalpy of the equilibrium phase mixture (fcc Al and diamond cubic Si). It turns out that the maximum amount of heat that can be released by precipitation of Si from a fully supersaturated alloy containing 10wt% Si is 85 J/g. This value is larger than those of the precipitation enthalpy obtained for the first signal of the present samples, confirming that only a portion of Si was retained in solution. The heat release data concur with lattice parameters results in indicating that the average concentration of solute Si in Al amounts to 1 at% in MS ribbons, 2 at% in the CMC sample and 4 at% in the L-PBF built.

These values are indicative of the general outcome from the diverse solidification processes, although in the samples there might be differences in Si content in neighbouring zones. Remembering that the solubility of Si is 1.8 at% at the eutectic temperature [185], it is confirmed that precipitation

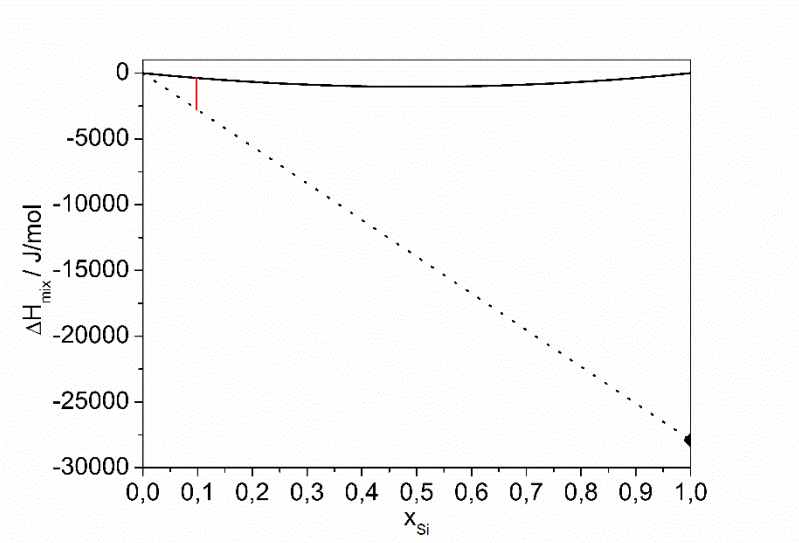

Fig. 3.7 *Enthalpy of mixing (bold curve) and of precipitation (red line) for an Al-10%Si alloy at 25°C (298 K). The dashed line gives the reference state of the mechanical mixture of fcc Al and diamond cubic Si.*

in the solid state soon after solidification takes place in the ribbon, but not in the CMC sample, whereas the L-PBF built is more supersaturated.
Since it has been demonstrated that the Si precipitated already in all samples, at least partially, it is deduced that nucleation of crystals must have occurred, and the heat release is mostly due to the growth by diffusion. The temperature shift can be attributed to two phenomena which can favour Si diffusion:

i. excess Si solute [93],
ii. excess vacancies inside the Al matrix [184,186],

both due to the rapid solidification processing.
The variations in temperature and heat, detectable although limited (***Fig. 3.5***), for different part of the L-PBF samples and different jobs depend on inhomogeneity in the microstructure of as built samples. This is because of inherent fluctuations in powder layer deposition and scanning mode for the skin, the contour and the core. Also, different batches of powder can have different impurity levels. Therefore, although within the general framework just outlined, a certain variability in the results is unavoidable.

These results, however, show that DSC can be considered a very sensitive tool for understanding the local level of supersaturation present in the samples and could help in evaluating the reproducibility of the AM process of Al-Si alloys.
Turning now to discuss the origin of the second DSC signal occurring at 317°C in the samples produced by L-PBF, it is noted that Mg_2Si is a likely precipitate in AlSi10Mg. Considering the enthalpy of formation of Mg_2Si [187], the maximum amount of heat releasable by 1g of an alloy containing 0.35wt% Mg is 8 J/g, i.e. a quantity of the same order of magnitude as the heat measured for the precipitation of Mg_2Si from the primary phase still supersaturated in Mg. This signal is absent in the DSC traces provided by the samples produced by CMC and MS, in spite of the evidence of the presence of Mg deduced from the values of lattice parameters after annealing. It is likely that the solute Mg in these samples corresponds to the equilibrium amount expected in the ternary Al-Mg-Si phase diagram [188,189]. The second DSC peak of the L-PBF samples cannot be separated from the minor one, which is found in all other samples as well. Its enthalpy contribution is limited, probably related to the formation of another precipitate containing impurity elements, e.g. Fe, present in the alloy.

3.2.2. Calculation of the metastable phase diagram

From results obtained, it is apparent that the increment in solidification rate gives origin to the reduction of the volume fraction of eutectic and in increased supersaturation of Si inside the cells of primary Al. To interpret the set of experimental findings, the model for dendritic growth under rapid solidification conditions developed by Kurz and Trivedi in [103] is applied to the Al-Si system.
The model assumes *liquidus* and *solidus* to be linear and is valid for dilute solutions.
According to this model the *liquidus* temperature is expressed as:

$$T_L = T_M + m\left(1 + \frac{k - k_v + k_v \ln\frac{k_v}{k}}{1-k}\right)C_L - \frac{2\Gamma}{r} - \frac{V}{\mu_k}$$

where T_M is the melting temperature of the solvent element, m the *liquidus* slope (dT_L/dC), k the equilibrium distribution coefficient (dC_s/dC_L), with C_s and C_L the solid and liquid composition respectively, Γ the Gibbs-Thompson coefficient, r the dendrite tip (or column, cell) radius, V the rate of interface movement, μ_k the interface kinetic coefficient defined as

$$\mu_k = V_0 \frac{1-k}{m}$$

with V_0 the limiting crystallization velocity of the order of the velocity of sound, and k_v the non-equilibrium distribution coefficient defined by Aziz [190,191] as:

$$k_v = \frac{k + P_i}{1 + P_i}$$

where P_i, the interface Pèclet number for solute redistribution, is defined as

$$P_i = \frac{a_0 V}{D_i}$$

with a_0 representing the interface diffusion length and D_i the interface diffusion coefficient. k_v expresses the deviation from equilibrium conditions on fast solidification and approaches unity when the *liquidus* approaches the T_0 line. The physical constants reported in ***Table 3.5*** were employed to perform the calculation.

Table 3.5 *Physical constants of the Al-Si system employed for the calculation.*

Physical constants employed in the calculation				
$\boldsymbol{T_M}$***(Al)***	*Melting temperature of Al*	*933*	*K*	*[192]*
$\boldsymbol{T_M}$***(Si)***	*Melting temperature of Si*	*1687*	*K*	*[192]*
$\boldsymbol{\Gamma_{Al}}$	*Gibbs-Thompson coefficient of Al*	$1.96{\cdot}10^{-7}$	*Km*	*[100]*
$\boldsymbol{\Gamma_{Si}}$	*Gibbs-Thompson coefficient of Si*	$1.70{\cdot}10^{-7}$	*Km*	*[100]*
$\boldsymbol{a_0}$	*Interface diffusion length*	$1{\cdot}10^{-9}$	*m*	*[100]*
$\boldsymbol{D_i}$***(Al)***	*Interface diffusion coefficient for Al*	$5.45{\cdot}10^{-9}$	m^2/s	*[193]*
$\boldsymbol{D_i}$***(Si)***	*Interface diffusion coefficient for Si*	$8.88{\cdot}10^{-9}$	m^2/s	*[191]*
$\boldsymbol{V_0}$	*Limiting crystallization velocity*	*4879*	*m/s*	*[194]*

In the case of samples produced by L-PBF, the microstructural length scale, R, of the primary phase varies about one order of magnitude in samples produced with different techniques. The growth velocities, however, are not known.

Therefore, an inverse approach was used to calculate both *liquidus* and *solidus* curves for the Al-rich and Si-rich of the phase diagram starting from the known parameters. The aim is to draw a metastable phase diagram with approximate tie lines for the Al-Si system to match the eutectic percentage determined in each microstructure.

The results of calculation are reported in ***Fig. 3.8*** together with the equilibrium phase diagram and T_0 curves determined according to the assessed Al-Si system (TCBIN Thermo-Calc®).

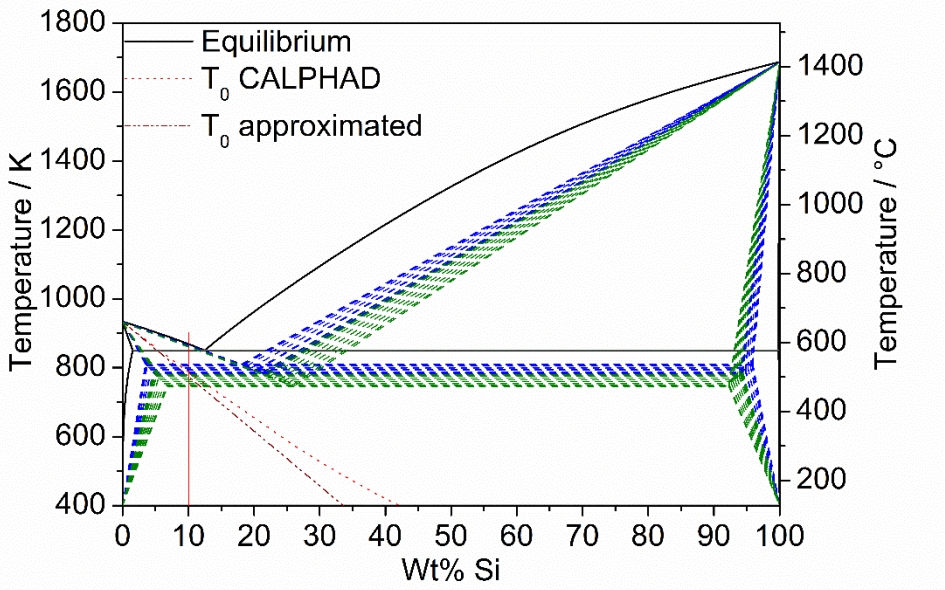

Fig. 3.8 *Equilibrium and approximate metastable phase diagram for Al-Si alloys. The dotted and the dot-dashed lines (light and dark red) in the picture represent respectively the T_0 line calculated with CALPHAD and derived from the model. The T_0 line of the model is obtained by the linear approximation of the liquidus and finds good agreement with the CALPHAD one especially at low Si content. The dashed bands in colour, blue for CMC and green for L-PBF respectively, were obtained for ranges of solidification velocities compatible with the percentage of eutectic observed in microscopy. The vertical red line represents the composition of the AlSi10 alloy.*

The metastable eutectic shifts to higher Si content when the growth velocity and the corresponding cooling rate are increased from the quasi-equilibrium condition to those occurring in CMC and L-PBF.

For each technique, a range of growth rates was assumed in order to reproduce the findings on the respective percentage of eutectic. The results of the calculations show that the rate of interface movement for the L-PBF samples should be comprised between 0.66 and 1.025 m/s. Despite the approximations outlined above, it is remarkable that these growth rates reproduce those found experimentally by recording the interface displacement in Al-Si thin films imaged in TEM during solidification after laser melting [195].

The band for the highest growth rates in ***Fig. 3.8*** intersects the T_0 line of the Al-rich solid solution representing the initial stage of solidification found in MS and CMC samples. For the L-PBF process, the presence of fcc Al crystals as substrate causes fast growth of the primary phase, in epitaxial fashion [17].

Si rejection brings the local composition of the melt to the eutectic which is incorporated into the primary phase. Re-nucleation may then occur at heterogeneous sites.

3.3. Conclusions

In this first part of the thesis, the correlation between the microstructure, the phase constitution and the thermal behaviour of AlSi10Mg samples produced by means of different rapid solidification techniques was established. The cooling rate, i.e. velocity of the solidification front, determines the morphology and size of the microstructural features. In CMC and MS samples, a thin featureless zone indicates that the initiation of solidification occurred below the T_0 line. With the subsequent increase in temperature due to recalescence, the microstructure become mixed, primary plus eutectic.

There is progressive change of the morphology of eutectic Si from dispersed particles to fibrous and lamellar network. The microstructure is more refined in MS with respect to CMC samples and even more in L-PBF parts, which are entirely made of cells or columns of primary Al and fibrous Si eutectic. Together with the change of eutectic morphology, a clear increase in eutectic fraction is found in the order L-PBF > MS (air side) > CMC > master alloy. The decrement of the Al lattice parameter when changing processing technique gives a measure of the extension of solid solubility of Si in the primary phase. The lattice parameter decreases in the sequence: master alloy or annealed samples > MS (all sides) > CMC > L-PBF. The surprising amount of solute Si in CMC samples, corresponding approximately to the solubility at the eutectic temperature, is understood by considering the fast cooling in the solid state after solidification provided by the continuous contact of the sample with the heat sink. This is also the reason for the extension of solubility in L-PBF parts, where the melt pool is in direct contact with the previously solidified material. Accordingly, the low solute content in MS samples must be due to decrease in cooling rate and the consequent self-heating of the ribbon because of recalescence after detaching from the quenching wheel. DSC analysis provided evidence of precipitation of excess solutes in the temperature range from approximately 150 to 350°C (heating rate 20°C/min). The first and main DSC peaks is due to Si precipitation, for which a correlation between the level of extended solid solubility and the onset temperature of the signal was evidenced: the lower is the temperature the

higher is the amount of released enthalpy. Thermodynamic analysis of the Al-Si system confirmed that the released enthalpy corresponds to the level of supersaturation reached in the samples produced by means of different processing routes. Further exothermic signals are attributed to the precipitation of Mg_2Si (signal detected only for L-PBF samples around 317°C, since probably the cooling condition allow the Mg to reach equilibrium in CMC and MS samples) and possibly Fe-containing intermetallics around 340°C. The ensemble of results on eutectic fraction and solubility are interpreted by applying a current model of cellular/dendritic solidification [103], which implies the progressive narrowing of the distance between *liquidus* and *solidus* lines in the phase diagram as a function of the solidification front velocity. Approximated metastable phase diagrams for the front velocities in between 0.5 and 1 m/s reproduce the eutectic fractions found in experiments. Remarkably, these correspond to those directly measured recently [195] by observing the movement of the primary solidification front in Al-Si.

4. Part II: Modification of the AlSi10Mg alloy

4.1. Experimental procedure

4.1.1. Samples preparation of AlSi10Mg modified with hardeners

Samples modified with hardeners were produced mechanically mixing AlSi10Mg, Ag and high purity Cu gas atomized powders provided respectively by EOS GmbH, Topcast and Sandvik Osprey LTD (certificate 22844). The chemical composition of the AlSi10Mg powder recalculated after mixture is reported in ***Table 4.1***.

Table 4.1 *Chemical composition of AlSi10Mg EOS powder and recalculated after addition of 0.5wt% of Ag and 4wt% of Cu. All quantities are reported in wt%.*

Alloy	Si	Fe	Cu	Ag	Mn	Mg	Zn	Ti	Al
AlSi10Mg	*9-11*	*≤0.55*	*≤0.05*	*-*	*≤0.45*	*0.2-0.45*	*≤0.10*	*≤0.15*	*Bal.*
AlSi10Mg+Ag	*8.96-10.95*	*≤0.55*	*≤0.05*	*0.5*	*≤0.45*	*0.2-0.45*	*≤0.10*	*≤0.15*	*Bal.*
AlSi10Mg+Cu	*8.65-10.58*	*≤0.53*	*4*	*-*	*≤0.43*	*0.19-0.43*	*≤0.10*	*≤0.14*	*Bal.*

To verify characteristics and processability of the compositions selected for AM applications, samples were produced both by MS and SST. Melt spun samples were produced ejecting the molten alloy onto a Cu wheel rotating at 10 m/s. SSTs were produced with an EOSINT M270 Dual Mode version adjusting the process window starting from the process parameters already employed to produce AlSi10Mg samples as recently reported in [196,197]. MS ribbons were then characterized and results, when possible, were compared with what obtained from SSTs.

For microscopy samples were embedded in resin, mechanically polished and etched using a 0.5% HF solution (5s) for MS ribbons and diluted Keller solution (20% Keller and 80% distilled H_2O for 10s) for SSTs. A ZEISS SUPRA TM 40 FESEM was employed to get secondary electron imaging and perform compositional analysis. The eutectic fraction was evaluated by careful image

analysis using the software Image J. Electron Back Scattered Diffraction (EBSD) maps were acquired at the Erich Schmid Institute of Materials Science (Austrian Academy of Sciences) in Leoben using a FESEM Zeiss Gemini 1525 possessing an EBSD detector (e^-Flash^{FS}) from Bruker.

XRD measurements were conducted with a PANalytical X'Pert PRO diffractometer by Philips in Bragg-Brentano configuration with the K_α emission line of a Cu filament ($\lambda_{Cu} = 1.5418$ Å). Patterns were acquired in the 2θ range from 20° to 140° at steps of 0.0167°. The lattice parameter of the face centred cubic (fcc) Al was calculated from the patterns with the $\cos\theta\cot\theta$ method.

A TA Q100 DSC was used to characterize the thermal properties of the samples. Measurements were conducted at a heating rate of 20°C/min in a temperature range from 50 to 450°C, equilibrating the heat flux for 15 minutes at each temperature. Scans were also performed up to 660°C and back at the same heating rate in alumina crucibles to monitor the alloy melting and solidification.

Nano-indentation tests were conducted with a Triboindenter 950 (TI950) equipped with a Berkovich tip. For MS ribbons, indentation was performed every 4 μm on a grid having width of 40 μm and variable length according to the specimen thickness. Grids on SSTs were performed covering completely the melt pool spacing the indentation marks of 7.5 μm one from each other. For all samples the load velocity was 100 μN/s, maximum load was fixed to 2.5 mN and kept for 5s. Load charge and discharge was done at the same velocity.

A bulk platelet ($10x10x4.5\ mm$) of the Cu modified alloy was produced by L-PBF and characterized to verify if MS and SST can simulate the properties of samples produced by means of AM. The platelet was produced with an EOSINT M270 Dual Mode version employing the process parameters optimized for SSTs and reported in ***Table 4.2***.

Characterization of the platelet was performed following the same procedure already described for MS and SST samples. For microscopy the sample, embedded in conductive resin and polished, was etched with diluted Keller solution along the *XZ* section. Nano-indentation tests on the *XZ* section of the L-PBF platelet were performed increasing the load to 250 μN/s up to a

maximum load of 2.5 mN for 5s and then decreased at the same rate on a grid having 384 indentations (4 along *X* and 96 along *Z*) distant 10 μm one from each other. Vickers microindentation measurements were performed with a Buehler Micromet 2101 applying a force of 300g for 20s. For each sample results of at least 10 indentations were averaged.

Table 4.2 *Process parameters employed to produce the AlSi10Mg+Cu platelet.*

Process Parameters	
Scan speed [mm/s]	*700*
Laser power [W]	*180*
Hatching distance [mm]	*0.14*
Layer thickness [μm]	*30*
Laser spot size [mm]	*0.10*

4.1.2. Samples preparation of AlSi10Mg modified with inoculants

Samples modified with inoculants were produced in different ways according to the form of the inoculant element. The inoculants selected for the modification of the eutectic were Erbium (Er), nano-TiB_2 and Strontium (Sr). 0.3wt% Er was added in the AlSi10Mg powder in form of Al3Er gas atomized powder (provided by Nanoval GmbH) and the composition was homogenized mechanically mixing the two powders. 0.1wt% nano-TiB_2 was added in form of powder mechanically mixing the AlSi10Mg alloy provided by EOS GmbH with the nano-TiB_2 provided by US Research Nanomaterials, Inc. The master alloy modified with Sr, instead, was produced by arc melting. The first step in the dilution of the AlSi10Mg alloy was the production of an Al10Sr alloy starting from chemically pure Al and chemically pure Sr. This alloy was then mixed in arc melting with the AlSi10Mg powder, gently pressed to form pellets, to obtain the desired amount of Sr, 0.1wt%.

All the mixtures were employed to produce samples by MS by ejecting the molten alloy onto a Cu wheel rotating at 10 m/s.

For microscopy samples were embedded in resin, mechanically polished and etched using a 0.5% HF solution (5s). A ZEISS SUPRA TM 40 was employed to

get secondary electron imaging. The eutectic fraction and the dimension of both Al cells and Si particles were evaluated by careful image analysis using the software Image J.

XRD measurements were conducted with a PANalytical X'Pert PRO diffractometer by Philips in Bragg-Brentano configuration with the K_α emission line of a Cu filament ($\lambda_{Cu} = 1.5418$ Å). Patterns were acquired in the 2θ range from 20° to 140° at steps of 0.0167°. The lattice parameter of the fcc Al was calculated from the patterns with the $\cos\theta\cot\theta$ method.

A TA Q100 DSC was used to characterize the thermal properties of the samples. Measurements were conducted at a heating rate of 20°C/min in a temperature range from 50 to 450°C equilibrating the heat flux for 15 minutes at each temperature. Scans were also performed up to 700°C and back at the same heating rate in alumina crucibles to monitor the alloy melting and solidification.

Nano-indentation tests were conducted with a Triboindenter 950 (TI950) equipped with a Berkovich tip. For MS ribbons indentation was performed every 4 μm on a grid having width of 40 μm and variable length according to the specimen thickness. Load velocity was 100 μN/s, maximum load was fixed to 2.5 mN and kept for 5s. Load charge and discharge was done at the same velocity.

4.2. Results

4.2.1. AlSi10Mg+hardeners

4.2.1.1. Melt spun ribbons

Microstructures of the cross section of the unmodified and Cu and Ag containing ribbons are reported in ***Fig. 4.1*** along with EBSD maps acquired across the whole ribbon thickness.

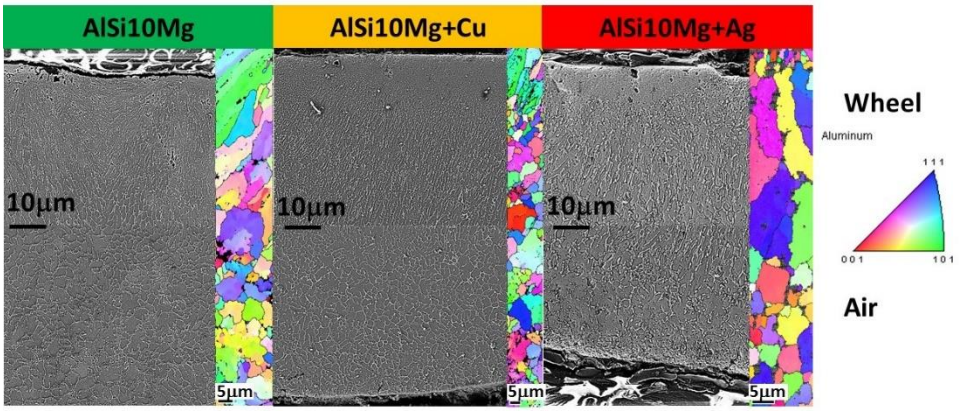

Fig. 4.1 *FESEM micrographs and EBSD maps of melt spun ribbons made of AlSi10Mg, AlSi10Mg+Cu and AlSi10Mg+Ag alloys.*

Both unmodified and modified ribbons display a microstructure made of primary Al cells surrounded by fibrous eutectic, as already observed in chapter 3 for the unmodified alloy, indicating that the presence of Ag and Cu in this amount (0.5wt% and 4wt% respectively) does not alter significantly the microstructural features characteristic of the AlSi10Mg alloy processed by MS.

Also the microstructure of the modified ribbons shows changes from the wheel side, top of ***Fig. 4.1***, where it is almost featureless for a few microns, becoming then primary plus eutectic with separated Si particles and ending on the air side, bottom of ***Fig. 4.1***, with coarser cellular plus fibrous eutectic microstructure.

EBSD maps were acquired to get a better insight on the spatial and crystallographic orientation of Al grains along the cross section of ribbons.

Results obtained suggest that no specific crystallographic orientation is present in the ribbons, however, show that there is a difference in the spatial orientation of Al grains and consequently in solidification when moving from the wheel side to the air side of the ribbons. In fact, in all ribbons EBSD maps show a transition from columnar Al grains at the wheel side to equiaxic Al grains at the air side. This suggests that, during the first stages of solidification, the subtraction of heat occurs through the Cu wheel of the MS apparatus; while, once the ribbon detaches from the Cu wheel, recalescence takes place modifying the solidification conditions and leading to the formation of equiaxic grains. In all ribbons, columnar grains were observed to be tens of microns long, while equiaxic grains were found to have diameters of approximately 5 μm. In all samples the dimensions of the grains detected by EBSD were found to be consistently larger with respect to the dimension of the cells of primary phase observed in the ribbons, having a average diameter of approximately 1.5 μm, confirming that each grain contains several cells of primary phase surrounded by fibrous eutectic.
As previously demonstrated (chapter 3), the amount of primary phase with respect to the eutectic changes substantially in samples produced by means of different rapid solidification techniques. The fraction of eutectic observed in the micrographs of the modified ribbons was calculated and compared with that obtained for the AlSi10Mg alloy. The results, reported in ***Table 4.3***, show that, as expected, in all samples the amount of eutectic is consistently lower than the quantity expected from the application of the lever rule on the equilibrium Al-Si phase diagram, suggesting the presence of Si supersaturation.

Table 4.3 *Al-Si eutectic percentage calculated through image analysis in AlSi10Mg samples without and with Ag and Cu additions.*

Sample	***Eutectic percentage***
AlSi10Mg	*20 ± 2%*
AlSi10Mg+Ag	*21 ± 5%*
AlSi10Mg+Cu	*30 ± 5%*

In detail, the sample containing Ag shows a eutectic percentage comparable to that observed for the AlSi10Mg ribbon without additions, while the sample

containing Cu displays more eutectic with respect to the other two. The presence of Ag was found not to alter the eutectic fraction of the ribbon, because according to the ternary phase diagram at this composition all the Ag is solubilized in the Al matrix. The increased percentage of eutectic observed in the sample containing Cu, was explained considering that, even if at this concentration the alloy is not in the condition to form a ternary eutectic [198], during the rapid solidification process the Cu is rejected from the primary phase and starts forming intermetallics with Al, enlarging the perception of the eutectic observed.

XRD measurements, ***Fig. 4.2***, confirm what suggested from the microstructural observation.

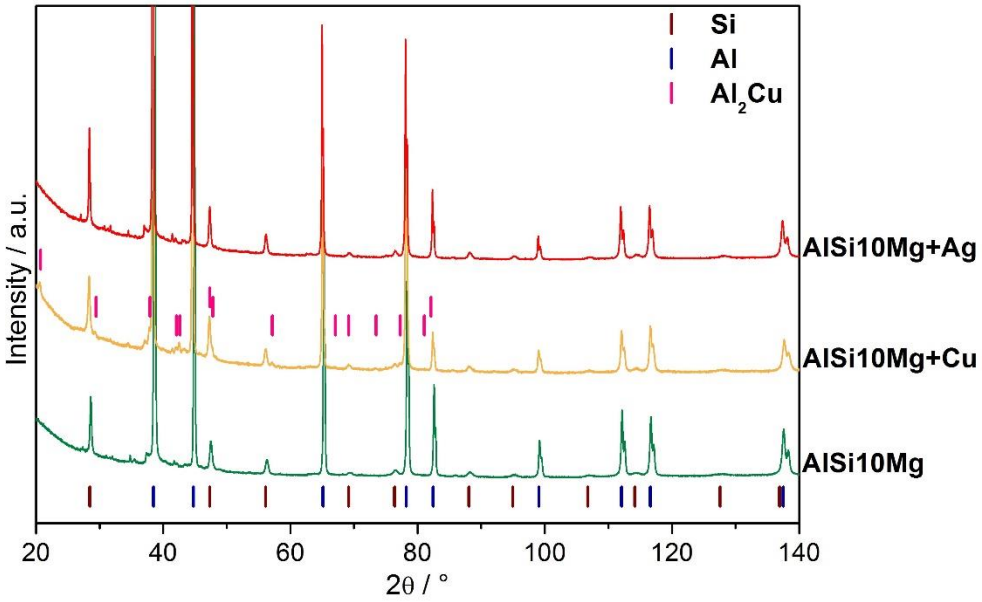

Fig. 4.2 *XRD patterns of the AlSi10Mg (green), AlSi10Mg+Cu (yellow) and AlSi10Mg+Ag (red) along with Al, Si, and Al_2Cu reflections.*

The patterns related to AlSi10Mg and AlSi10Mg+Ag display only reflections related to fcc Al and diamond cubic Si; in the ribbon containing Cu, instead, apart from these two phases also reflections of the body centred tetragonal (bct) θ phase (Al_2Cu) were indexed.

The effect of Ag and Cu additions on the AlSi10Mg alloy was evaluated through Al lattice parameter calculation. The results obtained from both wheel side an air side of all the ribbons are reported in ***Fig. 4.3***.
All ribbons display a lattice parameter lower than the reference one, i.e. a piece of AlSi10Mg ribbon annealed for 2h at 300°C. Moreover, it was evidenced that Ag addition does not alter the lattice parameter of the AlSi10Mg alloy, while the Cu containing alloy lowers it.

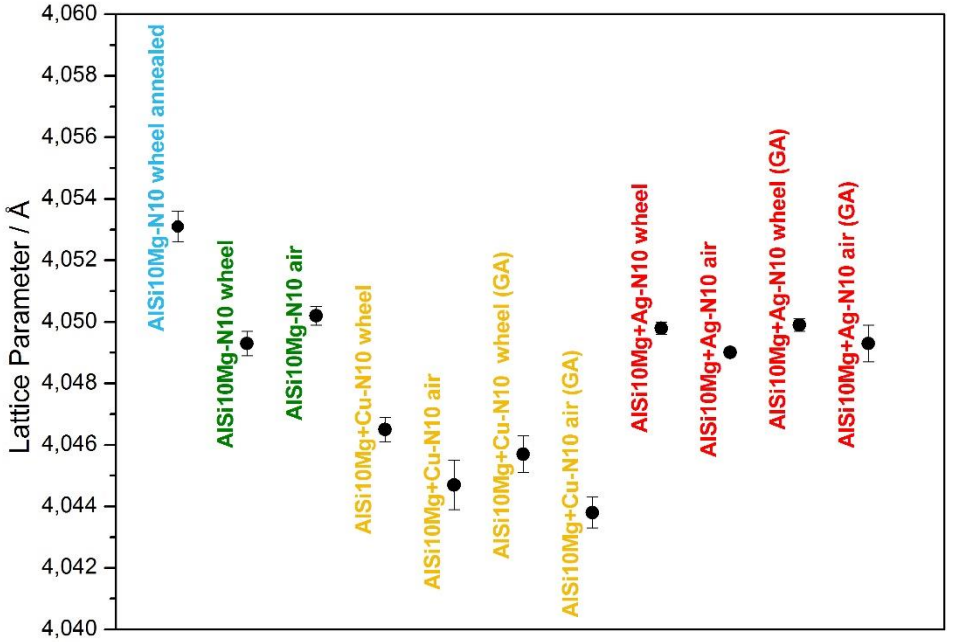

Fig. 4.3 *Comparison of the lattice parameters measured both on the air side and on the wheel side of the unmodified (green), Cu containing (yellow) and Ag (red) containing ribbons. The suffix (GA) indicates that the measurements were performed in Grazing Angle condition so limiting the penetration of the X-rays to few microns.*

This result agrees with what reported in literature on the effect of Ag and Cu on the Al lattice parameter [181,183], where it is stated that Cu and Si supersaturation decreases the lattice parameter of Al, while Mg increases it and Ag leaves it approximately unchanged. All ribbons were found to display a slight difference in the value of lattice parameter from wheel to air side. This difference can probably be associated to a gradient in supersaturation,

expected when considering the heat profile across the sample thickness deriving from the varied solidification condition in melt spun ribbons.

Assuming no ternary interaction and knowing the effect that each element solubilized in the Al has on its lattice parameter, it was possible to estimate the level of supersaturation by applying the Vegard's law. In the alloy modified wit Ag, it is possible to attribute all the reduction in lattice parameter to Si due to the limited effect of Ag in modifying the Al cell. In the case of the alloy modified with Cu instead the reduction can be attributed both to Si ($1.74 \cdot 10^{-4}$ nm/at%) and Cu ($4.77 \cdot 10^{-4}$ nm/at%).

Since in all alloys there are indications of supersaturation, alloys were analysed by means of DSC. A comparison of the DSC signals obtained for the three alloys is reported in ***Fig. 4.4***.

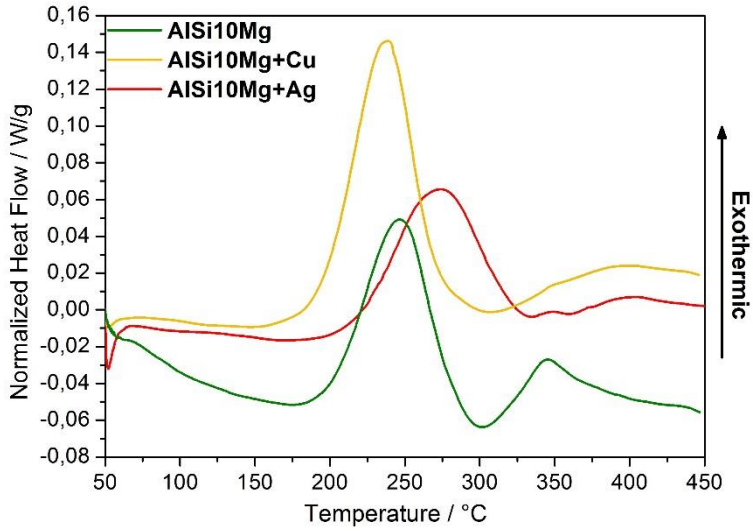

Fig. 4.4 *Comparison of the DSC traces showing the precipitation signals for the three alloys under study. In green is reported the precipitation trace of the AlSi10Mg alloy, in red the one related to the AlSi10Mg+Ag alloy and in yellow the track related to the AlSi10Mg+Cu alloy.*

In all samples two exothermic signals were identified the first one being more intense. The temperatures at which these signals occur agrees with the precipitation sequence already determined for the AlSi10Mg alloy reported in chapter 3**.**

The signal at lower temperature was associated primarily to Si precipitation also for the modified alloys, while the signal at higher temperatures was always correlated to the presence of Mg and other impurities (e.g. Fe) in the alloys. Si precipitation signal occurs at different temperatures, while the signal associated to the minority compounds appears invariant in temperature. This is related to the different supersaturation levels that can be found in the different samples and to the diverse amount of excess vacancies quenched in the samples during the rapid solidification processing [93,184,186]. The enthalpy released in the first exothermal process for the different alloys is 17 ± 2 J/g in the AlSi10Mg ribbon, 13 ± 2 J/g in the AlSi10Mg+Ag ribbon and 25 ± 7 J/g in the AlSi10Mg+Cu ribbon. The enthalpies of unmodified and Ag containing alloys are in accordance, confirming that all the contribution to the first signal is related to Si precipitation [81,97,179]. The lower enthalpy associated to the sample containing Ag agrees with the higher onset temperature of the precipitation signal and is probably correlated to a lower Si supersaturation in the portion of sample analysed. The high enthalpy of precipitation observed in the Cu containing sample, instead, is probably related to the fact that, in the same temperature range of Si precipitation, it is possible to have also the precipitation of Al-Cu intermetallics from the supersaturated solid solution, [199]; therefore the DSC signal observed must account also for the formation of Al-Cu compounds.

To verify the effectiveness of Ag and Cu addition in strengthening the AlSi10Mg alloy, nano-indentation tests were performed covering completely the cross section of the ribbons from wheel to air side. In ***Fig. 4.5*** are reported the nanoindentation maps obtained for all alloys.

From ***Fig. 4.5***, it is evident that hardness values in all samples were homogeneous across all the ribbon.

The average hardness values obtained for the three ribbons are 1.7 ± 0.2 GPa, 2.4 ± 0.4 GPa and 1.5 ± 0.1 GPa respectively for the AlSi10Mg, the

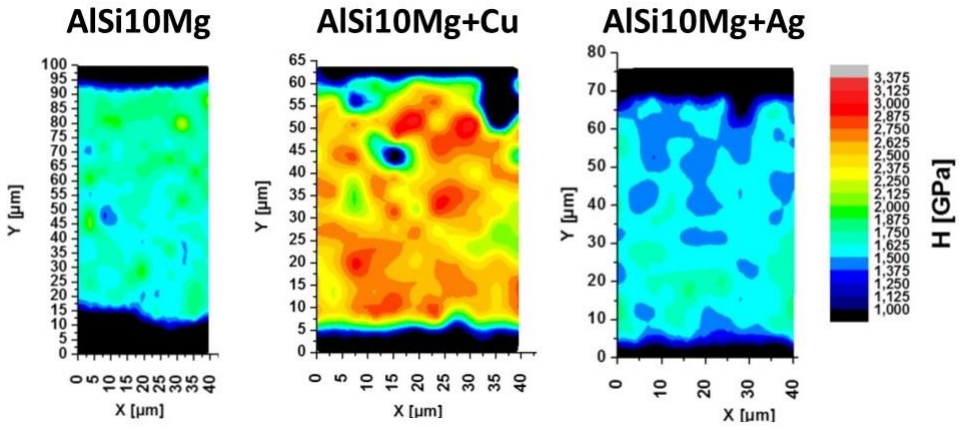

Fig. 4.5 *Nanoindentation maps obtained on the AlSi10Mg alloy (left), AlSi10Mg+Cu alloy (centre) and AlSi10Mg+Ag (right). Hardness values are represented according to the colour scale reported in the image.*

AlSi10Mg+Cu and the AlSi10Mg+Ag alloys. So, as evident from the colour scale in ***Fig. 4.5***, only the sample containing Cu leads to a consistent improvement in hardness, while Ag addition seems to be unable to provide strengthening at least in the as spun condition.

4.2.1.2. Laser Single Scan Tracks

In parallel to the characterization of melt spun samples, measurements were conducted also on Laser Single Scan Tracks.

These were employed as a first step to determine the best process parameters for the production of bulk components through L-PBF, but were also characterized to evaluate if alloys processed under the laser beam provide results in accordance to what determined through MS.

The microstructures of the cross sections of SSTs on both unmodified and modified alloys are reported in ***Fig. 4.6***, along with the microstructural features observed on the air side of melt spun ribbons.

As melt spun samples, melt pools display a microstructure made of cells of primary phase surrounded by fibrous eutectic. In SSTs the microstructure is not homogeneous, in fact areas having finer and coarser microstructures are recognized. The dimensional variation of the microstructural features inside

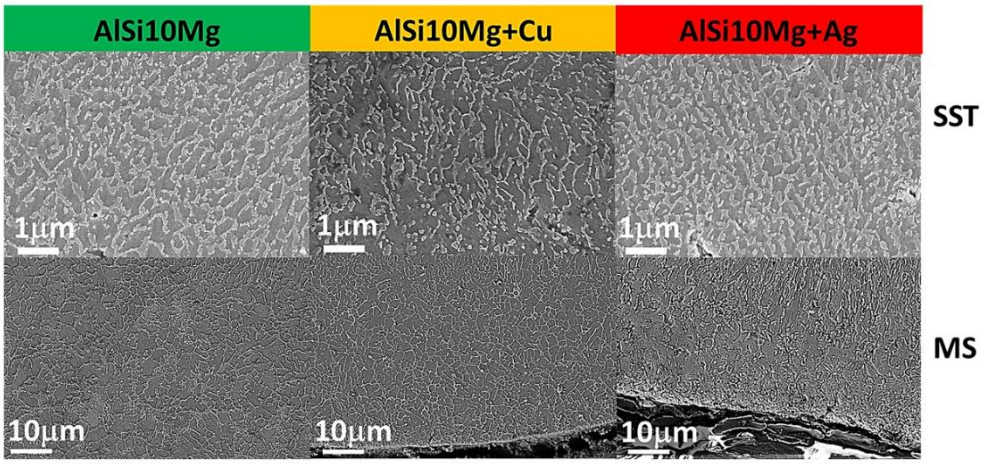

Fig. 4.6 *Microstructures of AlSi10Mg (left), AlSi10Mg+Cu (centre) and AlSi10Mg+Ag (right) samples produced by SSTs (top) and MS (bottom). Images of MS samples represent the air side of the ribbon for all the compositions.*

the melt pools can be understood considering the Marangoni effect, consisting in convective motions arising in the melt pool during L-PBF processes as widely reported in literature [63,64,75,82,85,105]. In SSTs cells of primary phase have an approximate dimension of 1 μm, slightly smaller with respect to what observed in melt spun ribbons. This agrees well with the method of heat subtraction occurring in the two processing techniques; in fact, while in MS the ribbon detaches from the cold medium during solidification, in SSTs the alloy is continuously in contact with the heat sink allowing an efficient heat transfer during solidification.
The fraction of eutectic observed in SSTs, along with that of melt spun ribbons is reported in ***Table 4.4***.

Table 4.4 *Al-Si eutectic percentage in AlSi10Mg samples without and with Ag and Cu additions for both Laser Single Scan Tracks and melt spun ribbons.*

Alloy	***SST***	***MS***
AlSi10Mg	*23 ± 3%*	*20 ± 2%*
AlSi10Mg+Ag	*24 ± 4%*	*21 ± 5%*
AlSi10Mg+Cu	*25 ± 4%*	*30 ± 5%*

The eutectic fraction obtained in SSTs was found to agree with that of the corresponding MS ribbon, the value obtained for the alloy containing Cu

being the highest because of the formation of Al-Cu intermetallics interconnected with eutectic Si.
XRD and DSC analyses were not performed on SST samples, since it would be impossible to eliminate the contribution of the substrate onto which they are produced.
In ***Fig. 4.7*** are reported the indentation maps obtained by analysing the cross section of the SSTs for both samples without and with Ag and Cu additions.

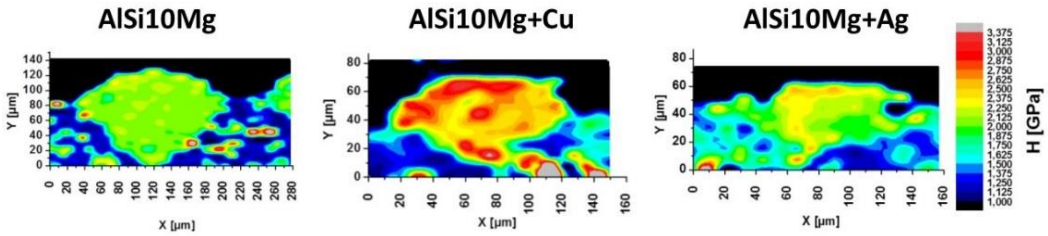

Fig. 4.7 *Nanoindentation maps of the SSTs cross section for AlSi10Mg, AlSi10Mg+Cu and AlSi10Mg+Ag respectively left, centre and right in the image.*

The average hardness values obtained for SSTs are 1.8 ± 0.3 GPa for the AlSi10Mg alloy, 2.0 ± 0.4 GPa for the AlSi10Mg+Ag alloy and 2.5 ± 0.5 GPa for the AlSi10Mg+Cu alloy. As observed in section 4.2.1.1 for the melt spun ribbons, the larger increase in hardness is observed for the alloy modified with Cu. In the sample modified with Ag, hardness values are close to those obtained on the unmodified alloy, indicating that Ag does not strengthen effectively the starting alloy in this amount and directly after rapid solidification.
Through these results, it was possible to state that Cu addition is promoting the most effective strengthening effect to the AlSi10Mg alloy already after rapid solidification. For this reason, only the Cu containing alloy was selected to produce a bulk platelet through L-PBF.

4.2.1.3. L-PBF bulk platelet

An AlSi10Mg+Cu platelet was built using the same powder mixture already employed to produce the previous samples and fully characterized. The microstructures of the AlSi10Mg+Cu alloy produced as SST (a-b), MS ribbon (c-d), and L-PBF platelet (e-f) are shown in ***Fig. 4.8*** both at low and high magnification.

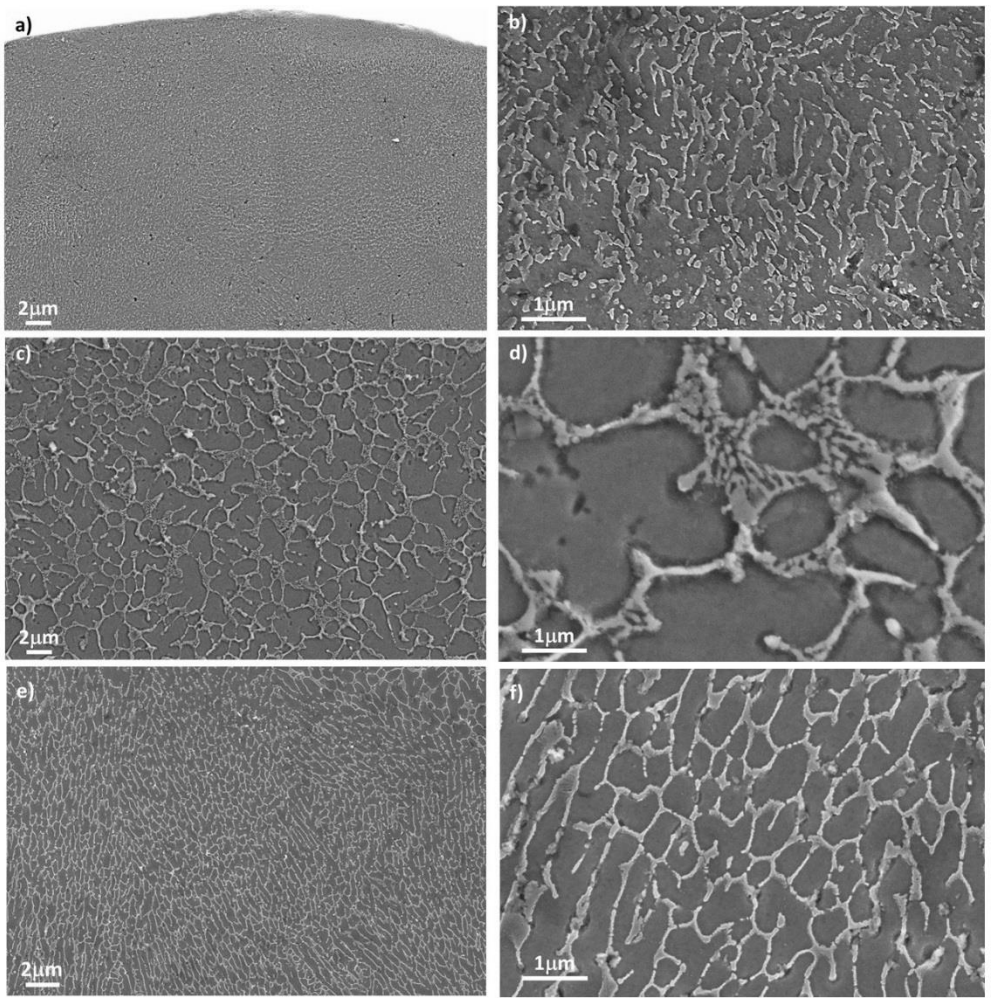

Fig. 4.8 *FESEM images of the cross section of AlSi10Mg+Cu samples: SST (a and b), the air side of the MS ribbon (c and d), and the L-PBF platelet (e and f), respectively at low and high magnifications.*

In all samples primary Al cells are surrounded by Al-Si eutectic (***Fig. 4.8***). The average cell size and eutectic percentage observed in the samples are reported in ***Table 4.5***.

Table 4.5 *Diameter of the primary cells and eutectic fraction of AlSi10Mg+Cu samples produced by means of different rapid solidification techniques: SSTs, L-PBF and MS. For the melt spun sample data refer to the largest portion of the ribbon away from the wheel side.*

Sample	***Cells diameter [μm]***	***Eutectic fraction***
SST	*0.4 ± 0.3*	*25 ± 4%*
L-PBF	*0.8 ± 0.4*	*27 ± 1%*
MS	*1.4 ± 0.7*	*30 ± 5%*

In the case of SSTs the eutectic is almost completely fibrous (***Fig. 4.8-b***), whereas in the *XZ* plane of the L-PBF platelet and in the MS ribbon some areas made of lamellar eutectic are found (***Fig. 4.8-d*** and ***Fig. 4.8-f***). The typical gradient in microstructural features of the MS ribbon is found here in the form of a change in cell size, which is of the order of 400-500 nm in a 20-30 μm thick region on the wheel side becoming then homogeneous around 1.4 μm in the remaining two thirds of the ribbon. Substantial differences emerge in the microstructural features of samples made by laser melting:

i. the size of the α-Al cells is finer in the SSTs whereas the amount of eutectic appears similar;
ii. the cell morphology in the SSTs sample is inhomogeneous in comparison to that of the other samples.

Its irregular shape suggests that solidification here has occurred in front of a turbulent melt. Apparently the strong convective motion of the liquid [63,64,82,105] favoured frequent re-nucleation of crystals and their growth along different paths, contrary to the regular cell-eutectic sequence originating from a relatively quiescent melt in the L-PBF and in the MS sample. In terms of cell size, the L-PBF sample is intermediate with respect to the SSTs and the MS ones. The latter is considered as a reference for solidification of unstirred melt in absence of external heating source. The MS

ribbon starts solidifying on undercooling as fine primary solid solution and eutectic, but very soon recalescence, due to the release of latent heat, reduces the rate of heat transfer also because of the detachment of the ribbon from the quenching wheel, and the length scale of the microstructure is definitely increased as a consequence of the decreased cooling rate [176,200]. The microstructure in the L-PBF platelet appears similar to that of the MS sample, although with reduced length scale. This indicates that solidification of the undercooled melt occurs after the laser has moved away from the molten pool, which encompasses melting of the powder layer together with portions of the previous layers. Solidification takes place via epitaxial growth of the primary phase from the underlying solid, Si segregation and frequent eutectic re-nucleation. The melt remains always in intimate contact with the heat sink underneath which provides continuous heat transfer during the whole cooling time.

The samples resulting from the addition of Cu to AlSi10Mg have eutectic fraction in between 25% and 30%, larger with respect to the base alloy in which the eutectic fraction was 17% in L-PBF and 20% in MS, see chapter 3. This is because Cu was only partially supersaturated in the primary phase as shown by the change in its lattice constant. It was segregated to a large extent in the last solidifying melt and remained in the eutectic zone as Al_2Cu compound (see XRD pattern in ***Fig. 4.9***). Therefore, the eutectic fraction in these samples should be better considered as the intermixing of eutectic Si and Al_2Cu secondary phase. EDX measurements performed on the cross section of MS and L-PBF samples, ***Fig. 4.10-a*** and ***Fig. 4.10-e***, confirm that Cu is preferentially and homogeneously located in zones outside the cells, interconnected with the eutectic Si in both samples. It is underlined that the composition of the present alloy is away from that of the ternary Al-Si-Cu eutectic, although the metastable solidification process causes its formation in all samples. The differences and similarities in microstructure are useful in the detailed understanding of the mechanism of phase formation.

The EDX maps in ***Fig. 4.10-c*** show local irregular distribution of Cu in some areas of the SST sample, apparently because of incomplete mixing with the base alloy in spite of turbulent flow. However, it is underlined that Cu is present everywhere in the sample at the micron scale indicating that SST

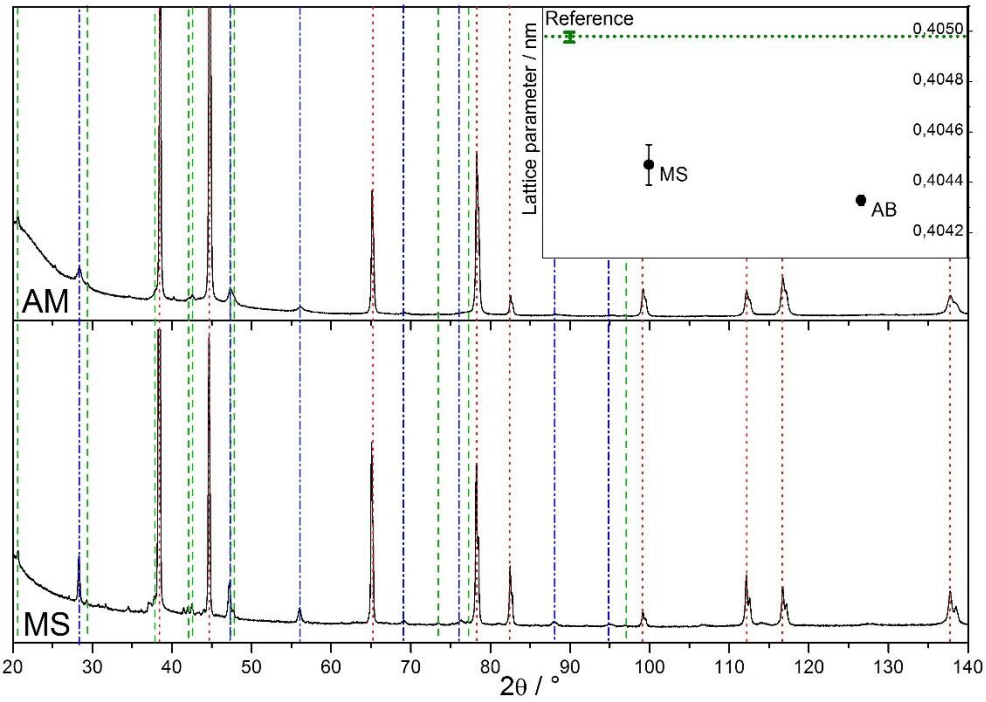

Fig. 4.9 *XRD patterns of the AlSi10Mg+Cu alloy produced both by MS and LPBF. The dotted red lines represent fcc Al reflections, the dot-dashed blue ones diamond cubic Si and the dashed green lines the tetragonal θ phase. The inset represents the variation of Al lattice, calculated through the $\cos\theta\cot\theta$ method, in samples produced by MS and L-PBF.*

produces substantial homogenization of the alloy originated from the mixture of powders. The L-PBF platelet results fully homogeneous within the resolution of the EDX measurement.

XRD patterns made on the air side of the MS ribbon and on the inner *XZ* surface of the L-PBF platelet (***Fig. 4.9***) display reflections due to the fcc Al, diamond cubic Si and bct θ phase (Al_2Cu), as described in section 4.2.1.1. The Si reflections of the MS sample are sharper and more intense with respect to those of the L-PBF platelet. This reproduces the findings on the AlSi10Mg alloy, where larger supersaturation of Si was found in the primary phase of L-PBF samples whereas thickening of the eutectic Si particles and Si precipitation in primary Al occurred in MS ribbons, the latter effects being apparently caused, respectively, by recalescence and self-annealing of the ribbon during slow cooling in the solid state.

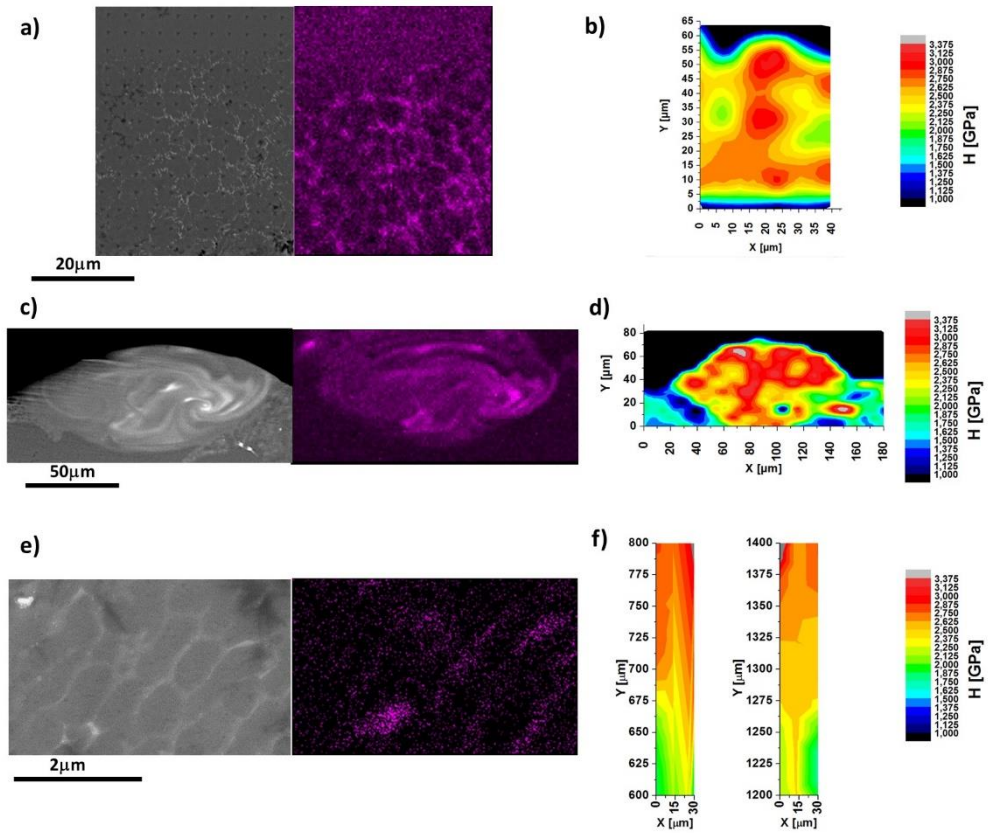

Fig. 4.10 *Images and EDX maps of Cu distribution acquired respectively on the cross section of MS ribbon, SST and L-PBF (along the XZ plane) samples (a, c and e) and nanoindentation maps of the same cross sections (b, d and f): for L-PBF sample the full height of the platelet was tested, and two representative portions of the results are shown.*

The lattice parameter of the Al rich phase of both L-PBF and MS samples is reported in the inset of ***Fig. 4.9***. All values are lower than that of the annealed sample used as reference indicating supersaturation. Both Si and Cu are reported to decrease the lattice parameter of Al, although with different efficacy, following rather well Vegard's law [181,183]: the decrease in Al lattice constant is $1.74 \cdot 10^{-4}$ nm/at% for Si and $4.77 \cdot 10^{-4}$ nm/at% for Cu. Assuming that Si supersaturation in AlSi10Mg+Cu is of the same order of magnitude as that in the base alloy (about 1% and 4% in the MS and L-PBF

samples respectively, chapter 3) and no ternary effect on the lattice constant, Cu supersaturation in the Al phase should be in between 0.75% and 1%, respectively, i.e. limited by the copious formation of the Al_2Cu phase from the melt.

Precipitation reactions should occur from the supersaturated solid solution in MS and L-PBF samples, which are well evidenced by the DSC signals obtained for AlSi10Mg+Cu alloys reported in ***Fig. 4.11***.

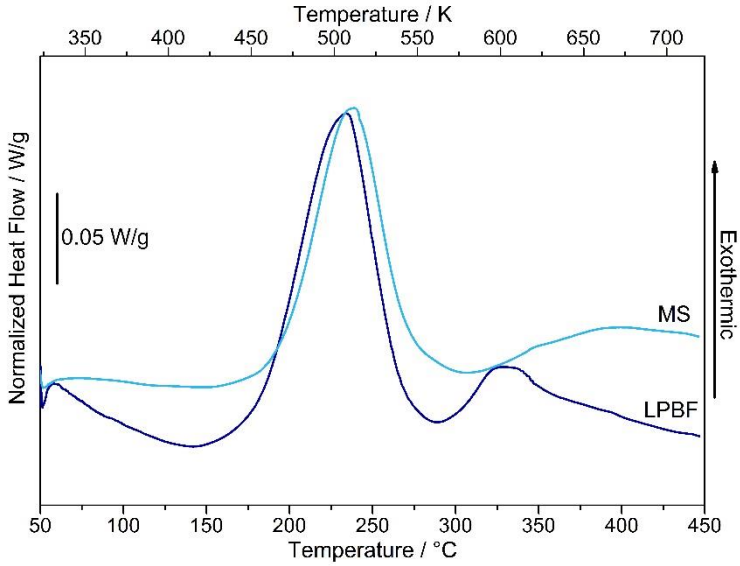

Fig. 4.11 *Comparison of the DSC traces showing precipitation signals obtained for the AlSi10Mg+Cu alloy produced by MS and L-PBF.*

In the case of L-PBF platelet, two exothermic peaks are recorded, the first one being more intense. The temperature at which these signals occur is in accordance with the precipitation sequence already determined for the AlSi10Mg alloys in chapter 3. The signal centred at 225°C is associated to Si precipitation. It must be noted that, as already described in section 4.2.1.1, in the same temperature range the precipitation of the Al-Cu intermetallics from the supersaturated solid solution was reported in literature [199], therefore the DSC signal must account also for the formation of the Al-Cu compounds. The DSC signal occurring at higher temperature are associated to the precipitation of minority compounds (e.g. Mg_2Si and phases containing impurity elements present in the alloy). The absence of the second

precipitation signal in the MS sample could be related to loss of Mg during alloy re-melting.

The enthalpy released in the first exothermal process is close: 25 ± 7 J/g in MS ribbons and 26 ± 3 J/g in the L-PBF sample, at variance with the base AlSi10Mg alloy for which values of 17 ± 2 J/g and 33 ± 9 J/g were found, respectively. Using assessed thermodynamic databases for Al alloys [201], the enthalpy difference between equilibrium phase mixtures and supersaturated solid solutions in Al-Si and Al-Cu systems in the composition range relevant for the present alloys, are 229 J/at% (8.5 J/g) and 633 J/at% (23.5 J/g), respectively. Therefore, although the contribution of the two reactions cannot be singled out, it is apparent that the precipitation of Cu compounds does contribute to the overall enthalpic effect in spite of the low supersaturation because of its larger formation enthalpy. The supersaturation in both Si and Cu in the rapidly solidified samples suggests the possibility of setting up *ad hoc* thermal treatments to induce precipitation hardening provided the microstructure obtained in solidification is preserved.

The melting of the modified alloy occurs in the temperature range between 545 ± 5°C and 583 ± 3°C. These values agree with the *solidus* and *liquidus* points reported in the recently assessed Al-Si-Cu phase diagram [202] within a few degrees which account for the present impurity content. The solidification at the fixed heating rate of 20 K/min of the DSC cell starts on undercooling at 562 ± 1°C and ends at 545 ± 3°C. The alloy melts/solidifies in limited temperature ranges which is a main condition to reduce the chance of developing cracks during solidification, a well-established problem in Additive Manufacturing of Al alloys especially of the 2xxx and 7xxx series [63]. Actually, no evidence of cracks is present in the images of the L-PBF in ***Fig. 4.8***, nor is there in the MS and SST samples although cracking here is much less likely.

Nano-indentation was performed to explore the mechanical properties of the samples. Results are visually highlighted in form of maps in ***Fig. 4.10***. The average hardness values are comparable for SST, MS and L-PBF samples: i.e. 2.7 ± 0.4 GPa, 2.4 ± 0.4 GPa and 2.4 ± 0.8 GPa, respectively; but there is a difference in the distribution of the harder phase (see colours in maps of

Fig. 4.10-b, ***Fig. 4.10-d*** and ***Fig. 4.10-f***) being the colour distribution and, consequently, the hardness more homogeneous in the MS and L-PBF samples with respect to the SST ones. This is due to the local inhomogeneous Cu distribution outlined above. Fluctuations in hardness observed across the *XZ* plane of the L-PBF platelet do not appear to follow any trend and are probably related to different amount of Cu compounds encountered in different zones of the sample. A significant increase in hardness with respect to that of the base AlSi10Mg alloy produced by MS is found (1.8 ± 0.3 GPa, the indentation map from which was obtained this value is reported in ***Fig. 4.5***). The slightly higher value of the SST sample can be attributed to the finer microstructure.

The effect of Cu addition was further established with conventional Vickers hardness measurements carried out on the *XZ* plane of L-PBF samples made of both AlSi10Mg and AlSi10Mg+Cu alloys in comparison with MS samples. The resulting excess in hardness of the Cu-added alloy, ***Table 4.6***, confirm the results obtained with nanoindentation, showing the higher hardness of the Cu-added alloy and the reproducibility of the effect in all samples. The overall increase in hardness with respect to the base alloy appears to be related to the larger amount of eutectic-like fraction since the crystal size and solute supersaturation are similar.

Table 4.6 *Comparison of Vickers hardness and hardness derived from nano-indentation for both AlSi10Mg and AlSi10Mg+Cu samples produced by L-PBF, MS and SST. Of course, due to the limited dimensions of the tracks hardness measurements on SSTs were performed only with nano-indentation.*

Sample	***Vickers Hardness [HV]***	***Nano-indentation [GPa]***
AlSi10Mg L-PBF	*137 ± 13*	*2.0 ± 0.2*
AlSi10Mg+Cu L-PBF	*152 ± 5*	*2.4 ± 0.8*
AlSi10Mg MS	*133 ± 4*	*1.8 ± 0.3*
AlSi10Mg+Cu MS	*162 ± 8*	*2.4 ± 0.4*
AlSi10Mg SST	-	*1.8 ± 0.3*
AlSi10Mg+Cu SST	-	*2.7 ± 0.4*

4.2.2. AlSi10Mg+inoculants

In ***Fig. 4.12*** are reported the micrographs of the AlSi10Mg ribbon along with those of the ribbons modified with the addition of different inoculants (Er, nano-TiB_2 and Sr). In ***Fig. 4.12-a*** is reported the low magnification micrographs of the unmodified AlSi10Mg alloy. As already discussed in chapter 3 in the ribbon there is a gradient in microstructure resulting in featureless microstructure at the wheel side (bottom of ***Fig. 4.12-a***) and in cellular primary phase of increasing dimensions surrounded by fibrous eutectic moving towards the air side (top of ***Fig. 4.12-a***). The eutectic Si network here appears to be continuous around the cells and in some areas lamellar eutectic can be observed, ***Fig. 4.12-b***. All ribbons modified adding conventional inoculants display differences with respect to the unmodified alloy. The ribbon containing 0.1wt% of Sr is the most similar to the AlSi10Mg ribbon showing a microstructure made of α-Al cells surrounded by Si eutectic (***Fig. 4.12-g*** and ***Fig. 4.12-h***). In this case a featureless microstructure is no longer observed at the wheel side, but at both air side and wheel side the microstructure appears finer for a few microns (***Fig. 4.12-g***). At higher magnification (***Fig. 4.12-h***) it is possible to notice that even if the microstructure is close to that of the unmodified ribbon the eutectic Si network around the primary phase appears to be more disrupted. This effect become even more evident in the ribbons modified with Er (***Fig. 4.12-c*** and ***Fig. 4.12-d***) and nano-TiB_2 (***Fig. 4.12-e*** and ***Fig. 4.12-f***). At low magnification both ribbons show a more uniform microstructure without strong gradient in microstructural features, but if in the ribbon containing 0.3wt% Er some Al cells are still distinguished (***Fig. 4.12-d***), in the alloy containing 0.1wt% nano-TiB_2 (***Fig. 4.12-f***) it is really hard to define shape and dimensions of the Al cells.

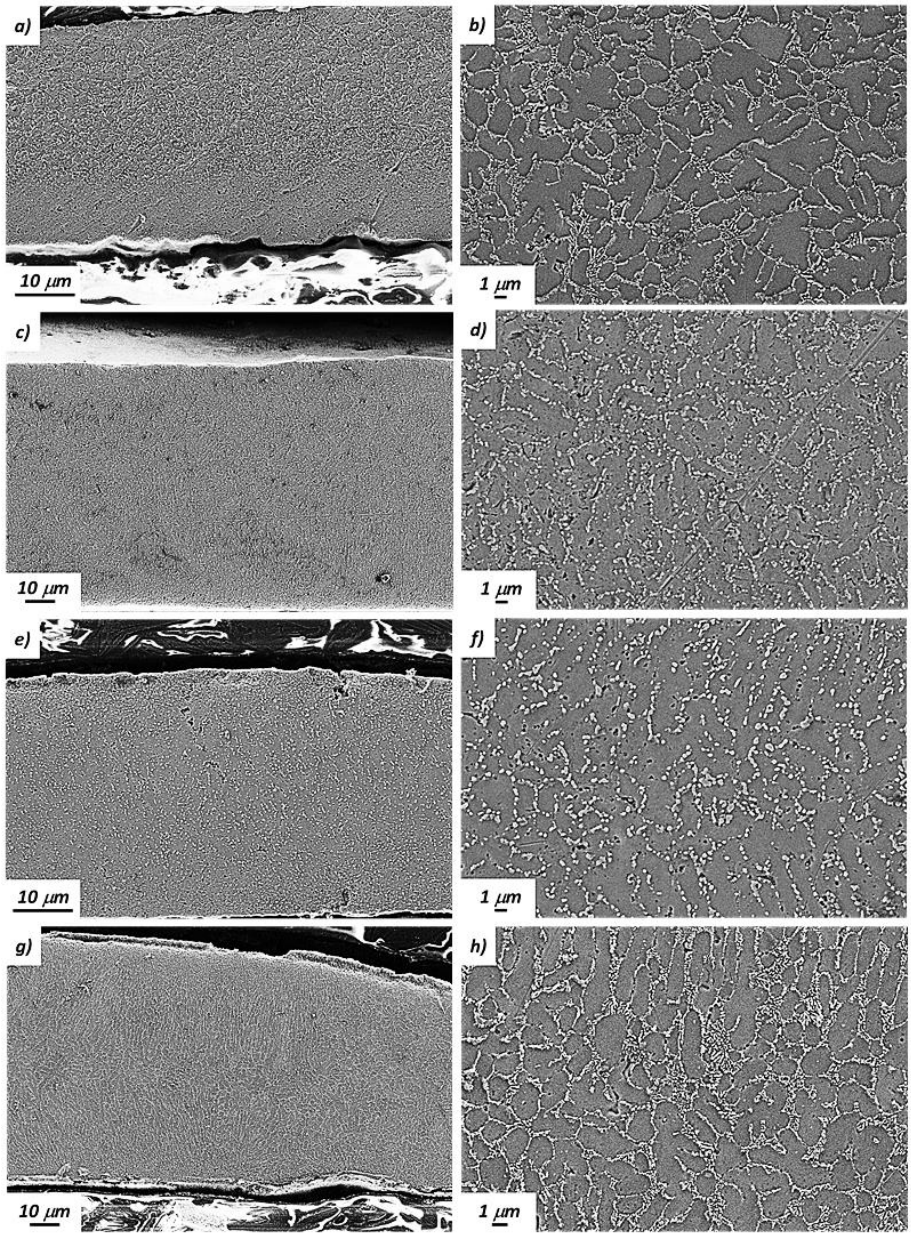

Fig. 4.12 *Micrographs of the melt spun ribbons unmodified and modified with the addition of inoculants. (a) and (b) represent the low and high magnification micrographs of the AlSi10Mg alloy; (c) and (d) those of the ribbon containing the 0.3wt% of Er; (e) and (f) the ones of the ribbon modified with 0.1wt% of nano-TiB_2; (g) and (h) the micrographs of the ribbon containing 0.1wt% of Sr. Low magnification images show the whole cross section of the ribbons while the high magnification images were collected in the centre of the ribbons.*

In order to evaluate the effectiveness of the different elements in modifying the eutectic Si, eutectic percentage, Al cells dimension and Si dimensions were measured, ***Table 4.7***.

Table 4.7 *Comparison of eutectic Si percentage, Al cells dimensions and Si dimensions observed in melt spun samples of both unmodified AlSi10Mg and alloy containing Er, nano-TiB_2 and Sr additions.*

Sample	***Eutectic Si percentage***	***Al cells dimensions [μm]***	***Si dimensions [nm]***
AlSi10Mg	*20 ± 2*	*3 ± 1*	*899 ± 119*
AlSi10Mg+Er	*13 ± 1*	*2.3 ± 0.1*	*255 ± 12*
AlSi10Mg+TiB_2	*12 ± 1*	*2.5 ± 0.3*	*310 ± 7*
AlSi10Mg+Sr	*18 ± 2*	*1.29 ± 0.06*	*144 ± 8*

From results in ***Table 4.7*** it is noted that all ribbons containing modifying elements display a lower eutectic Si percentage with respect to the unmodified alloy suggesting extended supersaturation of Si in the α-Al. However, it is important to underline that the reduced dimensions of Si precipitates, being under the resolution of the image analysis, can influence these results. Al cells dimensions appeared to be of the same order of magnitude of that observed for the AlSi10Mg ribbon produced with the same parameters, but Si eutectic was strongly modified upon addition of Er, nano-TiB_2 and Sr. As apparent from ***Fig. 4.12***, after the modification eutectic Si is fragmented, this results in reduced Si dimensions. Si dimensions, however, are only partially indicative of the modification of the microstructure; in fact, the ribbon containing nano-TiB_2 display the coarser Si but also the stronger modification of the microstructure ***Fig. 4.12-e*** and ***Fig. 4.12-f***.

XRD measurements were performed both to evaluate the phases present upon modification and to determine the level of Si solubilization through the application of the Vegard's law. In ***Fig. 4.13*** is reported the comparison of the XRD patterns acquired on the air side of all the ribbons under study. All samples displayed the same phases, i.e. fcc Al and diamond cubic Si, no other reflections were identified, as expected considering the low amount of modifying elements added into the AlSi10Mg alloy.

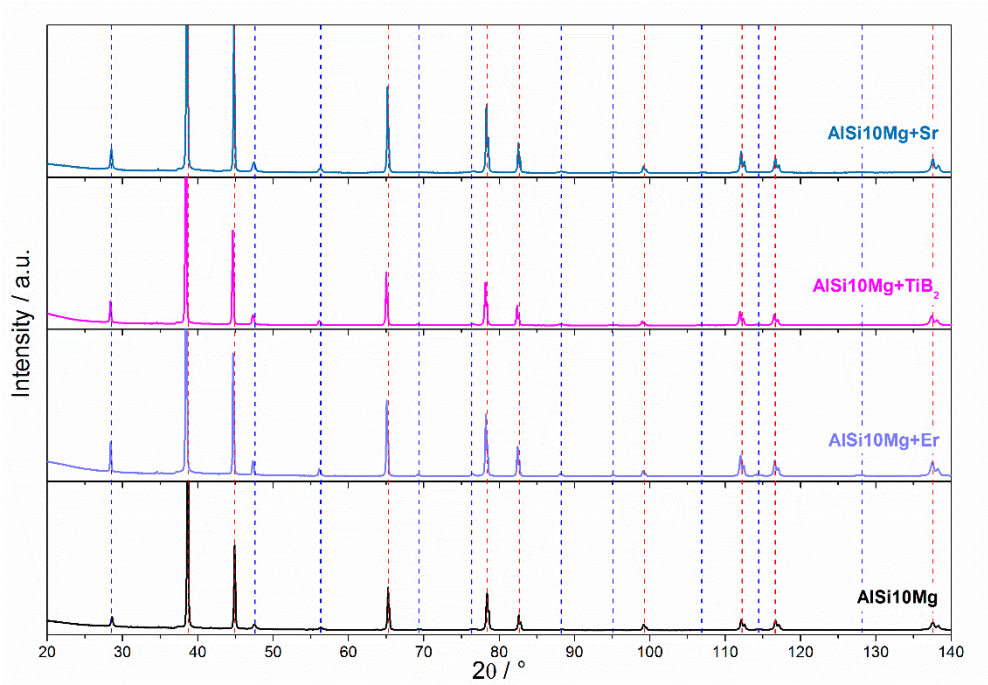

Fig. 4.13 *XRD patterns of the air side of both unmodified and modified ribbons. The dashed blue lines represent diamond cubic Si reflections while the dashed red lines represent fcc Al reflections.*

Reflections of fcc Al were employed to determine the lattice parameter of Al and to quantify the level of Si supersaturation using the Vegard's law. A comparison of the lattice parameter obtained for the ribbons under study is reported in ***Fig. 4.14***. All the lattice parameters appear to be below the value of the AlSi10Mg alloy solidified in equilibrium condition indicating Si supersaturation, moreover all ribbons display similar lattice parameters. No clear trend was observed when analysing the differences in lattice parameter when moving from the wheel side to the air side in accordance with the microstructural features observed in ***Fig. 4.12***. To evaluate the amount of Si supersaturation Vegard's law was applied to the average of the lattice parameters reported in ***Fig. 4.14***, the results obtained from the calculations are reported in ***Table 4.8***.

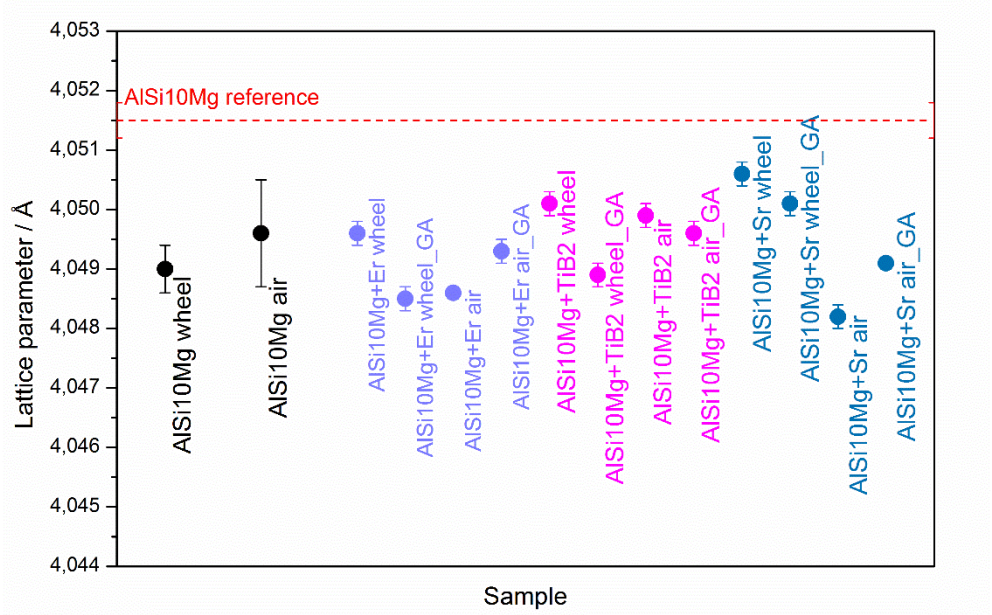

Fig. 4.14 *Comparison of the lattice parameter of Al calculated for the AlSi10Mg alloy and for the alloy modified with Er, nano-TiB_2 and Sr. Measurements were carried out on both wheel and air sides and for measurements performed both in Bragg-Brentano and in Grazing Angle (GA) configuration.*

As reported in ***Table 4.8***, the amount of Si supersaturation is more or less the same for all the samples and lays in between 1 at% and 1.5 at% in accordance with what already determined for the unmodified alloy.

Table 4.8 *Comparison of the amount of Si supersaturation present in the AlSi10Mg, AlSi10Mg+Er, AlSi10Mg+nano-TiB_2 and AlSi10Mg+Sr ribbons.*

	AlSi10Mg	***AlSi10Mg+Er***	***AlSi10Mg+TiB_2***	***AlSi10Mg+Sr***
Solubilized Si [at%]	*1.3 ± 0.4*	*1.5 ± 0.3*	*1.1 ± 0.1*	*1.2 ± 0.5*

A comparison of the curves obtained from DSC is reported in ***Fig. 4.15***.
All samples display two precipitation signals the first one being more intense and occurring at variable temperatures while the second one appears to be invariant in temperature.

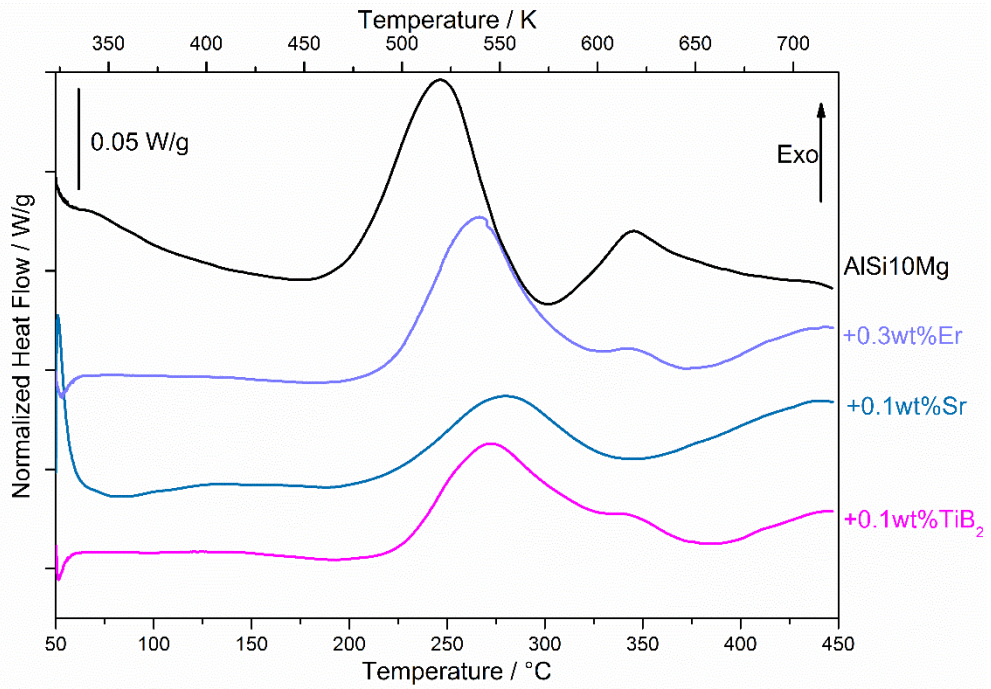

Fig. 4.15 *Comparison of the precipitation signals observed in the melt spun samples of AlSi10Mg and AlSi10Mg containing Er, nano-TiB_2 and Sr.*

These signals are the same already described for the AlSi10Mg alloy and are associated respectively to Si precipitation and to the precipitation of Mg and other impurities present in the AlSi10Mg alloy. The onset temperature and the precipitation enthalpy of the signal associated to Si are indicative of the amount of supersaturation in Si present in the samples, i.e. the higher is the temperature and the lower is the enthalpy and the lower will be the amount of Si retained in solution. From ***Fig. 4.15*** it is evident that in all samples modified with inoculants the Si precipitation signal occurs at slightly higher temperatures and has a lower enthalpy indicating reduced supersaturation with respect to what observed for the AlSi10Mg ribbon. From the DSC curves the ribbon containing Sr appears to be the one displaying the lowest supersaturation level (below 10 J/g). This is reflected in the wider error bar obtained when evaluating the amount of Si solubilized applying the Vegard's law, and can be explained considering that, as reported in literature [120,127,128], Sr act as nucleation initiator for Si, resulting in more frequent

precipitation of Si nuclei having smaller dimensions, consistently with what determined in ***Table 4.7*** from the image analysis, and consequently reducing the level of supersaturation.
This result agrees with what determined by XRD, but not all the ribbon is expected to possess the same level of supersaturation. In order to evaluate the exact enthalpy of precipitation and the consequent level of supersaturation for the ribbons containing inoculants further measurements are required.
To evaluate the effect of the different inoculants on the AlSi10Mg alloy melting and solidification of the alloys were studied through DSC, results on both onset and offset temperatures as well as enthalpies for melting and solidification signals are reported in ***Table 4.9***.

Table 4.9 *Onset and offset temperatures of melting and solidification temperatures along with the associated enthalpies for the unmodified AlSi10Mg alloy and for the alloys modified with 0.3wt% Er, 0.1wt% nano-TiB_2 and 0.1wt% Sr.*

	T_{onset} [°C] Heating	T_{offset} [°C] Heating	ΔH_{melt} [J/g]	T_{onset} [°C] Cooling	T_{offset} [°C] Cooling	ΔH_{sol} [J/g]
AlSi10Mg	571 ± 1	603 ± 1	458 ± 12	577 ± 6	552 ± 1	449 ± 1
AlSi10Mg+Er	568 ± 1	609 ± 3	449 ± 11	587 ± 1	550 ± 1	447 ± 2
AlSi10Mg+TiB_2	569 ± 1	602 ± 3	495 ± 7	584 ± 1	549 ± 1	483 ± 3
AlSi10Mg+Sr	573 ± 1	603 ± 1	463 ± 8	587 ± 1	551 ± 1	459 ± 1

Onset and offset temperatures for all the samples appear in agreement indicating that there are no differences in the melting point of the alloys, during solidification undercooling is observed but also in this case this acts in the same way for all the compositions under study.
A higher enthalpy of melting was observed in the unmodified sample and in the sample containing nano-TiB_2, the same result being observed also for the solidification enthalpy in the case of the AlSi10Mg+TiB_2 ribbon. Overall, results can be considered homogeneous for all the samples under study indicating that the presence of inoculants does not induce variations in melting and solidification mechanisms.
Further investigations were carried out to evaluate how the presence of inoculants affects the mechanical properties of the AlSi10Mg alloy. Results

on hardness derived from nano-indentation measurements performed on the cross section of the different ribbons are reported in ***Table 4.10***.

Table 4.10 *Comparison of the hardness values measured on the cross section of the unmodified and modified ribbons through nanoindentation.*

	AlSi10Mg	***AlSi10Mg+Er***	***AlSi10Mg+TiB_2***	***AlSi10Mg+Sr***
Hardness [GPa]	*1.8 ± 0.3*	*1.5 ± 0.3*	*1.1 ± 0.4*	*1.3 ± 0.5*

Hardness values for all ribbons modified with the addition of inoculants were found to be slightly lower with respect to that of the unmodified ribbon in the as spun condition. This is associated to the reduced amount of eutectic Si observed in the ribbons and to its disrupted morphology.

Despite hardness values do not show a significant improvement of the mechanical properties of the alloys modified with the addition of inoculants what is interesting is that also in rapid solidification conditions the presence of inoculants affects the morphology of eutectic Si. The refinement deriving from the combined effect of both grain refiners and rapid solidification could be of great interest especially if able to promote a more homogeneous distribution of Si nanocrystals in the Al matrix.

4.3. Conclusions

4.3.1. AlSi10Mg+hardeners

The focus of this part was to modify the composition of the AlSi10Mg alloy, widely employed in AM, to obtain better mechanical properties. The elements selected for the strengthening are Ag and Cu, known to provide respectively solution and precipitation hardening in conventional Al alloys.
Since L-PBF processes are known to require several kilos of atomized powders for a single job, it is not convenient to test new composition directly with AM techniques. To avoid this problem, here a new route to test new compositions avoiding to employ of kilos of powder was proposed. The method, developed in partnership with the Politecnico di Torino (DISAT) and the Istituto Italiano di Tecnologia (IIT), consists in evaluating the properties of new compositions through two alternative processing routes, MS and SST. Through MS microstructural, structural and thermal properties of the alloy solidified under rapid solidification were investigated, while SSTs were employed to assess the process window suitable for the selected compositions. In the end the process was validated producing a bulk sample by L-PBF with the most promising composition using the process parameters optimized with SSTs.
The microstructural features for both AlSi10Mg+Ag and AlSi10Mg+Cu are compatible meaning that the two alloys processed both by MS and SST give the same microstructural features even if solidification conditions are not equal due to the differences in heat subtraction. The bulk sample produced with the most promising alloy, the AlSi10Mg+Cu provided the same features observed in the other test samples, giving a first validation of the method proposed for designing new alloys.
Structural and thermal properties were evaluated only for MS samples. Results obtained from XRD patterns and lattice parameter calculation indicate the presence of extended solid solubility of both Si and hardeners respectively Ag in AlSi10Mg+Ag and Cu in AlSi10Mg+Cu. These results agree with what observed in rapidly solidified AlSi10Mg, where it was evidenced that increasing the cooling rate of the process, and so the level of

supersaturation achievable, there is a decrement in the value of the lattice parameter due to the increased solubilization of Si (and for the modified alloy of Cu) in the α-Al.

From calorimetric measurements results similar to those obtained for AlSi10Mg in chapter 3 were observed. No peculiar signals were identified after the additions of Ag and Cu; but, for the sample containing Cu, an increase in the precipitation enthalpy of the signal associated to Si was evidenced. This is probably related to the double contribution of Si and Al-Cu compounds precipitation occurring in the same temperature range.

To evaluate the mechanical properties of the alloys, nano-indentation tests were performed on all samples (MS and SSTs). Results obtained agree meaning that the two processing routes provide similar mechanical properties.

Due to the encouraging results obtained for the alloy containing Cu, the next step was to verify if results obtained by MS and SST were reproduced when producing a bulk platelet. SSTs were used to define the process window for the selected composition, while MS was employed as benchmark of microstructure and alloy properties after rapid solidification processing.

In all three cases an AlSi10Mg+Cu alloy was obtained showing that compositional homogenization is feasible even when starting the production from a powder mixture. Only some residual inhomogeneity in Cu distribution was found in the SST sample.

The microstructural features, i.e. cell size of primary Al and eutectic morphology of Si, obtained for SST and MS differ notably but help in interpreting the solidification process in the different techniques. The microstructure is almost one order of magnitude finer in SST and eutectic is made of highly distorted fibres. This implies that the rate of heat transfer to the quenching substrate and the convective motion of the melt differ substantially.

Schematically, the microstructures indicate that the melt in SST is turbulent, whereas it is quiescent in melt spinning. This affects the rate of nucleation and growth of phases. The microstructure morphology of the bulk sample produced by L-PBF is similar to that of MS ribbon, but intermediate between

SST and MS in terms of cell size. In all cases the Cu forms to a large extent the Al_2Cu phase directly from the melt which is intermixed with the eutectic.

The combination of results on lattice parameter of the primary phase, temperature and enthalpy of exothermal DSC signals due to precipitation indicate the occurrence of supersaturation of both Si and Cu in the as quenched samples. The Cu supersaturation was estimated in between 0.75 at% and 1 at% in both L-PBF and MS samples. Precipitation of both Si and Al-Cu compounds occurs on continuous heating at temperatures just above 200°C.

The mechanical properties were evaluated by means of nano-indentation and Vickers tests. The results given by the samples made with all processing techniques agree in showing an increase in hardness of the as prepared samples with respect to that of the base AlSi10Mg alloy, mostly due to the occurrence of Cu compounds intermixed with the eutectic. Nanoindentation maps show some scatter in hardness data due to local inhomogeneity in Cu distribution in the SST sample.

Since the combination of the fast MS and SSTs technique, which employ limited amount of powder, was proved effective in simulating the synthesis of new compositions and their properties, it is concluded that the approach used here will allow to test rapidly alloys and to expand the material palette available for AM processes.

4.3.2. AlSi10Mg+inoculants

After demonstrating that it is possible to evaluate the characteristics of alloy processed by L-PBF using MS and SSTs, the influence of different grain refiners, i.e. Er, nano-TiB_2 and Sr, on the AlSi10Mg alloy after rapid solidification was investigated.

Since it is not convenient to test new composition directly with AM techniques, MS was used as a fast technique to get a complete screening of the properties of new compositions before moving towards more complex approaches.

After the addition of inoculants (Er, nano-TiB_2 and Sr) to the AlSi10Mg alloy, the microstructure of the ribbons appears composed of two main phases, i.e. α-Al and Si eutectic as in the unmodified alloy; but here it is no more possible to describe the Si as a continuous network embedding the primary phase because it results disrupted forming smaller Si crystals dispersed in the matrix.

The amount of Si observed in the micrographs suggest the presence of supersaturation, as confirmed by calculating the lattice parameter of Al through XRD. Results obtained from XRD patterns and lattice parameter calculations agree with what already observed in AlSi10Mg samples produced by means of different rapid solidification techniques, where it was evidenced a decrement in the value of the lattice parameter due to the increased solubilization of Si. Supersaturation was found to be in the range 1 at% to 1.5 at%.

From calorimetric measurements results close to those obtained for AlSi10Mg were observed. No peculiar signals were identified after the additions of Er, nano-TiB_2 and Sr, but for all samples a decrease in the precipitation enthalpy of the signal associated to Si was observed. These results were found to agree with the increased nucleation frequency of Si in presence of inoculants. Moreover, also melting and solidification of these alloys were investigated. For all alloys onset and offset temperatures were found to agree indicating that the presence of grain refiners does not induce alterations in the mechanisms of melting and solidification. During solidification undercooling was observed.

To evaluate the mechanical properties of the alloys, nano-indentation tests were performed on the cross sections of all samples. The average hardness values obtained were found to be slightly lower than that of the unmodified alloy for all the inoculant additions indicating the continuous Si network as main responsible for the increase in hardness observed in rapidly solidified samples.

The fact that eutectic Si appears to be more disrupted, in principle can lead to a more homogeneous Si distribution inside bulk samples produced by means of AM, making mechanical properties more isotropic. To verify this aspect of course further measurements will be required, following the same pathway already described for the AlSi10Mg+Cu alloy in 4.2.1. Hopefully, in the next months, SSTs and bulk specimen will be produced by AM and fully characterized to confirm what observed through MS.

5. Part III: Residual stresses in AlSi10Mg alloy by Laser-Powder Bed Fusion

5.1. Experimental procedure

5.1.1. Sample selection

Measurements for the evaluation of residual stresses were performed on several AlSi10Mg samples both with XRD and Raman spectroscopy.
XRD measurements were conducted to evaluate if differences in scanning strategy and temperature of the building platform were able to provide substantial changes in the stress state of the system.
Analysis with Raman spectroscopy were conducted to get a deeper insight on the relationship Raman shift - residual stress - Si dimension.
In order to investigate this, different samples were selected for the different characterization techniques.
Samples selected for XRD measurements are cubic samples of AlSi10Mg produced by L-PBF having dimensions $15\,x15\,x10\,mm$ after support removal. All samples were produced using the same laser power, scan speed and hatching distance already described in ***Table 3.2***. These parameters were kept fixed since they allow to obtain dense samples. What was changed were the scanning strategy (rotating each layer of 67° or scanning unidirectionally along *X* for the whole job) and the temperature of the building platform (35°C or 100°C). Moreover, one sample was produced directly on the building platform without the presence of support structures and analysed to understand if supports can provide beneficial effects on the presence of residual stresses.
The selected samples were analysed both in the AB conditions and after the SR treatment (2h@300°C) on five of the six faces of the cubes. The bottom face of the cubes was not considered because of its higher roughness consequence of supports removal.
A list of the samples analysed along with their production parameters is reported in ***Table 5.1***.

Table 5.1 *L-PBF AlSi10Mg samples selected for the residual stress measurements and their process parameters.*

Sample name	***Scanning strategy***	***Temperature of the building platform [°C]***
AM_AB_67°_35°C	*67°*	*35*
AM_AB_67°_100°C	*67°*	*100*
AM_AB_X_35°C	*X*	*35*
AM_AB_X_100°C	*X*	*100*
AM_AB_67°_100°C_EDM	*67°*	*100*
AM_SR_67°_100°C	*67°*	*100*
AM_SR_X_35°C	*X*	*35*
AM_SR_X_100°C	*X*	*100*
AM_SR_67°_100°C_EDM	*67°*	*35*

Faces to be analysed were identified by defining a standard nomenclature for each face and this label was added as a suffix after the sample name defined in ***Table 5.1***. The nomenclature chosen follows the scheme depicted in ***Fig. 5.1***.

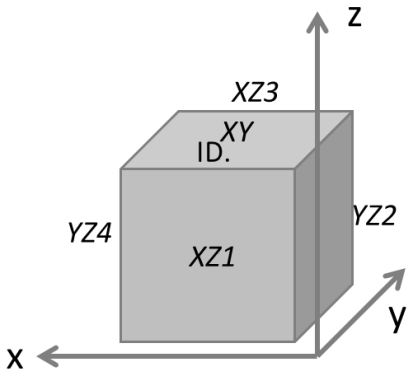

Fig. 5.1 *Scheme of the cube with the label associated to each face. ID. stands for a 3D printed label on top of each cube describing the process parameters employed for sample production.*

Of course the cubic samples for residual stress determination were analysed at first in their raw form (without any cutting or surface treatment), then after all the analysis were completed other measurements were performed on the *XZ1* face of the AM_AB_67°_35°C after mechanical polishing down to

40 nm and after electropolishing (following the procedure reported in 5.1.2.2).

Residual stress determination by Raman spectroscopy was conducted at first on the samples produced by CMC, MS and L-PBF employed in chapter 3. This first set of measurements was performed to see if Raman was able to see differences in samples produced with different cooling rates and so showing different eutectic morphologies. Another set of measurements was then conducted on the same samples employed for the determination of residual stresses through XRD in order to evaluate if it is possible to find a correlation between the macro-stress determined by XRD on Al and the micro-stress obtained by Raman spectroscopy on Si.

Raman spectra were acquired on at least three random positions on the sample surface, for the AB samples obtained with different parameters the nomenclature described in ***Table 5.1*** and ***Fig. 5.1*** was kept.

5.1.2. Sample preparation

5.1.2.1. Preparation for Raman measurements

Micro-Raman spectroscopy requires the part of sample onto which the analysis is performed to be in focus. Taking in mind this point, AlSi10Mg samples were investigated by Raman spectroscopy in raw form when possible. In the case it was not possible to find a portion of the sample onto which perform the analysis, the sample was cut and mechanically polished. Samples were analysed on different points along the sample surface and in case of MS ribbons measurements were performed both on wheel side and air side of the specimen. As for XRD stress measurements, L-PBF cubes were analysed on the five faces described in ***Fig. 5.1***.

5.1.2.2. Preparation for XRD measurements and Electropolishing

L-PBF samples for XRD residual stress measurements were analysed at first in their raw form in order not to alter the stress state of the samples. Then, to see how stress changes moving deeper in the sample, tests were performed on samples polished down to 3 μm and electropolished.
Electropolishing tests were performed following the ASTM E1558-09 (2014) using a home-made system as that reported in ***Fig. 5.2*** in which the cathode was a plate of stainless steel.

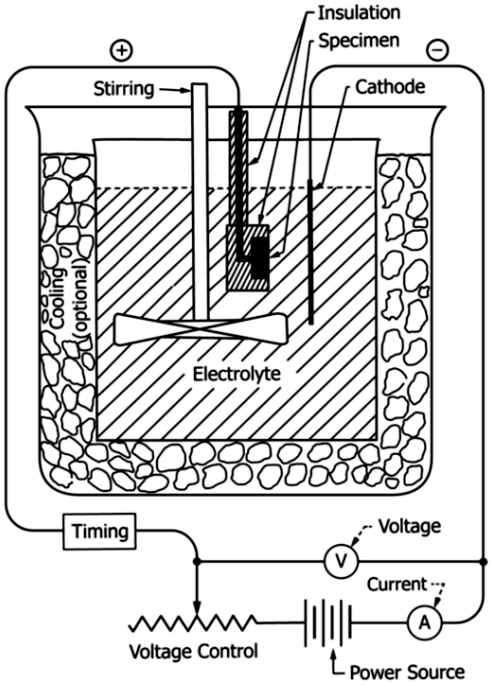

Fig. 5.2 *Scheme of a simple system for electropolishing tests (ASTM 1558-9 (2014))*

After several attempts performed varying temperature of the electrolyte, electrolyte composition, applied voltage and time of the process the best treatment conditions were identified.
As electrolyte a volumetric solution containing 90% Ethanol and 10% Perchloric acid (having concentration of 30%) was employed. Electropolishing was performed at room temperature applying approximately 10 V for 30 s. To avoid the formation of a passive layer of

oxide, that hinders the electrolyte to act homogeneously on the sample surface, mechanical polishing down to 3 μm was performed just before the electropolishing treatment. In presence of the passive layer time of treatment was increased.

In this specific case electropolishing was performed just to remove homogeneously a layer of material without introducing external stresses on the sample under analysis. The conditions reported here for electropolishing do not allow to obtain a mirror like surface for samples produced by L-PBF, probably because of the fine Si structures dispersed in the matrix; nevertheless, they were suited to remove the layer deformed by mechanical polishing.

5.2. Results

5.2.1. Raman spectroscopy

The first set of measurements by Raman spectroscopy was performed on the AlSi10Mg samples produced by means of different rapid solidification techniques already described in chapter 3**.**

In ***Fig. 5.3*** is reported the comparison of the transverse optic mode of crystalline Si produced by CMC, MS and L-PBF before and after stress relieving, along with a reference spectra representing polycrystalline Si in absence of stress and nano-crystals.

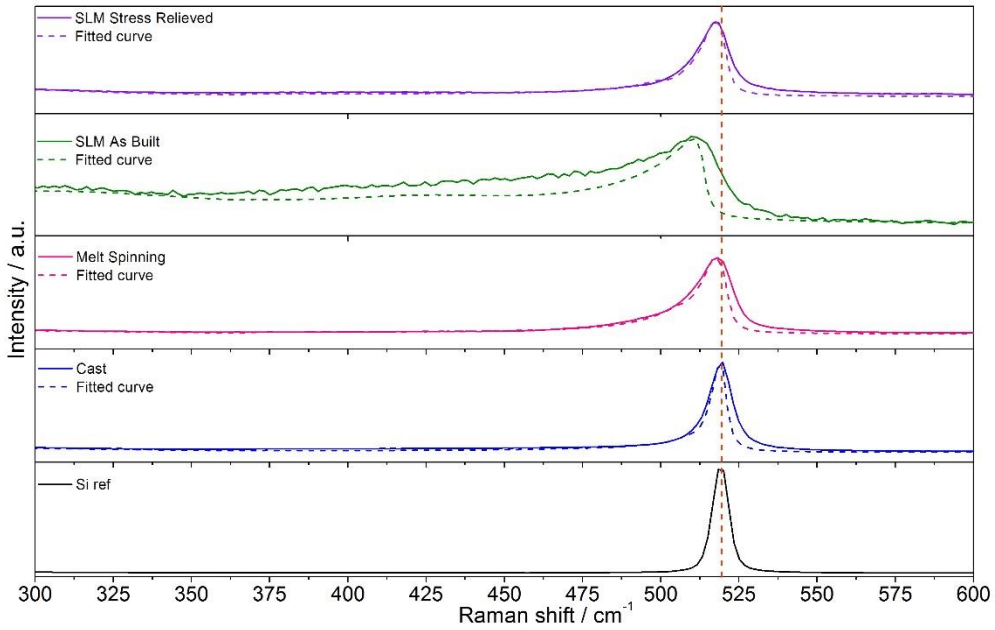

Fig. 5.3 *Comparison of the Raman spectra acquired on AlSi10Mg samples produced by means of different rapid solidification techniques (full line), along with the fit of the signal obtained after the analysis with the modified Campbell and Faucet model (dashed line). Moving from the bottom to the top of the image are reported the spectra acquired on: polycrystalline Si and AlSi10Mg produced by CMC, MS and L-PBF before (AM_AB) and after (AM_SR) stress relieving treatment. The red dashed line represents the position of the Si transverse optic mode in absence of stress and nanocrystals.*

Increasing the cooling rate, so going from the bottom to the top of ***Fig. 5.3***, Raman signal appears to be shifted towards lower wavenumber and broadened. After the stress relieving treatment performed on the sample produced by L-PBF, the Raman peak appears to be blue-shifted back towards the position of the reference and narrowed with respect to the sample in AB conditions.

The shift observed in ***Fig. 5.3*** is indicative of Si modification in the AlSi10Mg alloy when subjected to rapid solidification. However, considering that the Raman signal is more affected by nano-crystals than by micro-crystals, it is not straightforward to determine if the Raman shift observed is associated to the presence of residual stress in the samples or if the presence of nanometric Si crystals is predominant in the shift.

The same measurements were performed also on the L-PBF samples produced varying the scanning strategy and the temperature of the building platform, both in AB and SR conditions, in order to evaluate if different process parameters have a strong effect on the TO mode of Si.

In these samples limited variability on the position of the peak and on the dimensions of Si crystals, reported for clarity in ***Fig. 5.4***, was evidenced through the modified Campbell and Fauchet model, indicating that different process parameters have a limited influence on Si dimension and possibly on the stress level of samples. Even if the differences reported in ***Fig. 5.4*** are limited, it is interesting to underline how the model is able to discriminate in between samples before and after the stress relieving treatment. In fact, it is evident how samples in AB condition give average Si dimension below 7 nm as a first approximation, while samples that have received the SR treatment give average Si dimension above 7 nm.

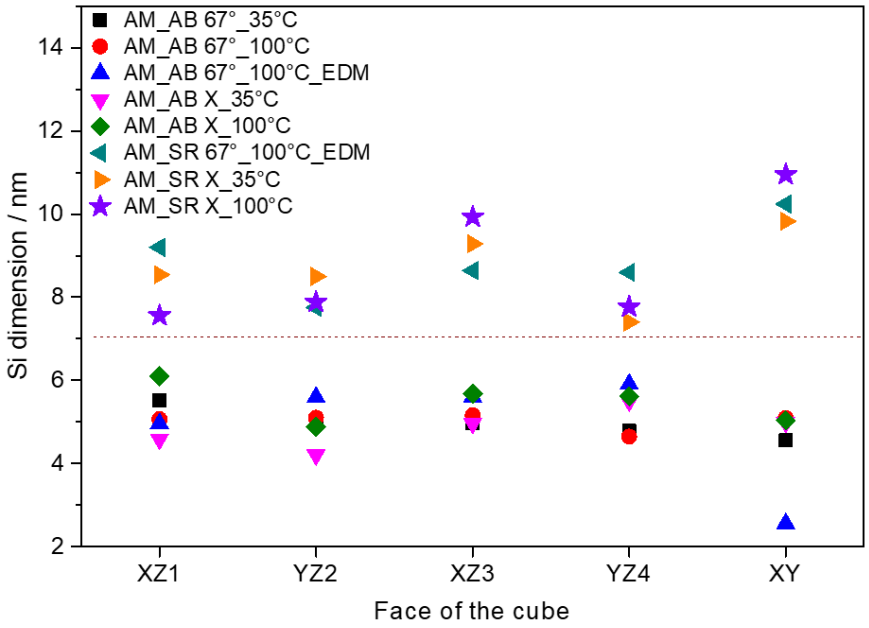

Fig. 5.4 *Comparison of Si nano-crystals dimensions obtained through the Campbell and Fauchet model applied on Raman spectra acquired on different faces of samples produced by L-PBF with different process parameters, both before (AM_AB) and after stress relieving treatment (AM_SR). The dashed line represents an ideal distinction in between samples before and after SR.*

To understand the reasons behind the shift observed, a careful literature search was performed and in this way an experimentally determined correlation between size of Si nano-crystals and shift was found, [160]. Having in mind this relationship, it was possible to compare the dimension of Si nano-crystals obtained through the calculation in Mathcad of both the samples produced by means of different rapid solidification techniques and the L-PBF samples produced with different process parameters with the theoretical behaviour reported in literature, ***Fig. 5.5***.

As reported in ***Fig. 5.5***, the dimensions and peak positions obtained from Mathcad follow the general trend described by Ossadnik et al. in [160] but the curve is shifted to lower wavenumbers of approximately 2 cm^{-1}. Samples produced by CMC (blue), MS with wheel velocity at both 10 m/s and 15 m/s (pink) and L-PBF after stress relieving treatment (violet) have the larger Si

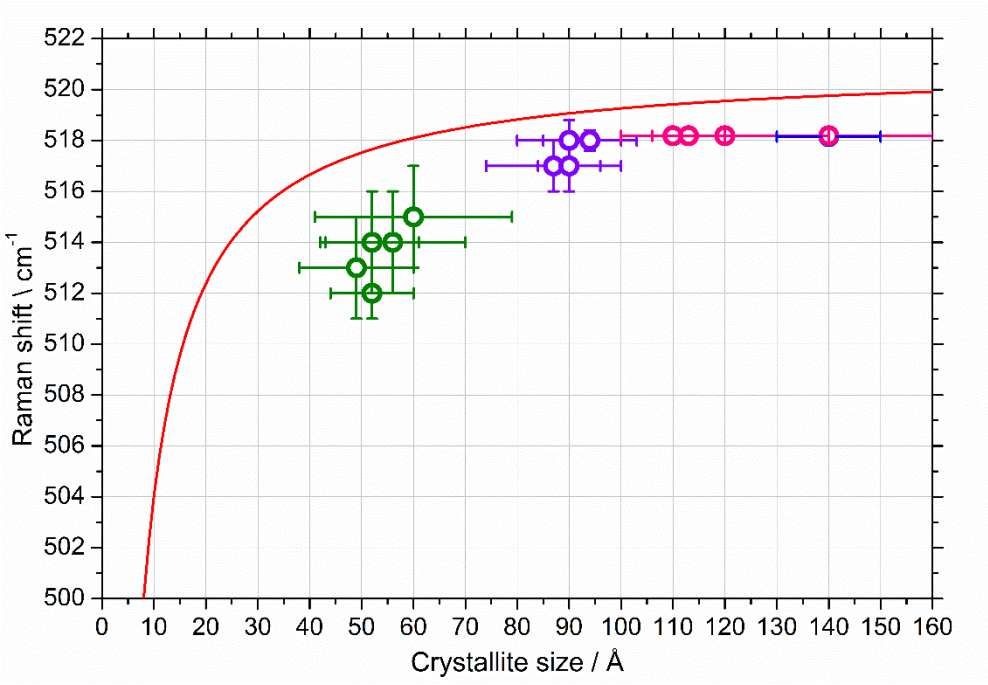

Fig. 5.5 *Comparison of the Si dimensions obtained from the Campbell and Fauchet model on samples produced by CMC (blue), MS (pink) and L-PBF both before (green) and after (violet) the stress relieving treatment. In samples produced by L-PBF the error bars represent simply the average of the results obtained on the different faces of the cubes analysed. The full red line represents the experimentally determined relationship described by Ossadnik et al. in [160].*

nano-crystals and the lower Raman shift, while samples produced by L-PBF in the as built conditions (green) result in smaller crystals and display a higher red-shift.

The displacement from the theoretical curve of the points obtained from the samples is interesting because could be an indication of the presence of a tensile stress contributing to the shift in the Raman signal.

To confirm these results of course it is necessary to validate the dimensions of Si nano-crystals present in the α-Al matrix as precipitates.

To get a better insight on Si morphology in samples produced by L-PBF, a small portion of the alloy was put into a diluted solution of HCl to selectively dissolve all the Al present in the alloy leaving only the unetched Si. Dissolution took place at approximately 70°C for several days. Once the

dissolution was complete, the acid solution was washed for several days into dialysis membranes in order to be able to retain the nanometric Si present as precipitate inside the matrix. Samples so obtained, along with bulk samples, were analysed both at FESEM and TEM to understand better Si dimensions in the L-PBF samples, ***Fig. 5.6***.

From ***Fig. 5.6-a*** it is evident that the fibrous Si eutectic forms a shell around the Al matrix, moreover the eutectic seems to be composed by small Si particles (i.e. having dimensions below 50 nm) aggregated together. This morphology is different from what observed in conventional micrographs, e.g. ***Fig. 5.6-b***, in which the Al matrix (lighter grey) is surrounded by continuous fibrous eutectic (darker grey). Increasing the magnification and focusing on some distinctive features of the eutectic, it is possible to confirm that these microstructural features are characteristic of different samples produced by L-PBF, ***Fig. 5.6-c*** and ***Fig. 5.6-d***. Further increasing magnification, it was possible to investigate the presence of nano-crystalline Si. In FESEM images Si particles having dimensions around 20 nm were evidenced, ***Fig. 5.6-e***; these are not small enough to contribute to the Raman shift described earlier, however it is important to underline that these dimensions are close to the instrumental limit. For this reason, further TEM analyses were performed both inside the Al matrix and on the Si extracted from the Al matrix. In the Al matrix, ***Fig. 5.6-f***, it was possible to isolate a particle having diameter of approximately 5 nm that was identified as Si along the (110) direction thanks to the interplanar distance. The dimension found in ***Fig. 5.6-f*** corresponds well to what found analysing the Raman spectra.

A further proof of the presence of nanometric Si was obtained analysing the finest part of the Si extracted from the α-Al matrix with TEM. In ***Fig. 5.7*** are reported two micrographs displaying the Si nano-crystals dispersed on the sample holder (***Fig. 5.7-a*** and ***Fig. 5.7-b***). To verify that particles observed are made of Si, EDX analysis and calculation of the interplanar spacing from the lattice fringes observed at high resolution (***Fig. 5.7-c***) were performed.

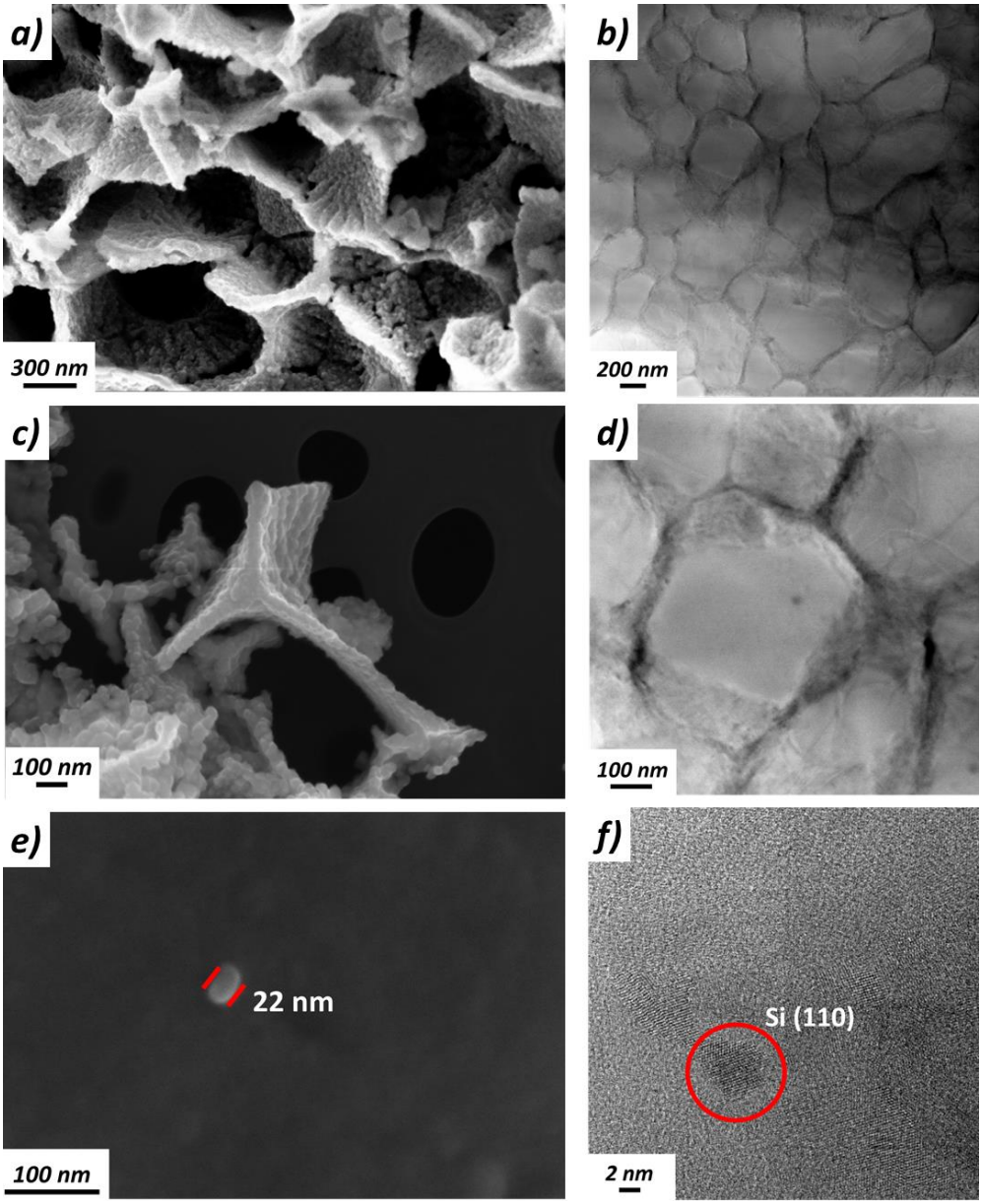

Fig. 5.6 *FESEM images of the Si extracted from L-PBF samples (left) and TEM images of an L-PBF sample (right). In detail: (a) and (b) are low magnification images in which is represented the shape of eutectic Si; (c) and (d) show a peculiar detail of the eutectic Si; while (e) and (f) represent Si precipitates that were found during the analysis.*

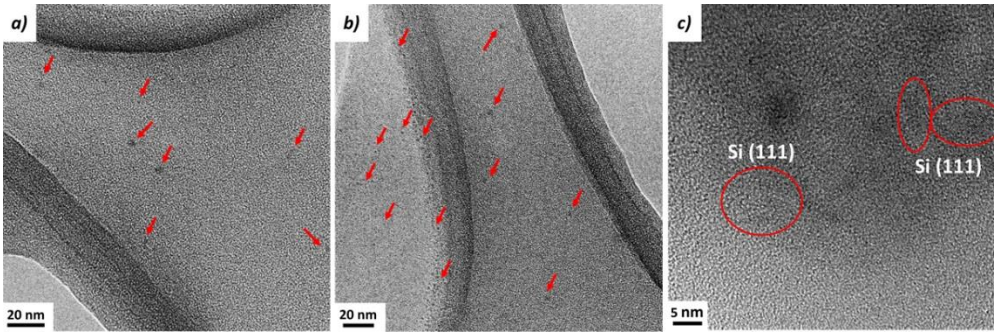

Fig. 5.7 *TEM micrographs representing the nanometric Si crystals removed from the α-Al matrix (a) and (b), along with a high resolution micrograph in which it is possible to identify the lattice fringes of (111) Si crystals, (c).*

Both the analysis confirmed that crystals observed are made of Si, so further measurements were carried out to determine which is the dimensional distribution of Si nano-crystals in the L-PBF samples in order to compare it with the distribution determined through Mathcad applying the modified Campbell and Fauchet model, ***Fig. 5.8***.

The distribution determined through the analysis of TEM micrographs, ***Fig. 5.8-a***, agrees well with that determined with Mathcad, ***Fig. 5.8-b***.

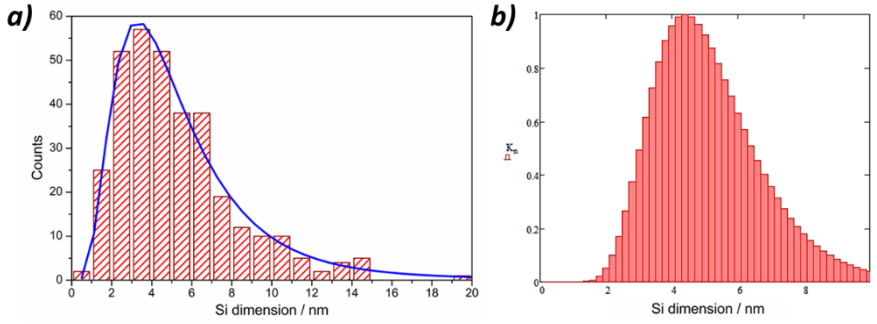

Fig. 5.8 *Comparison of the distribution of Si dimensions determined both by TEM micrographs (a) and applying the modified Campbell and Fauchet model (b).*

The presence of nanometric Si crystals confirms the results obtained from the elaboration of the Raman spectra using the Campbell and Fauchet approach. For this reason, it is possible to state that, assuming the experimentally determined model presented by Ossadnik in [160] to be correct and Si dimension to be verified, apart from the shift related to

nano-crystals, there is also a shift caused by the presence of a tensile stress in the alloy for all the samples subjected to rapid solidification.
Up to now results on the presence of residual stresses are just qualitative.
As a first approximation, to obtain a quantitative result on the local residual micro-stress in Si for the different rapidly solidified samples measured through Raman spectroscopy, it is possible to employ the following relationship

$$\sigma = \Delta\omega \cdot 250MPa$$

presented in [147] and applied in presence of a biaxial stress.
The local micro-stress of Si for the different rapidly solidified sample was evaluated by subtracting the contribution of shift related to the presence of Si nano-crystals. The average results obtained for all samples along with their standard deviation are reported in ***Table 5.2*** along with the strain determined using the Young modulus of Si (140 GPa).

Table 5.2 *Quantification of local micro-stress and strain of Si through Raman spectroscopy.*

	CMC	***MS***	***AM_AB***	***AM_SR***
$\boldsymbol{\sigma_{Si}}$ *[MPa]*	*402 ± 25*	*341 ± 38*	*1038 ± 243*	*392 ± 134*
$\boldsymbol{\varepsilon_{Si}}$	*0.0029 ± 0.0002*	*0.0024 ± 0.0003*	*0.007 ± 0.002*	*0.003 ± 0.001*

5.2.2. X-Ray Diffraction

In parallel to Raman measurements, residual stresses were also determined conventionally by XRD. The first measurements performed were devoted to verifying the alignment of the diffractometer and ensure the reproducibility of the process. In particular, a set of measurements was performed on an IN718 provided us by GE-Avio along with the values of stress measured on this sample by several laboratories during a Round Robin. In ***Fig. 5.9*** are reported the stresses measured on this specimen along with those obtained by the other laboratories.

Results reported in ***Fig. 5.9*** agree well with those obtained during the Round Robin performed on the same specimen, meaning that the instrument is aligned and measurements were performed correctly.

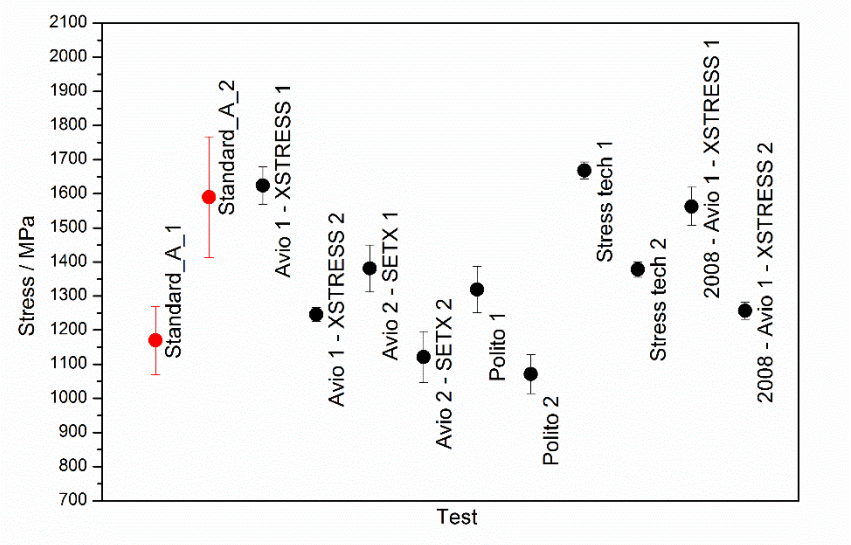

Fig. 5.9 *Residual stresses measured on the IN718 specimen in this work (red) and by other laboratories during a Round Robin (black). The suffix 1 and 2 represent the directions along which the measurements were performed.*

Prior to start the residual stress measurements on AlSi10Mg samples, the penetration of the X-ray beam in the AlSi10Mg alloy was evaluated for every tilting angle employed, to determine which is the average information depth from which residual stress is evaluated. This is defined as the depth from which 67% of the diffracted intensity has been absorbed and correspond to

the depth at which the stress is measured if the stress gradient along the depth is linear. The result obtained following the standard procedure reported in the UNI EN 15305:2008 regulation is reported in ***Fig. 5.10*** and show how the average information depth (x) varies with the tilting angle Ψ.
From ***Fig. 5.10***, it is evident that the information on residual stress in AlSi10Mg samples comes from a region comprised in between 20 and 40 μm below the surface. This factor is important when planning to perform an in-depth evaluation of the residual stresses in order to remove all the layers of material already analysed.

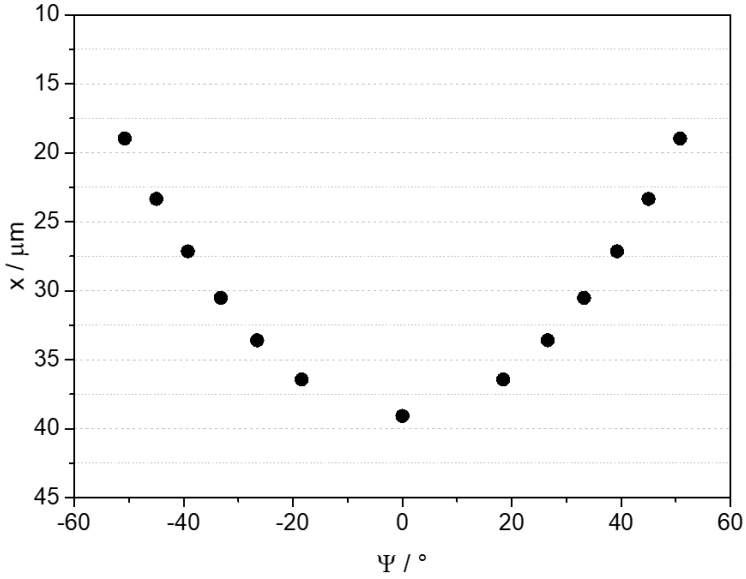

Fig. 5.10 *Average information depth as a function of the tilting angle for an AlSi10Mg alloy.*

The first set of measurements was performed on the raw, and consequently rough, surface of the L-PBF samples. Measurements were performed at the centre of each face of the cube both perpendicularly (*XY*) and parallel (*Z*) to the building direction. When analysing the top surface, it was impossible to apply this distinction, nevertheless measurements were carried out on two perpendicular directions, denoted for simplicity 1 and 2.
Patterns obtained at each Ψ angle were fitted with the X'Pert Highscore software and the variation of the interplanar distance with respect to $sin^2\Psi$

was employed to determine the stress value, as described in section 2.3.4. An example of the result of the calculation is reported in ***Fig. 5.11***.

As expected, from ***Fig. 5.11-b*** and ***Fig. 5.11-d*** it is evident that the stress value is substantially lowered after thermal treatment. This change in stress state of the sample is already clear from the position of the peaks at different tilting angle Ψ. In fact, if in ***Fig. 5.11-a*** the reflections appear to be strongly shifted; in ***Fig. 5.11-c***, where the stress state is close to 0, they appear simply one of top of the other at the same Bragg angle.

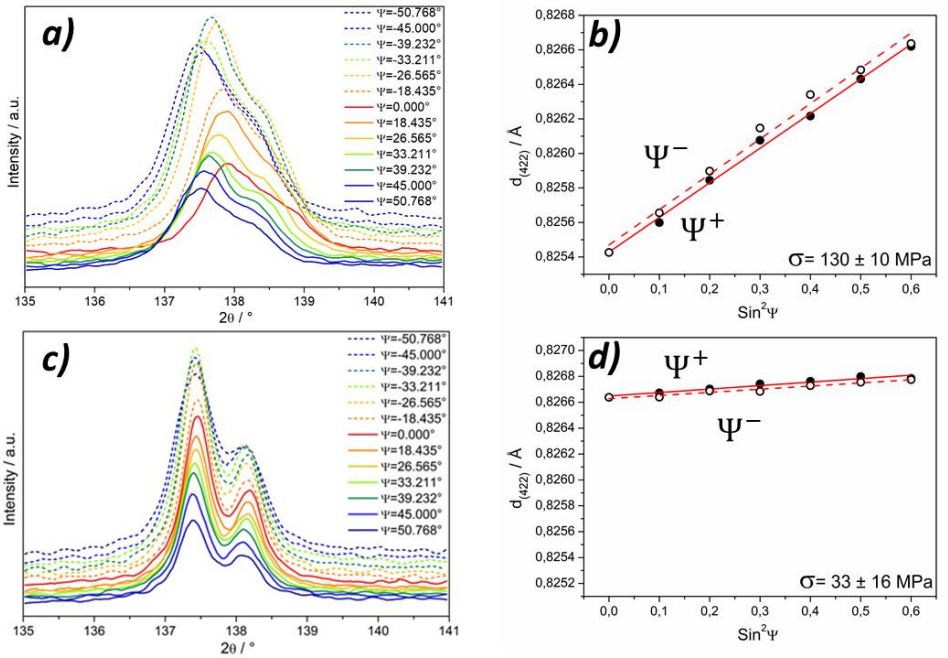

Fig. 5.11 *Examples of patterns and d vs. sin²Ψ graphs used for residual stress evaluation on the XZ3 face of AM_AB_67°_100°C_EDM both before (a and b) and after (c and d) stress relieving. In particular (a) and (b) refer to the sample in AB condition analysed with the X-Ray impinging perpendicularly to the building direction (XY direction), while (c) and (d) refer to the same face of the SR sample analysed parallel to the building direction (Z direction).*

These measurements were performed for the raw surfaces of all samples selected in ***Table 5.1*** in both the *Z/1* and *XY/2* directions.

Results obtained for the samples in AB condition are reported in ***Fig. 5.12***.

From ***Fig. 5.12*** it is possible to observe a clear distinction in stress between samples analysed along the *XY* (higher stress) and *Z* (lower stress) directions on the lateral faces of the cubes, all stresses measured being tensile. This strong distinction in stress is explained considering that, during the L-PBF process, there is a strong directionality of heat subtraction along the building direction (*Z*) and so it is reasonable that stress development occurs with a preferential orientation in the cubes. It is interesting to notice that in the *XY* face of the L-PBF samples the stress remains constant even when changing the direction of analysis (*1* or *2*).

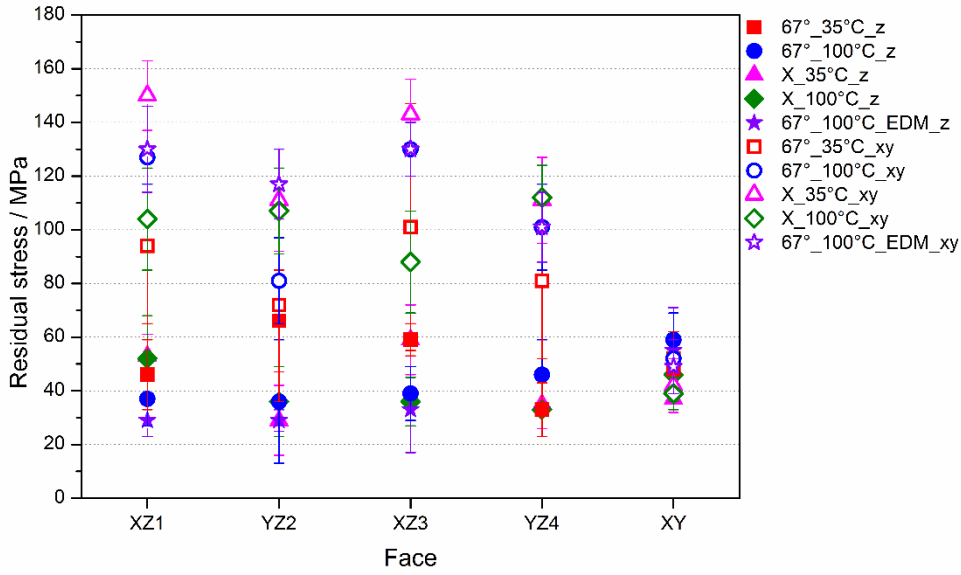

Fig. 5.12 *Comparison of the stress values obtained both perpendicularly (XY/2) and parallel (Z/1) to the building direction for each face of the L-PBF samples in the AB conditions.*

This result is explained considering the directionality of heat subtraction. In fact, from literature [19], it is well known that the AlSi10Mg alloy processed by means of L-PBF consists of grains of Al having different morphologies according to the surface under analysis, i.e. columnar Al grains along the building direction and more equiaxic grains perpendicularly to that, as confirmed by the EBSD measurements reported in ***Fig. 5.13***. Considering the inhomogeneous distribution of grain boundaries along *Z* and *XY* when looking

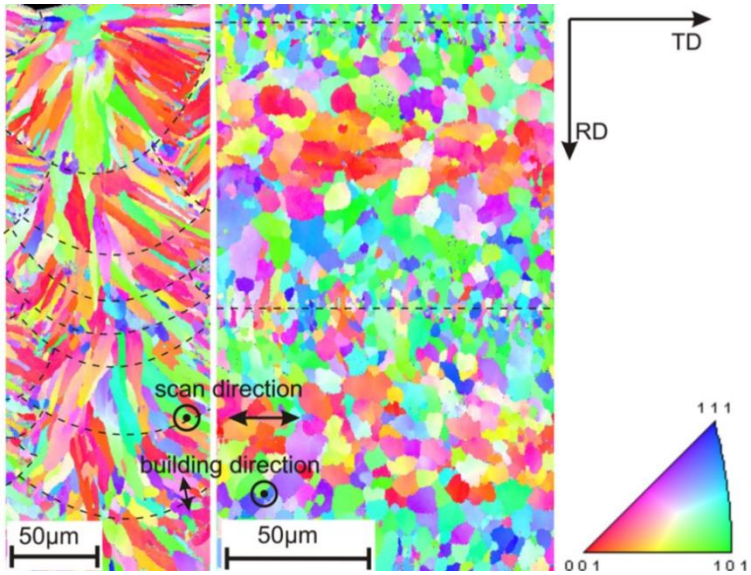

Fig. 5.13 *EBSD maps of an AlSi10Mg cubic sample produced by L-PBF and characterized in [19]. The EBSD map on the left represent the Al grain structure along the building direction (Z), while the EBSD map on the right represent the Al grain structure perpendicularly to the building direction (XY face of the cube). Z and XY being the notations used in this thesis.*

at the lateral faces of the cubes, it is easy to associate the lower stress level obtained along the *Z* direction to the lower amount of Al grain boundaries encountered during the XRD measurements, and the higher stress level along the *XY* direction to the higher amount of Al grain boundaries investigated. The homogeneity in stress values obtained on the *1* and *2* directions of the top surface of the cubes is completely in accordance with the Al grains homogeneity evidenced in the EBSD map on the right of ***Fig. 5.13***.

In ***Fig. 5.14*** is reported the comparison of stress values calculated on L-PBF samples after the stress relieving treatment.

After SR the residual stress is decreased indicating that this annealing can release part, but not all, of the tensional stress present in the samples. In annealed samples, all values seem to collapse to the same stress level and the difference in stress along perpendicular direction of analysis seems to be reduced. This agrees with what known from literature [84], in which it is demonstrated that, after the stress relieving treatment, part of the columnar grains present along the building direction change into more equiaxic grains

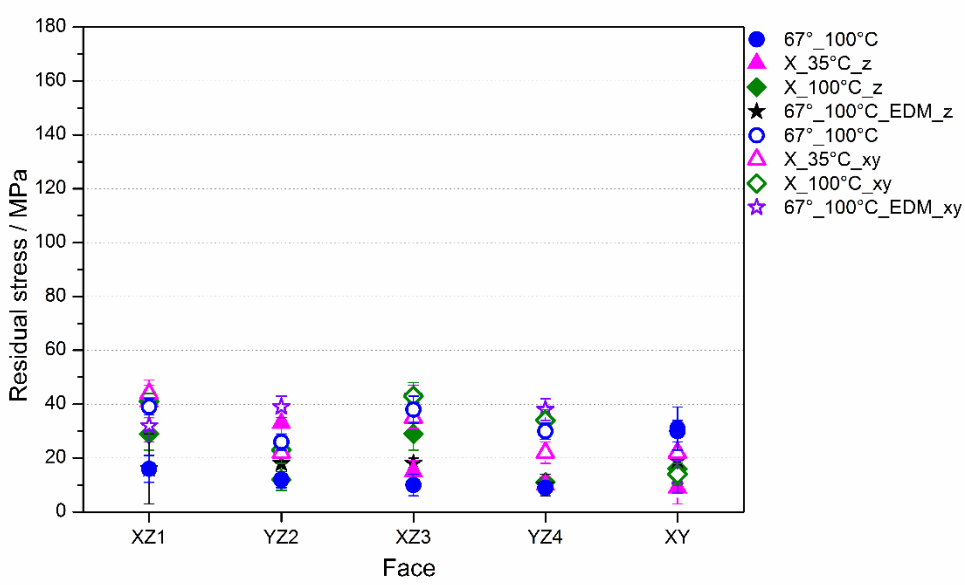

Fig. 5.14 *Comparison of the stress values obtained perpendicularly (XY/2) and parallel (Z/1) to the building direction for each face of the L-PBF samples after the stress relieving treatment.*

resulting, from the point of view of stress determination, into an increased homogeneity of the stress level along the two perpendicular directions.

To verify the homogeneity of stress results previously determined, it was evaluated if a stress gradient was present along a single surface of a sample. To do so, residual stress measurements were performed on 4 different areas of the same surface of the same sample moving from left to right and with the X-ray parallel to the building direction (*Z*). These measurements were performed on the raw *XZ1* surface of the AM_AB_67°_35°C, then were repeated on the same position on the same surface mechanically polished down to 40 nm, and again on the same surface after performing electropolishing. The same measurement was performed also on three points with the X-Ray beam perpendicular to the building direction (*XY*) on the electropolished surface. Results of these tests are reported in ***Fig. 5.15*** along with a schematic representation of where were performed the measurements.

From ***Fig. 5.15*** it was not evidenced a gradient in stress values along different positions of a single face; moreover, stress values obtained are fully

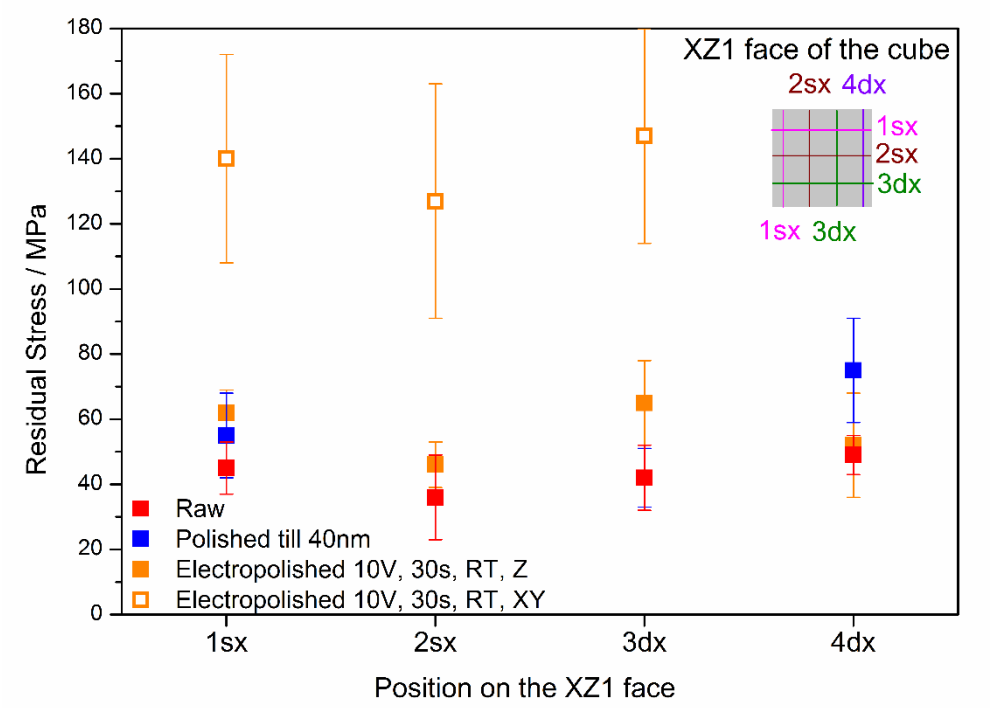

Fig. 5.15 *Residual stresses determined on the XZ1 face of the AM_AB_67°_35°C. Surface was analysed in the raw form (red squares), polished down to 40 nm (blue squares) and after electropolishing (orange squares). On the top left of the image is schematically represented where were performed the measurements along with their identification name.*

consistent with those determined on the raw sample. This result along with the value of stress obtained is reproducible for all the surface treatments performed on the sample, meaning that the portion of sample analysed is thick enough to avoid the surface roughness or deformation after mechanical polishing to influence the measurements.

The reproducibility of residual stress measurements on different positions of a single face and after different surface treatment was performed as a preliminary study before trying to evaluate how the residual stress level varies when moving from the upper part of the cube (XY face) towards the centre of the cube.

As far as the author knows no results of in-depth stress profile by XRD are reported in literature. The only result found being an in-depth stress determination performed by hole-drilling by Salmi et al. in [133] on different

L-PBF AlSi10Mg samples (both in AB condition and after the SR treatment). The results obtained by them for an as built AlSi10Mg sample, produced with support structures and employing the same set of process parameters employed in this work, are reported in black in ***Fig. 5.16***. In [133], the residual stress is found to have an oscillating nature and, in some cases, stress values are found to reach values well above the yielding strength of the material.

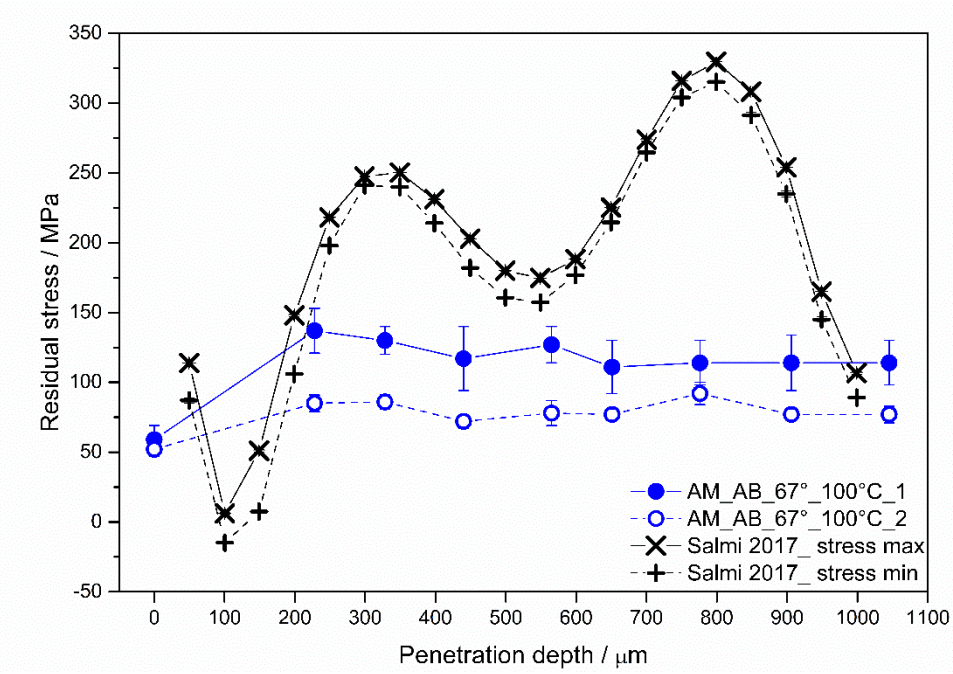

Fig. 5.16 *Determination of the stress level of the AM_AB_67°_100°C sample moving from the XY face of the cube towards its centre at steps of approximately 100 μm (blue). In black are reported the results obtained by Salmi et al. in [133] on a similar sample using hole drilling.*

To verify this oscillating trend when moving toward the core of an AB sample and evaluate the actual stress level in the sample, residual stress measurements by XRD were carried out removing material at steps of approximately 100 μm. XRD measurements were carried out along both the *1* and *2* directions. For all steps, in blue in ***Fig. 5.16***, the stress measured is tensile and lays approximately at 120 MPa along direction *1* and 80 MPa along direction *2*, all these values being considerably lower with respect to

those reported in [133]. Moreover, after a first increase in stress level when moving from the rough surface (considered as the zero point of penetration) to the first penetration step at approximately 200 μm, the stress level was found to remain constant for all the steps considered. At the rough surface the stress level along the *1* and *2* directions is the same, after removing layers of material there is a change in the stress state of the sample along the two perpendicular directions. This result can probably be explained considering that the cube is built in a layer by layer fashion and that the scanning strategy adopted implies a rotation of 67° in between each layer. So, when removing material from the top face of the cube, we will be in presence of a surface processed by the laser in a different way with respect to the previous one. Unfortunately, it was impossible to correlate the production process with the stress level found in the sample. However, on average the stress level measured for each step is approximately the same for both directions, meaning that, even if different rotation of the specimen can provide different stress values, the maximum difference in stress is that reported in ***Fig. 5.16***, as confirmed by the results reported in ***Fig. 5.17***, in which the results of residual stresses measured rotating the XY face of a sample along different directions are shown.

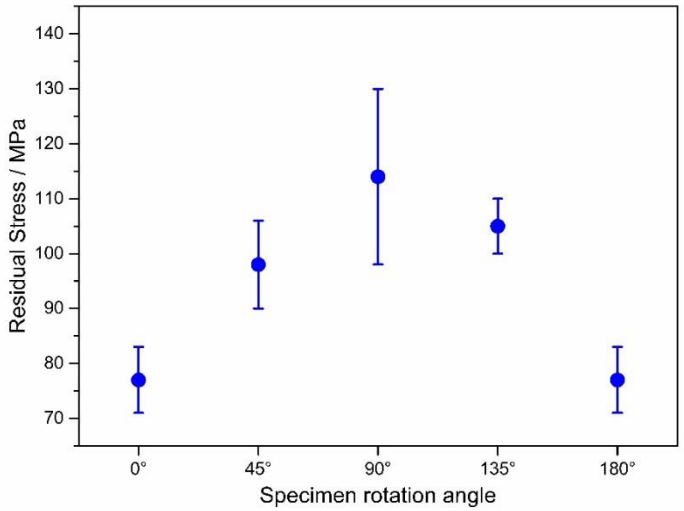

Fig. 5.17 *Residual stress variations when rotating the specimen of different angles with respect to directions 1 and 2. In this graph the 0° rotation angle corresponds to the direction 2 and the 90° rotation to the 1 direction in the previous graphs.*

5.3. Correlation of the two techniques

Both Raman spectroscopy and XRD suggested the presence of tensile residual stress in rapidly solidified samples, especially those produced by L-PBF in as built condition. The stress found with Raman spectroscopy, though, refers to the micro-stress on Si nano-crystals in the alloy, while stress determined by XRD refers to the macro-stress acting on the α-Al matrix.
Having these two set of measurements, the next step was to find a correlation between the stresses measured with these two techniques. This was done by applying the Williamson-Hall method for the determination of strains of both Al and Si from the XRD patterns acquired on the rapidly solidified AlSi10Mg samples. Another attempt to find a correlation was performed applying the simplified Eshelby model for the transmission of stress on composites starting from results on residual stress determined on Al through XRD.

5.3.1. Williamson-Hall method

The Williamson-Hall (WH) method exploits the analysis of X-ray peak broadening to evaluate size of the scattering domains and lattice strain of the phases under analysis. In particular, the WH method is a simplified integral breadth method in which both size-induced and strain-induced broadening are deconvoluted by considering the peak width as a function of 2θ [203,204].
The WH formula employed hereafter can be written as

$$\beta_{hkl}\cos\theta = \frac{K\lambda}{D} + 4\varepsilon\sin\theta$$

in which

$$\beta_{hkl} = \eta(\beta_{Lexp} - \beta_{instr}) + (1-\eta)\sqrt{\beta_{Gexp}^2 - \beta_{instr}^2}$$

In these formulae β_{hkl} is the broadening of the peaks corrected for the broadening of the instrumental function β_{instr} , i.e. the broadening

characteristic of the instrument employed for the analysis, D is the size of the scattering domains, K is a shape factor (0.94), λ is the wavelength of the incident radiation, ε is the strain induced in the lattice, θ is the Bragg angle and η describe how much the peaks under analysis are Lorentzian in shape.
Both the correction with the instrumental function and the shape of the reflections play a fundamental role in the correct evaluation of the results, for this reason calculations were performed carefully monitoring these parameters.
Employing these parameters, a plot in which $4\sin\theta$ represents the *x*-axis and $\beta_{hkl}\cos\theta$ the *y*-axis is drawn, and from the intercept and the slope of the linear fit of the data it is possible to calculate respectively the size of the scattering domains and the lattice strain. All reflections present in the diffraction patterns were analysed by fitting analytically the peak profile in order to collect information on peak position, Full Width at Half Maximum (FWHM) of the peak and Lorentzian contribution to peak shape [205]. Linear fitting of the data was performed considering a confidence level of 95%.An example of the fit performed on both Al and Si reflections and of the resulting Williamson-Hall plots is reported in ***Fig. 5.18***.
Here, the WH method was applied to the XRD patterns of the AlSi10Mg samples produced by means of different rapid solidification techniques and fully characterized in chapter 3, i.e. CMC cone, MS ribbons (both on air and wheel side) and L-PBF cubes both AB and after SR. Results obtained from the application of the model, along with stress level in the crystals obtained by simply multiplying for the Young modulus of the elements (70 GPa for Al and 140 GPa for Si), for both the Al and the Si reflections are reported in ***Table 5.3*** and ***Table 5.4*** respectively.

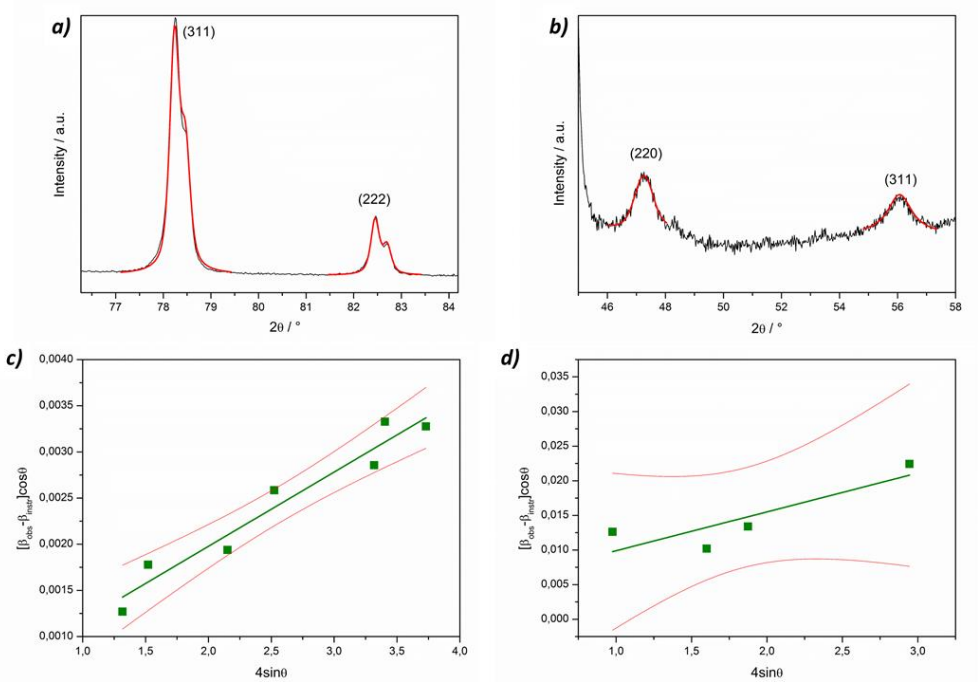

Fig. 5.18 *Example of both fitting and WH plots obtained for the AB sample both on Al and Si. In particular (a) and (c) represent respectively the peak fitting and the WH plot in the case of Al reflections, while (b) and (d) those of the Si reflections. Red lines in (c) and (d) represent the confidence bands used in the fitting.*

Table 5.3 *Results of the WH analysis from the Al reflections.*

	D_{Al} [nm]	$\langle \varepsilon_{Al}^2 \rangle^{1/2}$	σ_{Al} [MPa]
CMC	290 ± 348	0.0003 ± 0.0002	21 ± 14
MS	188 ± 191	0.0003 ± 0.0002	20 ± 12
AM_AB	362 ± 543	0.0008 ± 0.0002	56 ± 14
AM_SR	-	-	-

Table 5.4 *Results of the WH analysis from the Si reflections.*

	D_{Si} [nm]	$\langle \varepsilon_{Si}^2 \rangle^{1/2}$	σ_{Si} [MPa]
CMC	145 ± 579	0.0031 ± 0.0016	434 ± 224
MS	124 ± 529	0.003 ± 0.001	427 ± 182
AM_AB	36 ± 181	0.006 ± 0.010	840 ± 1400
AM_SR	241 ± 603	0.0018 ± 0.0006	252 ± 84

From these results it is evident that the determination of D comes with a large error for most of the samples, while the determination of stress seems to be more reliable (apart from the stress value obtained on Si for the AM_AB sample).

The uncertainty in the determination of the dimension of the scattering domains is related to the fact that both Al and Si crystals in these samples are considerably large with respect to those considered classically by the Williamson-Hall method; for this reason, when performing the linear regression, the intercept will lay close to 0 (corresponding to infinite scattering domains). In the case of the WH plot performed for Al reflections of the SR sample the intercept value obtained is found negative, for this reason no results were reported for this sample. Regarding the determination of D, wide error bars are obtained for both Al and Si; nevertheless, in the case of Si the hierarchy of Si crystals dimensions found in the micrographs in chapter 3 seems to be respected.

On the contrary, the stress level measured on the Al is always lower with respect to that measured for the Si; moreover, for the as built sample results seem to agree quite well with those obtained from the classical determination of residual stresses performed using XRD. Regarding the stress level measured on Si what is interesting is that the stress values reported in ***Table 5.4*** are of the same order of magnitude as those reported in ***Table 5.2*** regarding the stress level measured using Raman spectroscopy. Unfortunately, the result obtained for the AB sample comes with a wide error bar because of the limited amount of Si reflections observed in the XRD pattern. In fact, due to the extension of solid solubility achieved with the high cooling rate involved in the L-PBF process, only four reflections of Si can be analysed their intensity resulting low. This gave wider errors in fitting the peaks and consequently in the determination of both dimension of the scattering domains and strain.

The results obtained by applying the Williamson-Hall method were found to be quite interesting in correlating both the stress determined by conventional XRD and those obtained by Raman spectroscopy.

5.3.2. Eshelby's method

A further attempt to find a correlation between the stress level found with Raman and that determined by XRD was performed looking at the theory developed in the past for stress transfer from matrix to reinforcement particles in composites [115,148].

In [148] Harris et al. suggest that, in the elastic regime of deformation, it is possible to estimate the tensile stress in the particles, knowing which is the applied tensile strain of the composite, by applying the Eshelby's analysis for the pure shear case. Even if our material is not properly a composite, it is made of a softer matrix made of Al, reinforced by a stronger element, Si; so, following what done in [148], it was considered appropriate to apply this model to the Al-Si alloy.

The model describes the tensile stress acting on the reinforcement particles, σ_p, as:

$$\sigma_p = EK\varepsilon_c$$

in which

$$K = \frac{1+(1-f)\gamma M}{1-fM} \qquad \gamma = \frac{7-5\nu}{15(1-\nu)} \qquad M = \frac{\left(\frac{\mu^*}{\mu}-1\right)}{\left(\frac{\mu^*}{\mu}-1\right)\{1-\gamma(1-f)\}+1}$$

E and ν represent respectively Young modulus and Poisson ratio of the matrix (70 GPa and 0.33 for Al), ε_c stands for the applied tensile strain on the composite, f is the overall volume fraction of reinforcement, i.e. Si particles, and μ and μ^* are respectively the shear modulus of the matrix (here 24.81 GPa for Al) and of the reinforcing agent (here 66.41 GPa for Si).

The formula reported here is an approximation of the Eshelby analysis for the case of pure tension loading, but the fact that it is quite simple and was already applied on the same system in literature ([148]) made us choose this approximation.

Here, the applied tensile strain used for the determination of the particles stress was derived from the stress measured on Al through XRD, while the

overall volume fraction was taken as the amount of Si present in the alloy under investigation.

In ***Table 5.5*** are reported the results obtained by applying the model for the case of L-PBF samples in as built conditions, while results obtained on the samples subjected to stress relieving treatment are displayed in ***Table 5.6***.

All stresses calculated on Si applying this model considerably differs with respect to those obtained from both Raman spectroscopy and Williamson-Hall analysis.

At the present time there is not a straightforward explanation for this. What is assumed is an effect of Si crystals dimension in the determination of the stress level; in both Raman and WH, what influences the most the results is the presence of nanometric Si crystals, while the Eshelby's model is thought for reinforcement particles having considerably larger dimensions.

Knowing that the Eshelby's model and the experimental analysis performed account for different Si dimensions, what can be assumed is that the two results describe the different stress level experienced by larger (eutectic Si) and smaller (Si precipitates) crystals. Moreover, it is well known that both Raman spectroscopy and Williamson-Hall can be influenced by the presence lattice defects; so, another option could be that the stress derived from the Eshelby's model is the actual one transferred by the α-Al matrix to the Si crystals, while the higher values obtained with the other two techniques account also for the presence of defects increasing the stress level at the nanometric scale.

To verify these hypotheses and explain the discrepancy in numbers obtained by different models, further experiments and calculations will be performed in the next months.

Table 5.5 *Comparison of the stress level of as built samples determined on both Al and Si respectively by direct XRD measurements and by applying the approximate Eshelby analysis.*

Sample	*Face*	*Stress Al (Z) [MPa]*	*Stress Si (Z) [MPa]*	*Stress Al (XY) [MPa]*	*Stress Si (XY) [MPa]*
AM_AB_67°_35°C	*XZ1*	*46 ± 13*	*72 ± 20*	*94 ± 29*	*148 ± 46*
	YZ2	*66 ± 19*	*104 ± 30*	*72 ± 36*	*113 ± 56*
	XZ3	*59 ± 6*	*93 ± 9*	*101 ± 46*	*158 ± 72*
	YZ4	*33 ± 10*	*52 ± 16*	*81 ± 29*	*127 ± 46*
	XY	*48 ± 5*	*75 ± 8*	*52 ± 10*	*82 ± 16*
AM_AB_67°_100°C	*XZ1*	*37 ± 10*	*58 ± 16*	*127 ± 10*	*199 ± 16*
	YZ2	*36 ± 23*	*56 ± 36*	*81 ± 16*	*127 ± 25*
	XZ3	*39 ± 10*	*61 ± 16*	*130 ± 10*	*204 ± 16*
	YZ4	*46 ± 13*	*72 ± 20*	*101 ± 16*	*158 ± 25*
	XY	*59 ± 10*	*93 ± 16*	*52 ± 5*	*82 ± 8*
AM_AB_X_35°C	*XZ1*	*53 ± 8*	*83 ± 13*	*150 ± 13*	*235 ± 20*
	YZ2	*29 ± 13*	*46 ± 20*	*111 ± 19*	*174 ± 30*
	XZ3	*59 ± 13*	*93 ± 20*	*143 ± 13*	*224 ± 20*
	YZ4	*35 ± 9*	*55 ± 14*	*111 ± 16*	*174 ± 25*
	XY	*37 ± 5*	*58 ± 8*	*42 ± 10*	*66 ± 16*
AM_AB_X_100°C	*XZ1*	*52 ± 16*	*82 ± 25*	*104 ± 19*	*163 ± 30*
	YZ2	*36 ± 13*	*56 ± 20*	*107 ± 16*	*168 ± 25*
	XZ3	*36 ± 9*	*56 ± 14*	*88 ± 19*	*138 ± 30*
	YZ4	*33 ± 10*	*52 ± 16*	*112 ± 12*	*176 ± 19*
	XY	*46 ± 10*	*72 ± 16*	*39 ± 6*	*61 ± 9*
AM_AB_67°_100°C_EDM	*XZ1*	*29 ± 6*	*46 ± 9*	*130 ± 16*	*204 ± 25*
	YZ2	*29 ± 4*	*46 ± 6*	*117 ± 13*	*184 ± 20*
	XZ3	*33 ± 16*	*52 ± 25*	*130 ± 10*	*204 ± 16*
	YZ4	*33 ± 10*	*52 ± 16*	*101 ± 13*	*158 ± 20*
	XY	*55 ± 16*	*86 ± 25*	*49 ± 10*	*77 ± 16*

Table 5.6 *Comparison of the stress level of stress relieved samples determined on both Al and Si respectively by direct XRD measurements and by applying the Eshelby analysis for composites.*

Sample	*Face*	*Stress Al (Z) [MPa]*	*Stress Si (Z) [MPa]*	*Stress Al (XY) [MPa]*	*Stress Si (XY) [MPa]*
AM_SR_67°_100°C	*XZ1*	*16 ± 5*	*25 ± 8*	*39 ± 3*	*61 ± 5*
	YZ2	*12 ± 3*	*19 ± 5*	*26 ± 3*	*41 ± 5*
	XZ3	*10 ± 4*	*16 ± 6*	*38 ± 5*	*60 ± 8*
	YZ4	*9 ± 2*	*14 ± 3*	*30 ± 3*	*47 ± 5*
	XY	*31 ± 8*	*49 ± 13*	*30 ± 4*	*47 ± 6*
AM_SR_X_35°C	*XZ1*	*41 ± 6*	*64 ± 9*	*44 ± 5*	*69 ± 8*
	YZ2	*33 ± 1*	*52 ± 2*	*22 ± 2*	*35 ± 3*
	XZ3	*15 ± 4*	*24 ± 6*	*35 ± 4*	*55 ± 6*
	YZ4	*10 ± 3*	*16 ± 5*	*22 ± 4*	*35 ± 6*
	XY	*9 ± 6*	*14 ± 9*	*22 ± 4*	*35 ± 6*
AM_SR_X_100°C	*XZ1*	*29 ± 6*	*46 ± 9*	*41 ± 3*	*64 ± 5*
	YZ2	*12 ± 4*	*19 ± 6*	*23 ± 5*	*36 ± 8*
	XZ3	*29 ± 6*	*46 ± 9*	*43 ± 5*	*67 ± 8*
	YZ4	*11 ± 3*	*17 ± 5*	*34 ± 4*	*53 ± 6*
	XY	*16 ± 5*	*25 ± 8*	*14 ± 4*	*22 ± 6*
AM_SR_67°_100°C_EDM	*XZ1*	*16 ± 13*	*25 ± 20*	*32 ± 6*	*50 ± 9*
	YZ2	*18 ± 4*	*28 ± 6*	*39 ± 4*	*61 ± 6*
	XZ3	*18 ± 2*	*28 ± 3*	*43 ± 4*	*67 ± 6*
	YZ4	*10 ± 4*	*16 ± 6*	*38 ± 4*	*60 ± 6*
	XY	*19 ± 4*	*30 ± 6*	*13 ± 6*	*20 ± 9*

5.4. Conclusions

A study on the determination of residual stresses in AlSi10Mg samples produced by L-PBF and other rapid solidification techniques was carried out using both conventional and unconventional techniques, respectively XRD and Raman spectroscopy. In the end, a correlation was sought for the two techniques.

Raman measurements for the determination of residual stresses were performed on AlSi10Mg samples produced by means of different rapid solidification techniques, i.e. CMC, MS and L-PBF both in AB and SR condition. Increasing the cooling rate, the Raman peak was found to be red-shifted and broadened, while after the stress relieving treatment the signal of the L-PBF sample appeared to be blue-shifted close to equilibrium.

The shift observed in the samples was found to be indicative of both the presence of residual stresses and Si nano-crystals in the alloy. To discriminate between these two contributions the Campbell and Fauchet model modified by Brunetto and Amato was applied to evaluate the dimensional distribution of Si nano-crystals present in the rapidly solidified samples: results were compared with what identified by microscopy (using both FESEM and TEM). The presence of Si nano-crystals in the α-Al matrix of AB samples produced by L-PBF was verified with TEM and a good agreement between results obtained experimentally and results obtained from the model was evidenced by analysing the finer part of Si extracted from the alloy. Results obtained from the Raman spectra were compared with an experimentally determined curve correlating Raman shift and Si crystallite dimension proposed by Ossadnik in [160]; it was evidenced that all rapidly solidified samples give a Raman signal red-shifted indicating the presence of a tensional stress.

Starting from these results an approximate quantification of the stress level present in the different rapidly solidified samples was provided.

The presence of a tensional stress on L-PBF samples was confirmed from conventional stress measurements performed with XRD. Measurements were performed on five of the six faces of both AB and SR raw cubes and for each face two perpendicular directions were analysed, one parallel and one perpendicular to the building direction.

Different stress levels were found according to the direction of the measure on the lateral faces of the cubes, the one measured perpendicularly to the building direction being higher. This discrepancy was explained considering the differences in Al grain orientation observed by EBSD. The lower stress level obtained along the building direction was related to the lower amount of Al grain boundaries encountered during the XRD measurements, while the higher stress level perpendicularly to it to the higher amount of Al grain boundaries investigated. On the top face of the cubes, homogeneity in the stress level measured along the two perpendicular directions was observed, again this was found to agree with the equiaxic nature of Al grains evidenced by EBSD.

After SR the level of residual stress in the samples was found to decrease, indicating, as expected, that the thermal treatment releases the stresses present in the alloy. Moreover, the difference in stress level along the two perpendicular directions is reduced due to the modification of the Al grains morphology after thermal treatment.

Once determined the stress level of the raw faces of the cubes, an evaluation of the in-depth stress level was carried out, moving from the top surface to the core of the cube at steps of approximately 100 μm. Contrarily with what reported in [133], the stress level, measured with XRD, was found to remain constant throughout all the steps. This result was associated to a relaxation of the stresses related to the partial removal of material from the sample. Moreover, a difference along the two perpendicular dimensions of analysis was evidenced. This difference, that was not observed on the raw surface of the cubes, was explained considering that the cube is built in a layer by layer fashion and that the scanning strategy adopted implies a rotation of 67° in between each layer. So, when removing material from the top face of the cube, we will be in presence of a surface processed by the laser in a different way with respect to the previous ones.

Both Raman spectroscopy and XRD were found to suggest the presence of tensile residual stress in rapidly solidified samples. The stress found with Raman spectroscopy, though, refers to the micro-stress acting on the Si in the alloy, while the stress determined by XRD refers to the macro-stress

acting on the α-Al matrix. To investigate if there is a correlation in the results obtained with XRD and Raman, two different approaches were followed:

i. applying the Williamson-Hall method to the XRD patterns of rapidly solidified samples;
ii. applying a simplified Eshelby's model to estimate the stress level transferred from the Al to the Si.

The Williamson-Hall analysis performed on the XRD patterns of the rapidly solidified samples was found to provide interesting results on both the stress level of Al and Si. The stress determined for both the elements is of the same order of magnitude of that determined on Al by conventional XRD and on Si by Raman, validating the use of both these techniques to determine the stress level in rapidly solidified AlSi10Mg samples.
Results obtained applying the simplified Eshelby's model provided stress values considerably lower than those obtained by both Raman and WH. This result was suggested to be related to the different Si dimensions observed by the different techniques, i.e. Si precipitates influencing more Raman and WH and eutectic Si influencing more the Eshelby's approach. Another hypothesis that was drawn accounts for the possibility that the macro-stress level transferred from Al to Si is that determined by the Eshelby's model, but in Raman and WH also a micro-stress contribution, deriving from the presence of lattice defects, is accounted resulting in an overall increase in the stress level.

6. Summary and future perspectives

In this PhD thesis several open points of Additive Manufacturing were faced to advance in the knowledge of this innovative processing route.
First, starting from the wide knowledge on rapid solidification processes and the preparation of different test samples, the solidification mechanism of the AlSi10Mg alloy was determined.
The main results obtained in studying this topic are reported in the following points.

- A correlation between microstructure, phase constitution and thermal behaviour of AlSi10Mg samples produced by means of different rapid solidification techniques was established.
- A progressive change of eutectic Si morphology from dispersed particles to fibrous and lamellar network was evidenced. Microstructure being more refined in MS with respect to CMC samples and even more in L-PBF parts.
- The decrement of the Al lattice parameter when changing processing technique was found to give a measure of the extension of Si solid solubility in the primary phase.
- The surprising amount of solute Si in CMC and L-PBF samples was understood considering the fast cooling in the solid state provided by the intimate contact of the sample with the heat sink.
- The low solute content in MS samples must be associated to a decrease in cooling rate and consequent self-heating of the ribbon because of recalescence after detaching from the quenching wheel.
- The main DSC peak is due to Si precipitation, for which a correlation between the level of extended solid solubility and the onset temperature of the signal was evidenced: the lower is the temperature the higher is the amount of released enthalpy.
- Further exothermic signals are attributed to the precipitation of Mg_2Si and possibly Fe-containing intermetallics.
- Approximated metastable phase diagrams for the front velocities in between 0.5 and 1 m/s reproduce the eutectic fractions found in

experiments. Remarkably, these correspond to those directly measured in [195] by observing the movement of the primary solidification front in a hypoeutectic Al-Si alloy.

Once understood the correlation between conventional RS techniques and L-PBF, a route for designing new compositions specifically thought for AM, reducing the amount of material and time necessary for the testing, was implemented. This new testing route was verified completely for the addition of hardeners to the AlSi10Mg alloys. A preliminary work on the addition of typical grain refiners of Al alloys to the AlSi10Mg was also performed.
The main results obtained are reported in the following points.

- In all cases new alloys were obtained showing that compositional homogenization is feasible even when starting the production from a powder mixture.
- The microstructures of samples modified with hardeners indicate that the melt in SST is turbulent, whereas it is quiescent in MS.
- The microstructural morphology of the bulk sample produced by L-PBF with the most promising alloy, the AlSi10Mg+Cu, is similar to that of the melt spun ribbon, but intermediate between SST and MS in terms of cell size.
- In MS, SSTs and L-PBF the Cu forms to a large extent the Al_2Cu phase directly from the melt, which is intermixed with the eutectic.
- The presence of extended solid solubility of Si and both Ag and Cu respectively in AlSi10Mg+Ag and AlSi10Mg+Cu was evidenced.
- Cu supersaturation was estimated in between 0.75 at% and 1 at% in both L-PBF and MS samples. Precipitation of both Si and Al-Cu compounds occur on continuous heating at temperatures just above 200°C.
- An increase in hardness of the as prepared samples containing Cu with respect to that of the base AlSi10Mg alloy was evidenced by nano-indentation and Vickers tests, it is mostly related to the presence of Cu compounds intermixed with the eutectic.

- After the addition of inoculants (Er, nano-TiB_2 and Sr) to the AlSi10Mg alloy, the eutectic the Si results disrupted forming smaller Si crystals dispersed in the matrix.
- XRD patterns and lattice parameter calculations indicate the presence of extended solid solubility of Si. Supersaturation was found to be in the range 1 at% to 1.5 at%.
- No peculiar precipitation signals were identified after the additions of Er, nano-TiB_2 and Sr, but for all the samples a decrease in the enthalpy of Si precipitation was observed. This is in accordance with the increased nucleation frequency of Si when in presence of inoculants.
- Melting and solidification onset and offset temperatures were found to agree indicating that the presence of grain refiners does not induce alterations in the mechanisms of melting and solidification.
- Average hardness values were found to decrease with respect to that of the unmodified alloy indicating the continuous Si network as main responsible for the increase in hardness observed in rapidly solidified samples.
- The fact that the eutectic Si appears to be more disrupted, in principle can lead to a more homogeneous Si distribution inside bulk samples produced by AM, making mechanical properties more isotropic.
- The combination of the fast MS and SST techniques was proved effective in simulating the synthesis of new compositions and the properties of the alloy, this approach will allow to test rapidly alloys and to expand the material palette available for AM processes.

In the last part of the thesis, the presence of residual stresses in AlSi10Mg samples produced by L-PBF and other rapid solidification techniques was investigated using both an unconventional technique, i.e. Raman spectroscopy, and a conventional one, i.e. XRD.
The presence of a correlation for the stresses determined with the two techniques was investigated using the Williamson-Hall method and the simplified Eshelby's model.
The following points report the principal results obtained.

- Raman measurements were performed on AlSi10Mg samples produced by means of different rapid solidification techniques, i.e. CMC, MS and L-PBF in both AB and SR condition. Increasing the cooling rate, Raman peak was found to be red-shifted and broadened; after SR the signal of the L-PBF sample appeared to be blue-shifted close to equilibrium.
- The Campbell and Fauchet model, modified by Brunetto and Amato, was applied to determine the average dimensional distribution of Si nano-crystals present in the samples to discriminate between the shift provided by the small Si crystals and that provided by the presence of residual stresses.
- The presence of Si nano-crystals in the AB samples produced by L-PBF was verified with TEM. The dimensional distribution of Si nano-crystals determined experimentally was found to agree with the one determined with the modified Campbell and Fauchet model.
- Results obtained by the model were compared with an experimentally determined curve correlating Raman shift and Si dimensions; it was evidenced that results on rapidly solidified samples are all red-shifted indicating a tensional stress.
- Using the difference in shift from the experimentally determined curve, a quantitative evaluation of the stress present in the samples was provided.
- The presence of a tensional stress was confirmed from stress measurements performed with XRD.
- Measurements were performed on five of the six faces of both AB and SR raw cubes. For each face two perpendicular directions were analysed, one parallel and one perpendicular to the building direction.
- Different stresses were found according to the direction of measure on the lateral faces of the AB cubes, the one measured perpendicularly to the building direction being higher. This was explained considering the columnar orientation of Al grains observed by EBSD, i.e. the lower stress level obtained along the building direction was related to the lower amount of grain boundaries encountered during XRD, while the higher

stress level perpendicularly to it to the higher amount of grain boundaries investigated.

- On the top face of the cubes homogeneity in the stress level measured along the two perpendicular directions was observed, in accordance with the equiaxic nature of Al grains evidenced by EBSD.
- After SR the level of residual stress in the samples was found to decrease. The difference in stress level along the two perpendicular directions is reduced due to the modification of Al grains morphology after thermal treatment.
- An evaluation of the in-depth profile of stress was performed. The stress level was found to remain constant throughout all the steps. This was associated to the relaxation of the stresses related to the partial removal of the material.
- A difference along the two perpendicular dimensions of analysis was evidenced due to the fact that, when removing material from the top face of the cube, the surface under analysis will be processed by the laser in a different way with respect to the previous ones.
- Williamson-Hall analysis provided stress level compatible with those determined with both XRD and Raman spectroscopy validating the use of these two techniques for residual stress determination.
- The application of the simplified Eshelby model for composites, instead, provided stresses on Si considerably lower with respect to those determined with the other techniques. This result was explained considering that WH and Raman spectroscopy account more for nanometric Si, while the Eshelby model was developed for reinforcement particles of larger dimensions. It was suggested that the stress level obtained from the Eshelby's model is the one directly transferred from the matrix to both eutectic and Si precipitates, while that obtained with both WH and Raman account also for the presence of lattice defects inside the nano-crystals dispersed in the α-Al matrix.

In this thesis several open points in Additive Manufacturing were faced, but a lot of work is still necessary to make these techniques highly competitive in industrial processes.

For sure in the next months the work started adding inoculants to the AlSi10Mg alloy will be continued, producing both SSTs and bulk samples by L-PBF, to verify if the disruption of the eutectic Si is beneficial in terms of isotropy of mechanical properties.
Moreover, following the work performed on residual stress determination, further investigations on the correlation of results obtained by Raman and Williamson-Hall with what determined by the simplified Eshelby model will be performed, to verify if the presence of lattice defects can be responsible for the difference in stress level evidenced with the different techniques.

Acknowledgements

The experimental work reported in this thesis required the collaboration of several experts and institution so I will spend few words to thank all the people that were involved in this work.
First of all, I would like to acknowledge Politecnico di Torino (DISAT) and Istituto Italiano di Tecnologia (IIT) for providing me the L-PBF and SSTs samples and for the continuous and proficient collaboration during the whole project.
In particular, a big thank you goes to Dr. Diego Manfredi (DISAT/IIT) for involving me in this work with his great passion in research and for the huge amount of time spent with me acquiring FESEM micrographs always searching for something fancy and particular to see and talking about both science and future perspectives for life.
Moreover, I would like to thank Prof. Mariangela Lombardi, Dr. Alberta Aversa, Federico Bosio from DISAT, for their help in samples production and in the definition of the new Al alloys compositions reported in the thesis, and Dr. Massimo Lorusso from IIT, for his huge help in performing nanoindentation measurements.
Regarding the analysis on residual stresses a first acknowledgement goes to Dr. Enrica Bosco of GE Avio, for her help in understanding all the secrets related to residual stress determination in the industrial world and for providing us a “standard” for understanding if measurements were correct.
For Raman measurements a special thank you goes to both Dr. Giampiero Amato (INRIM), for its help in interpreting the results obtained on Si and for helping in the development of the modified Campbell and Fauchet model, and Dr. Alessandro Damin, for his constant help in calibrating the instrument and all the time spent with me looking for the best condition possible for the analysis.
For TEM measurements I would like to thank Prof. Paola Rizzi, that taught me all the secrets to prepare samples for TEM, and Dr. Maria Carmen Valsania, for all the time spent together looking for Si nano-crystals.
A huge acknowledgement goes to Dr. Gianluca Fiore for teaching me how to properly use and disassemble all the instruments in the Metallurgy Lab., for his help in the production of CMC and MS samples, for his courage in trying

with me to perform the first EBSD measurements ever tried in the Lab. and for all the ideas and advices shared in these three years.
It is easier to succeed if you are surrounded by a friendly environment, for this reason I would like to express my gratitude to all of my co-workers and students encountered during the last three years in the Metallurgy Lab.. Thank you to each one of you for sharing ideas, knowledge, laughter, gossip, crazy ideas, explosions and desks (yes Dario and Valerio this is for you!).
From a personal point of view, I would like to acknowledge my supervisor, Prof. Livio Battezzati, for his patience, support and advices during these three years and for teaching me that “there is only one thing that can not be changed, death” and that “there is a lot time in two weeks”.
A special thanks goes to my family and my friends that believed in me much more than myself and were always ready to push me to do my best even when I was having meltdowns.
Last but not least, I would like to acknowledge the STAMP project and Regione Piemonte for the financial support received during these three years and the committee, Prof. Jürgen Eckert, Prof. Riccardo Casati and Prof. Marcello Baricco, for reviewing this thesis and for their precious suggestions to improve the quality of this work.

List of abbreviations and symbols

Abbreviations

.stl	STereoLithography file
AB	As Built
AM	Additive Manufacturing
bct	Body centred tetragonal
CAD	Computer Aided Design
CMC	Copper Mould Casting
D	Detector
DED	Direct Energy Deposition
DMLS	Direct Metal Laser Sintering
DSC	Differential Scanning Calorimetry
EBSD	Electron Back Scattered Diffraction
EDX	Energy Dispersive X-Ray spectroscopy
fcc	Face centred cubic
FESEM	Field Emission Scanning Electron Microscope
FWHM	Full Width at Half Maximum
GA	Grazing Angle
haz	Heat affected zone
LAS	Leica Application Suite
LO	Longitudinal Optical mode
L-PBF	Laser Powder Bed Fusion
mpb	Melt pool border
mpc	Melt pool centre

MS	Melt Spinning
OM	Optical Microscopy
PBF	Powder Bed Fusion
PM	Powder Metallurgy
RS	Rapid Solidification
SEM	Scanning Electron Microscope
SLA	StereoLithographic Apparatus
SLM	Selective Laser Melting
SLS	Selective Laser Sintering
SP	Specimen
SR	Stress Relieved
SST	Laser Single Scan Track
TEM	Transmission Electron Microscope
TO	Transverse Optic mode
WH	Williamson-Hall method
XRD	X-Ray Diffraction

Symbols

$(1-\eta)$	Gaussian contribution to peak shape
$\overrightarrow{q_0}$	Generic wavevector
h_d	Hatching distance
C_L	Liquid composition
D_i	Interface diffusion coefficient
P_i	Interface Pèclet number
S_1, S_2, S_3	Sample coordinate system
S_{11}, S_{12}, S_{44}	Elastic compliances
$\dot{T}$	Cooling rate
T_0	Temperature of equal free energy for two phases
T_L	*Liquidus* temperature
T_M	Melting temperature
V_0	Limiting crystallization velocity
a_0	Interface diffusion length
d_0	Unstressed interplanar spacing
$d_{\phi\Psi}$	Measured interplanar spacing
k_v	Non-equilibrium distribution coefficient
m_a	Atomic mass of Si
$\vec{r}$	Vector of the crystalline lattice
x_{Si}	Atomic percentage of solute Si
β_{hkl}	Full Width at Half Maximum of the diffraction peak
β_{Gexp}	Full Width at Half Maximum measured on the pattern for the Gaussian component

β_{Lexp}	Full Width at Half Maximum measured on the pattern for the Lorentzian component
β_{instr}	Full Width at Half Maximum of the instrumental function
ε_c	Applied tensile strain of the composite
$\varepsilon_{\phi\Psi}$	Strain vector
μ^*	Shear modulus of Si reinforcing particles
μ_k	Interface kinetic coefficient
σ_1, σ_2	Stress components
σ^2	Variance
σ_p	Tensile stress in the reinforcing particle
σ_ϕ	Surface stress component
2θ	Diffraction angle
C_S	Solid composition
h, k, l	Miller indices of the crystallographic planes
ø	Diameter
Ψ	Tilting angle
$\Psi(\overrightarrow{q_0}, \vec{r})$	Wave function of the phonon in the nanocrystal
v	Poisson ratio
C	Alloy composition
$C(\overrightarrow{q_0}, \vec{r})$	Coefficients of the Fourier series
D	Size of the scattering domains
E	Young modulus
G	Thermal gradient
$I(\omega)$	Intensity of the Lorentzian
K	Shape factor (0.94)
L	Dimension of the nanocrystal

P	Laser power
R	Solidification rate
V	Rate of interface movement
$W(\vec{r}, L)$	Phonon weighting function
X	X-ray tube
Y	Young modulus of porous Si
a	Lattice parameter
d	Interplanar distance
$dF(x)$	Lognormal function describing size distribution
f	Overall volume fraction of Si particles
k	Equilibrium distribution coefficient
m	*Liquidus* slope
n	Integer representing the scattering order
r	Dendrite tip radius
$u(\overrightarrow{q_0}, \vec{r})$	Periodicity of the lattice
v	Scanning speed
x	Average information depth
Γ	Gibbs-Thompson coefficient
Γ	Gibbs-Thompson coefficient
$\Phi(\overrightarrow{q_0}, \vec{r})$	Generic wave function
γ	Bandwidth corresponding to Full Width at Half Maximum
ε	Lattice strain
η	Lorentzian contribution to peak shape
θ	Bragg angle
λ	Wavelength of the incident X-Ray beam
μ	Shear modulus of the composite matrix (Al)

ρ	Mode of the lognormal distribution
χ	Most probable value of x
ω	$\Psi + \theta$
$\omega(q)$	Theoretical wavenumbers
ωR	Rotation about ω axis
ϕR	Rotation about ϕ axis

List of Figures

List of Tables

References

[1] J.O. Milewski, Additive Manufacturing of Metals *From Fundamental Technology to Rocket Nozzles, Medical Implants, and Custom Jewelry*, Springer Series in Material Science 258, 2017. doi:10.1007/978-3-319-58205-4.

[2] W.J. Sames, F.A. List, S. Pannala, R.R. Dehoff, S.S. Babu, *The metallurgy and processing science of metal additive manufacturing*, Int. Mater. Rev. 61 (2016) 315–360. doi:10.1080/09506608.2015.1116649.

[3] T. Wohlers, I. Campbell, O. Diegel, J. Kowen, *Wohlers report 2017*, Wohlers Associate, INC., 2017.

[4] ASTM Internationals, *ASTM F2792-12a: Standard terminology for additive manufacturing technologies*, (2012). doi:10.1520/F2792-12A.2.

[5] D. Manfredi, F. Calignano, E.P. Ambrosio, M. Krishnan, R. Canali, S. Biamino, M. Pavese, E. Atzeni, L. Luliano, P. Fino, C. Badini, *Direct Metal Laser Sintering: An additive manufacturing technology ready to produce lightweight structural parts for robotic applications*, Metall. Ital. 105 (2013) 15–24.

[6] I. Gibson, D. Rosen, B. Stucker, *Additive Manufacturing Technologies 3D Printing, Rapid Prototyping, and Direct Digital Manufacturing*, Second Ed., Springer New York Heidelberg Dordrecht London, 2015.

[7] C.Y. Yap, C.K. Chua, Z.L. Dong, Z.H. Liu, D.Q. Zhang, L.E. Loh, S.L. Sing, *Review of selective laser melting: Materials and applications*, Appl. Phys. Rev. 2 (2015) 1–21.

[8] D. Manfredi, F. Calignano, M. Krishnan, R. Canali, E.P. Ambrosio, S. Biamino, D. Ugues, M. Pavese, P. Fino, *Additive Manufacturing of Al Alloys and Aluminium Matrix Composites (AMCs)*, Light Met. Alloy. Appl. (2014) 3–34. doi:10.5772/57069.

[9] K.G. Prashanth, S. Scudino, H.J. Klauss, K.B. Surreddi, L. Löber, Z. Wang, A.K. Chaubey, U. Kühn, J. Eckert, *Microstructure and mechanical properties of Al-12Si produced by selective laser melting: Effect of heat treatment*, Mater. Sci. Eng. A. 590 (2014) 153–160. doi:10.1016/j.msea.2013.10.023.

[10] J. Suryawanshi, K.G. Prashanth, S. Scudino, J. Eckert, O. Prakash, U.

Ramamurty, *Simultaneous enhancements of strength and toughness in an Al-12Si alloy synthesized using selective laser melting*, Acta Mater. 115 (2016) 285–294. doi:10.1016/j.actamat.2016.06.009.

[11] L. Zhou, A. Mehta, E. Schulz, B. McWilliams, K. Cho, Y. Sohn, *Microstructure, precipitates and hardness of selectively laser melted AlSi10Mg alloy before and after heat treatment*, Mater. Charact. 143 (2018) 5–17. doi:10.1016/j.matchar.2018.04.022.

[12] F. Trevisan, F. Calignano, M. Lorusso, J. Pakkanen, A. Aversa, E.P. Ambrosio, M. Lombardi, P. Fino, D. Manfredi, *On the selective laser melting (SLM) of the AlSi10Mg alloy: Process, microstructure, and mechanical properties*, Materials (Basel). 10 (2017). doi:10.3390/ma10010076.

[13] N. Kang, P. Coddet, M.R. Ammar, H. Liao, C. Coddet, *Characterization of the microstructure of a selective laser melting processed Al-50Si alloy: Effect of heat treatments*, Mater. Charact. 130 (2017) 243–249. doi:10.1016/j.matchar.2017.06.026.

[14] R. Casati, M. Vedani, *Aging Response of an A357 Al Alloy Processed by Selective Laser Melting*, Adv. Eng. Mater. (2018) 1800406. doi:10.1002/adem.201800406.

[15] U. Tradowsky, J. White, R.M. Ward, N. Read, W. Reimers, M.M. Attallah, *Selective Laser Melting of AlSi10Mg: Influence of Post-Processing on the Microstructural and Tensile Properties Development*, Mater. Des. 105 (2016) 212–222. doi:10.1016/j.matdes.2016.05.066.

[16] W. Li, S. Li, J. Liu, A. Zhang, Y. Zhou, Q. Wei, C. Yan, Y. Shi, *Effect of heat treatment on AlSi10Mg alloy fabricated by selective laser melting: Microstructure evolution, mechanical properties and fracture mechanism*, Mater. Sci. Eng. A. 663 (2016) 116–125. doi:10.1016/j.msea.2016.03.088.

[17] J. Wu, X.Q. Wang, W. Wang, M.M. Attallah, M.H. Loretto, *Microstructure and strength of selectively laser melted AlSi10Mg*, Acta Mater. 117 (2016) 311–320. doi:10.1016/j.actamat.2016.07.012.

[18] D. Manfredi, F. Calignano, M. Krishnan, R. Canali, E.P. Ambrosio, E. Atzeni, *From powders to dense metal parts: Characterization of a commercial AlSiMg alloy processed through Direct Metal Laser Sintering*, Materials (Basel). 6 (2013) 856–869. doi:10.3390/ma6030856.

[19] L. Thijs, K. Kempen, J.P. Kruth, J. Van Humbeeck, *Fine-structured aluminium products with controllable texture by selective laser melting of pre-alloyed AlSi10Mg powder*, Acta Mater. 61 (2013) 1809–1819. doi:10.1016/j.actamat.2012.11.052.

[20] R. Casati, M.H. Nasab, M. Coduri, V. Tirelli, M. Vedani, *Effects of Platform Pre-Heating and Thermal-Treatment Strategies on Properties of AlSi10Mg Alloy Processed by Selective Laser Melting*, Metals (Basel). 8 (2018) 954. doi:10.3390/met8110954.

[21] M. Wang, B. Song, Q. Wei, Y. Zhang, Y. Shi, *Effects of annealing on the microstructure and mechanical properties of selective laser melted AlSi7Mg alloy*, Mater. Sci. Eng. A. 739 (2019) 463–472. doi:10.1016/j.msea.2018.10.047.

[22] B.A. Fulcher, D.K. Leigh, T.J. Watt, *Comparison of AlSi10Mg and Al6061 processed through DMLS*, in: Proceeding Solid Free. Fabr. Symp., Austin, TX, USA, 2014: pp. 404–419.

[23] O. Gharbi, D. Jiang, D.R. Feenstra, S.K. Kairy, Y. Wu, C.R. Hutchinson, N. Birbilis, *On the corrosion of additively manufactured aluminium alloy AA2024 prepared by selective laser melting*, Corros. Sci. 143 (2018) 93–106. doi:10.1016/j.corsci.2018.08.019.

[24] K. Schmidtke, F. Palm, A. Hawkins, C. Emmelmann, *Process and mechanical properties: Applicability of a Scandium modified Al-alloy for Laser Additive Manufacturing*, Phys. Procedia. 12 (2011) 369–374. doi:10.1016/j.phpro.2011.03.047.

[25] A.B. Spierings, K. Dawson, M. Voegtlin, F. Palm, P.J. Uggowitzer, *Microstructure and mechanical properties of as-processed scandium-modified aluminium using selective laser melting*, CIRP Ann. - Manuf. Technol. 65 (2016) 213–216. doi:10.1016/j.cirp.2016.04.057.

[26] A.B. Spierings, K. Dawson, P. Dumitraschkewitz, S. Pogatscher, K. Wegener, *Microstructure characterization of SLM-processed Al-Mg-Sc-Zr alloy in the heat treated and HIPed condition*, Addit. Manuf. 20 (2018) 173–181. doi:10.1016/j.addma.2017.12.011.

[27] M. Awd, J. Tenkamp, M. Hirtler, S. Siddique, M. Bambach, F. Walther, *Comparison of microstructure and mechanical properties of Scalmalloy® produced by Selective Laser Melting and Laser Metal Deposition*, Materials (Basel). 11 (2017). doi:10.3390/ma11010017.

[28] A.B. Spierings, K. Dawson, P.J. Uggowitzer, K. Wegener, *Influence of SLM scan-speed on microstructure, precipitation of Al_3Sc particles and mechanical properties in Sc- and Zr-modified Al-Mg alloys*, Mater. Des. 140 (2018) 134–143. doi:10.1016/j.matdes.2017.11.053.

[29] A.B. Spierings, K. Dawson, T. Heeling, P.J. Uggowitzer, R. Schäublin, F. Palm, K. Wegener, *Microstructural features of Sc- and Zr-modified Al-Mg alloys processed by selective laser melting*, Mater. Des. 115 (2017) 52–63. doi:10.1016/j.matdes.2016.11.040.

[30] A.B. Spierings, K. Dawson, K. Kern, F. Palm, K. Wegener, *SLM-processed Sc- and Zr- modified Al-Mg alloy: Mechanical properties and microstructural effects of heat treatment*, Mater. Sci. Eng. A. 701 (2017) 264–273. doi:10.1016/j.msea.2017.06.089.

[31] P. Wang, L. Deng, K.G. Prashanth, S. Pauly, J. Eckert, S. Scudino, *Microstructure and mechanical properties of Al-Cu alloys fabricated by selective laser melting of powder mixtures*, J. Alloys Compd. 735 (2018) 2263–2266. doi:10.1016/j.jallcom.2017.10.168.

[32] G. Barucca, E. Santecchia, G. Majni, E. Girardin, E. Bassoli, L. Denti, A. Gatto, L. Iuliano, T. Moskalewicz, P. Mengucci, *Structural characterization of biomedical Co-Cr-Mo components produced by direct metal laser sintering*, Mater. Sci. Eng. C. 48 (2015) 263–269. doi:10.1016/j.msec.2014.12.009.

[33] K.M. Mantrala, M. Das, V.K. Balla, C.S. Rao, V.V.S. Kesava Rao, *Additive Manufacturing of Co-Cr-Mo Alloy: Influence of Heat Treatment on Microstructure, Tribological, and Electrochemical Properties*, Front. Mech. Eng. 1 (2015) 1–7. doi:10.3389/fmech.2015.00002.

[34] A.G. Demir, B. Previtali, *Additive manufacturing of cardiovascular CoCr stents by selective laser melting*, Mater. Des. 119 (2017) 338–350. doi:10.1016/j.matdes.2017.01.091.

[35] F. Trevisan, F. Calignano, M. Lorusso, M. Lombardi, D. Manfredi, P. Fino, *Selective laser melting of chemical pure copper powders*, in: Proc. Euro PM2017 Congr. Exhib., Milan, Italy, 2017.

[36] S. Scudino, C. Unterdörfer, K.G. Prashanth, H. Attar, N. Ellendt, V. Uhlenwinkel, J. Eckert, *Additive manufacturing of Cu-10Sn bronze*, Mater. Lett. 156 (2015) 202–204. doi:10.1016/j.matlet.2015.05.076.

[37] M. Khan, P.M. Dickens, *Processing parameters for Selective Laser*

Melting (SLM) of gold, Proc. Solid Free. Fabr. Symp. (2008) 278–289.

[38] Q. Jia, D. Gu, *Selective laser melting additive manufacturing of Inconel 718 superalloy parts: Densification, microstructure and properties*, J. Alloys Compd. 585 (2014) 713–721. doi:10.1016/j.jallcom.2013.09.171.

[39] Z. Wang, K. Guan, M. Gao, X. Li, X. Chen, X. Zeng, *The microstructure and mechanical properties of deposited-IN718 by selective laser melting*, J. Alloys Compd. 513 (2012) 518–523. doi:10.1016/j.jallcom.2011.10.107.

[40] K. Mumtaz, N. Hopkinson, *Selective Laser Melting of Inconel 625 Using Pulse Shaping*, Rapid Prototyp. J. 16 (2010) 248–257. doi:10.1108/13552541011049261.

[41] K. Mumtaz, N. Hopkinson, *Top surface and side roughness of Inconel 625 parts processed using selective laser melting*, Rapid Prototyp. J. 15 (2009) 96–103. doi:10.1108/13552540910943397.

[42] F. Wang, *Mechanical property study on rapid additive layer manufacture Hastelloy® X alloy by selective laser melting technology*, Int. J. Adv. Manuf. Technol. 58 (2012) 545–551. doi:10.1007/s00170-011-3423-2.

[43] A. Riemer, S. Leuders, M. Thöne, H.A. Richard, T. Tröster, T. Niendorf, *On the fatigue crack growth behavior in 316L stainless steel manufactured by selective laser melting*, Eng. Fract. Mech. 120 (2014) 15–25. doi:10.1016/j.engfracmech.2014.03.008.

[44] C. Yan, L. Hao, A. Hussein, P. Young, D. Raymont, *Advanced lightweight 316L stainless steel cellular lattice structures fabricated via selective laser melting*, Mater. Des. 55 (2014) 533–541. doi:10.1016/j.matdes.2013.10.027.

[45] J.A. Cherry, H.M. Davies, S. Mehmood, N.P. Lavery, S.G.R. Brown, J. Sienz, *Investigation into the effect of process parameters on microstructural and physical properties of 316L stainless steel parts by selective laser melting*, Int. J. Adv. Manuf. Technol. 76 (2015) 869–879. doi:10.1007/s00170-014-6297-2.

[46] R. Casati, J. Lemke, M. Vedani, *Microstructure and Fracture Behavior of 316L Austenitic Stainless Steel Produced by Selective Laser Melting*, J. Mater. Sci. Technol. 32 (2016) 738–744.

doi:10.1016/j.jmst.2016.06.016.

[47] Z. Sun, X. Tan, S.B. Tor, W.Y. Yeong, *Selective laser melting of stainless steel 316L with low porosity and high build rates*, Mater. Des. 104 (2016) 197–204. doi:10.1016/j.matdes.2016.05.035.

[48] E. Liverani, S. Toschi, L. Ceschini, A. Fortunato, *Effect of selective laser melting (SLM) process parameters on microstructure and mechanical properties of 316L austenitic stainless steel*, J. Mater. Process. Technol. 249 (2017) 255–263. doi:10.1016/j.jmatprotec.2017.05.042.

[49] B. Clausen, D.W. Brown, J.S. Carpenter, K.D. Clarke, A.J. Clarke, S.C. Vogel, J.D. Bernardin, D. Spernjak, J.M. Thompson, *Deformation behavior of additively manufactured GP1 stainless steel*, Mater. Sci. Eng. A. 696 (2017) 331–340. doi:10.1016/j.msea.2017.04.081.

[50] M. Islam, T. Purtonen, H. Piili, A. Salminen, O. Nyrhilä, *Temperature profile and imaging analysis of laser additive manufacturing of stainless steel*, Phys. Procedia. 41 (2013) 835–842. doi:10.1016/j.phpro.2013.03.156.

[51] S. Pal, H.R. Tiyyagura, I. Drstvenšek, C.S. Kumar, *The effect of post-processing and machining process parameters on properties of stainless steel PH1 product produced by Direct Metal Laser Sintering*, Procedia Eng. 149 (2016) 359–365. doi:10.1016/j.proeng.2016.06.679.

[52] H. Asgari, M. Mohammadi, *Microstructure and mechanical properties of stainless steel CX manufactured by Direct Metal Laser Sintering*, Mater. Sci. Eng. A. 709 (2018) 82–89. doi:10.1016/j.msea.2017.10.045.

[53] E.A. Jägle, P.P. Choi, J. Van Humbeeck, D. Raabe, *Precipitation and austenite reversion behavior of a maraging steel produced by selective laser melting*, J. Mater. Res. 29 (2014) 2072–2079. doi:10.1557/jmr.2014.204.

[54] D. Croccolo, M. De Agostinis, S. Fini, G. Olmi, A. Vranic, S. Ciric-Kostic, *Influence of the build orientation on the fatigue strength of EOS maraging steel produced by additive metal machine*, Fatigue Fract. Eng. Mater. Struct. 39 (2016) 637–647. doi:10.1111/ffe.12395.

[55] Y. Bai, Y. Yang, D. Wang, M. Zhang, *Influence mechanism of parameters process and mechanical properties evolution mechanism of maraging steel 300 by selective laser melting*, Mater. Sci. Eng. A. 703 (2017) 116-123. doi:10.1016/j.msea.2017.06.033.

[56] C. Tan, K. Zhou, W. Ma, P. Zhang, M. Liu, T. Kuang, *Microstructural evolution, nanoprecipitation behavior and mechanical properties of selective laser melted high-performance grade 300 maraging steel*, Mater. Des. 134 (2017) 23–34. doi:10.1016/j.matdes.2017.08.026.

[57] L. Thijs, F. Verhaeghe, T. Craeghs, J. Van Humbeeck, J.P. Kruth, *A study of the microstructural evolution during selective laser melting of Ti-6Al-4V*, Acta Mater. 58 (2010) 3303–3312. doi:10.1016/j.actamat.2010.02.004.

[58] W. Xu, M. Brandt, S. Sun, J. Elambasseril, Q. Liu, K. Latham, K. Xia, M. Qian, *Additive manufacturing of strong and ductile Ti-6Al-4V by selective laser melting via in situ martensite decomposition*, Acta Mater. 85 (2015) 74–84. doi:10.1016/j.actamat.2014.11.028.

[59] J. Sun, X. Zhu, L. Qiu, F. Wang, Y. Yang, L. Guo, *The microstructure transformation of selective laser melted Ti-6Al-4V alloy*, Mater. Today Commun. 19 (2019) 277–285. doi:10.1016/j.mtcomm.2019.02.006.

[60] M. Simonelli, Y.Y. Tse, C. Tuck, *Effect of the build orientation on the mechanical properties and fracture modes of SLM Ti-6Al-4V*, Mater. Sci. Eng. A. 616 (2014) 1–11. doi:10.1016/j.msea.2014.07.086.

[61] B. Vrancken, L. Thijs, J.-P. Kruth, J. Van Humbeeck, *Heat treatment of Ti6Al4V produced by Selective Laser Melting: Microstructure and mechanical properties*, J. Alloys Compd. 541 (2012) 177–185. doi:10.1016/j.jallcom.2012.07.022.

[62] S. Leuders, M. Thöne, A. Riemer, T. Niendorf, T. Tröster, H.A. Richard, H.J. Maier, *On the mechanical behaviour of titanium alloy TiAl6V4 manufactured by selective laser melting: Fatigue resistance and crack growth performance*, Int. J. Fatigue. 48 (2013) 300–307. doi:10.1016/j.ijfatigue.2012.11.011.

[63] T. DebRoy, H.L. Wei, J.S. Zuback, T. Mukherjee, J.W. Elmer, J.O. Milewski, A.M. Beese, A. Wilson-Heid, A. De, W. Zhang, *Additive manufacturing of metallic components – Process, structure and properties*, Prog. Mater. Sci. 92 (2018) 112–224. doi:10.1016/j.pmatsci.2017.10.001.

[64] E.O. Olakanmi, R.F. Cochrane, K.W. Dalgarno, *A review on selective laser sintering/melting (SLS/SLM) of aluminium alloy powders: Processing, microstructure, and properties*, Prog. Mater. Sci. 74 (2015) 401–477. doi:10.1016/j.pmatsci.2015.03.002.

[65] B. Vrancken, L. Thijs, J.P. Kruth, J. Van Humbeeck, J. Van Humbeeck, *Microstructure and mechanical properties of a novel β titanium metallic composite by selective laser melting*, Acta Mater. 68 (2014) 150–158. doi:10.1016/j.actamat.2014.01.018.

[66] A. Aversa, M. Lorusso, G. Cattano, D. Manfredi, F. Calignano, E.P. Ambrosio, S. Biamino, P. Fino, M. Lombardi, M. Pavese, *A study of the microstructure and the mechanical properties of an Al-Si-Ni alloy produced via selective laser melting*, J. Alloys Compd. 695 (2017) 1470–1478. doi:10.1016/j.jallcom.2016.10.285.

[67] R. Meharabian, B.H. Kear, M. Cohen, *Rapid Solidification Processing an outlook*, in: R. Meharabian, B.H. Kear, M. Cohen (Eds.), Rapid Solidif. Process. Princ. Technol., Claitor's Publishing Division, Reston,Virginia,U.S.A., 1980: pp. 1–23.

[68] B.H. Kear, B.C. Giessen, M. Cohen, *Rapidly solidified Amorphous and Crystalline Alloys*, in: B.H. Kear, B.C. Giessen, M. Cohen (Eds.), Proc. Mater. Res. Soc. Annu. Meet., Elsevier Science Publishing Co., Boston, Massachussetts, U.S.A., Massachussetts, U.S.A., 1981.

[69] H.H. Liebermann, *Rapidly solidified alloys*, Maecrel Dekker, INC., New York, New York, U.S.A., New York, U.S.A., 1993.

[70] S. Steeb, H. Warlimont, *Rapidly quenched metals*, in: S. Steeb, H. Warlimont (Eds.), Proc. Fifth Int. Conf. Rapidly Quenched Met., North-Holland Physics Publishing, Wurzburg, Germany, Germany, 1984.

[71] B.H. Kear, E.M. Breinan, E.R. Thompson, *Laser Processing of Materials*, in: J.J. Burke, R. Mehrabian, V. Weiss (Eds.), Adv. Met. Process. Sagamore Army Mater. Res. Conf. Proc., Springer, Boston, MA, U.S.A., 1981: pp. 45–78.

[72] I.J. Polmear, *Light Alloys*, Third Edit, Arnold, London, GB, GB, 1995.

[73] J.R. Davis, *Metals Handbook*, Second Edi, ASM International, 1998.

[74] G.P. Dinda, A.K. Dasgupta, J. Mazumder, *Evolution of microstructure in laser deposited Al-11.28%Si alloy*, Surf. Coatings Technol. 206 (2012) 2152–2160. doi:10.1016/j.surfcoat.2011.09.051.

[75] E.O. Olakanmi, *Selective laser sintering/melting (SLS/SLM) of pure Al, Al-Mg, and Al-Si powders: Effect of processing conditions and powder properties*, J. Mater. Process. Technol. 213 (2013) 1387–1405. doi:10.1016/j.jmatprotec.2013.03.009.

[76] N.T. Aboulkhair, N.M. Everitt, I. Ashcroft, C. Tuck, *Reducing porosity in AlSi10Mg parts processed by selective laser melting*, Addit. Manuf. 1 (2014) 77–86. doi:10.1016/j.addma.2014.08.001.

[77] P. Ma, K. Prashanth, S. Scudino, Y. Jia, H. Wang, C. Zou, Z. Wei, J. Eckert, *Influence of Annealing on Mechanical Properties of Al-20Si Processed by Selective Laser Melting*, Metals (Basel). 4 (2014) 28–36. doi:10.3390/met4010028.

[78] L.P. Lam, D.Q. Zhang, Z.H. Liu, C.K. Chua, *Phase analysis and microstructure characterisation of AlSi10Mg parts produced by Selective Laser Melting*, Virtual Phys. Prototyp. 10 (2015) 207–215. doi:10.1080/17452759.2015.1110868.

[79] X.P. Li, X.J. Wang, M. Saunders, A. Suvorova, L.C. Zhang, Y.J. Liu, M.H. Fang, Z.H. Huang, T.B. Sercombe, *A selective laser melting and solution heat treatment refined Al-12Si alloy with a controllable ultrafine eutectic microstructure and 25% tensile ductility*, Acta Mater. 95 (2015) 74–82. doi:10.1016/j.actamat.2015.05.017.

[80] N. Read, W. Wang, K. Essa, M.M. Attallah, *Selective laser melting of AlSi10Mg alloy: Process optimisation and mechanical properties development*, Mater. Des. 65 (2015) 417–424. doi:10.1016/j.matdes.2014.09.044.

[81] J. Fiocchi, A. Tuissi, P. Bassani, C.A. Biffi, *Low temperature annealing dedicated to AlSi10Mg selective laser melting products*, J. Alloys Compd. 695 (2017) 3402–3409. doi:10.1016/j.jallcom.2016.12.019.

[82] N. Kang, P. Coddet, H. Liao, C. Coddet, *Macrosegregation mechanism of primary silicon phase in selective laser melting hypereutectic Al - High Si alloy*, J. Alloys Compd. 662 (2016) 259–262. doi:10.1016/j.jallcom.2015.11.222.

[83] K.G. Prashanth, S. Scudino, J. Eckert, *Defining the tensile properties of Al-12Si parts produced by selective laser melting*, Acta Mater. 126 (2017) 25–35. doi:10.1016/j.actamat.2016.12.044.

[84] N. Takata, H. Kodaira, K. Sekizawa, A. Suzuki, M. Kobashi, *Change in microstructure of selectively laser melted AlSi10Mg alloy with heat treatments*, Mater. Sci. Eng. A. 704 (2017) 218–228. doi:10.1016/j.msea.2017.08.029.

[85] F. Calignano, G. Cattano, D. Manfredi, *Manufacturing of thin wall*

structures in AlSi10Mg alloy by laser powder bed fusion through process parameters, J. Mater. Process. Technol. 255 (2018) 773–783. doi:10.1016/j.jmatprotec.2018.01.029.

[86] M. Fousová, D. Dvorský, A. Michalcová, D. Vojtěch, *Changes in the microstructure and mechanical properties of additively manufactured AlSi10Mg alloy after exposure to elevated temperatures*, Mater. Charact. 137 (2018) 119–126. doi:10.1016/j.matchar.2018.01.028.

[87] X. Liu, C. Zhao, X. Zhou, Z. Shen, W. Liu, *Microstructure of selective laser melted AlSi10Mg alloy*, Mater. Des. 168 (2019) 107677. doi:10.1016/j.matdes.2019.107677.

[88] E. Louvis, P. Fox, C.J. Sutcliffe, *Selective laser melting of aluminium components*, J. Mater. Process. Technol. 211 (2011) 275–284. doi:10.1016/j.jmatprotec.2010.09.019.

[89] M. Tang, P.C. Pistorius, S. Narra, J.L. Beuth, *Rapid Solidification : Selective Laser Melting of AlSi10Mg*, JOM. 68 (2016) 960–966. doi:10.1007/s11837-015-1763-3.

[90] D.K. Kim, J.H. Hwang, E.Y. Kim, Y.U. Heo, W. Woo, S.H. Choi, *Evaluation of the stress-strain relationship of constituent phases in AlSi10Mg alloy produced by selective laser melting using crystal plasticity FEM*, J. Alloys Compd. 714 (2017) 687–697. doi:10.1016/j.jallcom.2017.04.264.

[91] P. Todeschini, G. Champier, F.H. Samuel, *Production of Al-(12-25) wt% Si alloys by rapid solidification: melt spinning versus centrifugal atomization*, J. Mater. Sci. 27 (1992) 3539–3551. doi:10.1007/BF01151831.

[92] H. Matyja, B.C. Giessen, N.J. Grant, *The effect of cooling rate on the dendrite spacing in splat-cooling Aluminium alloys*, J. Inst. Met. 96 (1968) 30–32.

[93] P.H. Shingu, K. Kobayashi, K. Shimomura, R. Ozaki, *Splat Cooling of Aluminum-Silicon Alloys*, J. Japan Inst. Met. 37 (1973) 433–440.

[94] A. Bendijk, R. Delhez, L. Katgerman, T.H. De Keijser, E.J. Mittemeijer, N.M. Van Der Pers, *Characterization of Al-Si-alloys rapidly quenched from the melt*, J. Mater. Sci. 15 (1980) 2803–2810. doi:10.1007/BF00550549.

[95] R. Delhez, T.H. De Keijser, E.J. Mittemeijer, P. Van Mourik, N.M. Van

Der Pers, L. Katgerman, W.E. Zalm, *Structural inhomogeneities of AlSi alloys rapidly quenched from the melt*, J. Mater. Sci. 17 (1982) 2887-2894. doi:10.1007/BF00644666.

[96] C. Antonione, L. Battezzati, F. Marino, *Structure and stability of rapidly solidified Al-Si based alloys*, J. Mater. Sci. Lett. 5 (1986) 586–588.

[97] I. Yamauchi, I. Ohnaka, S. Kawamoto, T. Fukusako, *Production of Rapidly Solidified Al-Si Alloy Powder by the Rotating-Water-Atomized Process and Its Structure*, Trans. Japan Inst. Met. 27 (1986) 187–194.

[98] M. Gremaud, D.R. Allen, M. Rappaz, J.H. Perepezko, *The development of nucleation controlled microstructures during laser treatment of Al-Si alloys*, Acta Mater. 44 (1996) 2669–2681.

[99] H. Jones, *Formation of metastable crystalline phases in light-metal systems by rapid solidification*, Philos. Mag. B. 61 (1990) 487–509. doi:10.1080/13642819008219289.

[100] M. Pierantoni, M. Gremaud, P. Magnin, D. Stoll, W. Kurz, *The coupled zone of rapidly solidified Al-Si alloys in laser treatment*, Acta Metall. Mater. 40 (1992) 1637–1644.

[101] W. Kurz, R. Trivedi, *Overview No. 87 Solidification microstructures: Recent developments and future directions*, Acta Metall. Mater. 38 (1990) 1–17. doi:10.1016/0956-7151(90)90129-5.

[102] M.J. Aziz, *Model for solute redistribution during rapid solidification*, J. Appl. Phys. 53 (1982) 1158–1168. doi:10.1063/1.329867.

[103] R. Trivedi, W. Kurz, *Dendritic growth*, Int. Mater. Rev. 39 (1994) 49–74. doi:10.1179/imr.1994.39.2.49.

[104] Z. Wang, K.G. Prashanth, S. Scudino, J. He, W.W. Zhang, Y.Y. Li, M. Stoica, G. Vaughan, D.J. Sordelet, J. Eckert, Effect of ball milling on structure and thermal stability of Al84Gd6Ni7Co3 glassy powders, Intermetallics. 46 (2014) 97–102. doi:10.1016/j.intermet.2013.11.005.

[105] A. Aversa, G. Marchese, D. Manfredi, M. Lorusso, F. Calignano, S. Biamino, M. Lombardi, P. Fino, M. Pavese, *Laser Powder Bed Fusion of a High Strength Al-Si-Zn-Mg-Cu Alloy*, Metals (Basel). 8 (2018) 300-311. doi:10.3390/met8050300.

[106] K. Kempen, *Expanding the materials palette for Selective Laser Melting*

of metals, Doctoral Dissertation, Faculty of Engineering Science, KU Leuven, Leuven, The Nederlands, (2015).

[107] M.L. Montero Sistiaga, R. Mertens, B. Vrancken, X. Wang, B. Van Hooreweder, J.P. Kruth, J. Van Humbeeck, *Changing the alloy composition of Al7075 for better processability by selective laser melting*, J. Mater. Process. Technol. 238 (2016) 437–445. doi:10.1016/j.jmatprotec.2016.08.003.

[108] P. Vora, R. Martinez, N. Hopkinson, I. Todd, K. Mumtaz, *Customised Alloy Blends for In-Situ Al339 Alloy Formation Using Anchorless Selective Laser Melting*, Technologies. 5 (2017) 24–36. doi:10.3390/technologies5020024.

[109] A. Aversa, M. Moshiri, E. Librera, M. Hadi, G. Marchese, D. Manfredi, M. Lorusso, F. Calignano, S. Biamino, M. Lombardi, M. Pavese, *Single scan track analyses on aluminium based powders*, J. Mater. Process. Technol. 255 (2018) 17–25. doi:10.1016/j.jmatprotec.2017.11.055.

[110] R. Li, J. Liu, Y. Shi, L. Wang, W. Jiang, *Balling behavior of stainless steel and nickel powder during selective laser melting process*, Int. J. Adv. Manuf. Technol. 59 (2012) 1025–1035. doi:10.1007/s00170-011-3566-1.

[111] D. Gu, Y. Shen, *Balling phenomena during direct laser sintering of multi-component Cu-based metal powder*, J. Alloys Compd. 432 (2007) 163–166. doi:10.1016/j.jallcom.2006.06.011.

[112] D. Gu, Y. Shen, *Balling phenomena in direct laser sintering of stainless steel powder: Metallurgical mechanisms and control methods*, Mater. Des. 30 (2009) 2903–2910. doi:10.1016/j.matdes.2009.01.013.

[113] D. Dai, D. Gu, *Influence of thermodynamics within molten pool on migration and distribution state of reinforcement during selective laser melting of AlN/AlSi10Mg composites*, Int. J. Mach. Tools Manuf. 100 (2016) 14–24. doi:10.1016/j.ijmachtools.2015.10.004.

[114] X.P. Li, C.W. Kang, H. Huang, L.C. Zhang, T.B. Sercombe, *Selective laser melting of an $Al_{86}Ni_6Y_{4.5}Co_2La_{1.5}$ metallic glass: Processing, microstructure evolution and mechanical properties*, Mater. Sci. Eng. A. 606 (2014) 370–379. doi:10.1016/j.msea.2014.03.097.

[115] D.A. Porter, K.E. Easterling, *Diffusional Transformations in Solids*, in: Phase Transform. Met. Alloy., Second Edi, CHAPMAN & HALL, 1992:

pp. 263–378.

[116] P.S. Mohanty, J.E. Gruzleski, *Grain refinement mechanisms of hypoeutectic Al-Si alloys*, Acta Mater. 44 (1996) 3749–3760. doi:10.1016/1359-6454(96)00021-3.

[117] H. Liao, Y. Sun, G. Sun, *Correlation between mechanical properties and amount of dendritic α-Al phase in as-cast near-eutectic Al-11.6% Si alloys modified with strontium*, Mater. Sci. Eng. A. 335 (2002) 62–66. doi:10.1016/S0921-5093(01)01949-9.

[118] S.A. Alkahtani, E.M. Elgallad, M.M. Tash, A.M. Samuel, F.H. Samuel, *Effect of rare earth metals on the microstructure of Al-Si based alloys*, Materials (Basel). 9 (2016). doi:10.3390/ma9010045.

[119] A. Darlapudi, S.D. McDonald, S. Terzi, A. Prasad, M. Felberbaum, D.H. StJohn, *The influence of ternary alloying elements on the Al-Si eutectic microstructure and the Si morphology*, J. Cryst. Growth. 433 (2016) 63-73. doi:10.1016/j.jcrysgro.2015.10.002.

[120] E. Vandersluis, D. Sediako, C. Ravindran, A. Elsayed, G. Byczynski, *Analysis of eutectic silicon modification during solidification of Al-6Si using in-situ neutron diffraction*, J. Alloys Compd. 736 (2018) 172–180. doi:10.1016/j.jallcom.2017.11.118.

[121] A.L. Greer, P.S. Cooper, M.W. Meredith, W. Schneider, P. Schumacher, J.A. Spittle, A. Tronche, *Grain Refinement of Aluminium Alloys by Inoculation*, Adv. Eng. Mater. 5 (2003) 81–91. doi:10.1002/adem.200390013.

[122] A.M.A. Mohamed, F.H. Samuel, A.M. Samuel, H.W. Doty, *Influence of additives on the impact toughness of Al-10.8% Si near-eutectic cast alloys*, Mater. Des. 30 (2009) 4218–4229. doi:10.1016/j.matdes.2009.04.041.

[123] X. Hu, F. Jiang, F. Ai, H. Yan, *Effects of rare earth Er additions on microstructure development and mechanical properties of die-cast ADC12 aluminum alloy*, J. Alloys Compd. 538 (2012) 21–27. doi:10.1016/j.jallcom.2012.05.089.

[124] R.S. Rana, R. Purohit, S. Das, *Reviews on the influences of alloying elements on the microstructure and mechanical properties of aluminum alloys and aluminum alloy composites*, Int. J. Sci. Res. Publ. 2 (2012) 1–7.

[125] M. Timpel, N. Wanderka, R. Grothausmann, J. Banhart, *Distribution of Fe-rich phases in eutectic grains of Sr-modified Al-10 wt.% Si-0.1 wt.% Fe casting alloy*, J. Alloys Compd. 558 (2013) 18–25. doi:10.1016/j.jallcom.2012.12.009.

[126] E. Samuel, B. Golbahar, A.M. Samuel, H.W. Doty, S. Valtierra, F.H. Samuel, *Effect of grain refiner on the tensile and impact properties of Al-Si-Mg cast alloys*, Mater. Des. 56 (2014) 468–479. doi:10.1016/j.matdes.2013.11.058.

[127] Y. Zhang, H. Zheng, Y. Liu, L. Shi, R. Xu, X. Tian, *Cluster-assisted nucleation of silicon phase in hypoeutectic Al-Si alloy with further inoculation*, Acta Mater. 70 (2014) 162–173. doi:10.1016/j.actamat.2014.01.061.

[128] X. Liu, Y. Zhang, B. Beausir, F. Liu, C. Esling, F. Yu, X. Zhao, L. Zuo, *Twin-controlled growth of eutectic Si in unmodified and Sr-modified Al-12.7%Si alloys investigated by SEM/EBSD*, Acta Mater. 97 (2015) 338–347. doi:10.1016/j.actamat.2015.06.041.

[129] P. Mercelis, J. Kruth, *Residual stresses in selective laser sintering and selective laser melting*, Rapid Prototyp. J. 12 (2006) 254–265. doi:10.1108/13552540610707013.

[130] N.S. Rossini, M. Dassisti, K.Y. Benyounis, A.G. Olabi, *Methods of measuring residual stresses in components*, Mater. Des. 35 (2012) 572–588. doi:10.1016/j.matdes.2011.08.022.

[131] M. Shiomi, K. Osakada, K. Nakamura, T. Yamashita, F. Abe, *Residual stress within metallic model made by selective laser melting process*, CIRP Ann. - Manuf. Technol. 53 (2004) 195–198. doi:10.1016/S0007-8506(07)60677-5.

[132] C. Meier, R.W. Penny, Y. Zou, J.S. Gibbs, A.J. Hart, *Thermophysical Phenomena in Metal Additive Manufacturing by Selective Laser Melting: Fundamentals, Modeling, Simulation and Experimentation*, Annu. Rev. Heat Transf. (2017). http://arxiv.org/abs/1709.09510.

[133] A. Salmi, E. Atzeni, *History of residual stresses during the production phases of AlSi10Mg parts processed by powder bed additive manufacturing technology*, Virtual Phys. Prototyp. 12 (2017) 153–160. doi:10.1080/17452759.2017.1310439.

[134] J. Wu, L. Wang, X. An, *Numerical analysis of residual stress evolution*

of AlSi10Mg manufactured by selective laser melting, Optik (Stuttg). 137 (2017) 65–78. doi:10.1016/j.ijleo.2017.02.060.

[135] J.L. Bartlett, X. Li, *An overview of residual stresses in metal powder bed fusion*, Addit. Manuf. 27 (2019) 131–149. doi:10.1016/j.addma.2019.02.020.

[136] J.D. Roehling, W.L. Smith, T.T. Roehling, B. Vrancken, G.M. Guss, J.T. McKeown, M.R. Hill, M.J. Matthews, *Reducing residual stress by selective large-area diode surface heating during laser powder bed fusion additive manufacturing*, Addit. Manuf. 28 (2019) 228–235. doi:10.1016/j.addma.2019.05.009.

[137] L. Zhuo, Z. Wang, H. Zhang, E. Yin, Y. Wang, T. Xu, C. Li, *Effect of post-process heat treatment on microstructure and properties of selective laser melted AlSi10Mg alloy*, Mater. Lett. 234 (2019) 196–200. doi:10.1016/j.matlet.2018.09.109.

[138] M.F. Zaeh, G. Branner, *Investigations on residual stresses and deformations in selective laser melting*, Prod. Eng. Res. Dev. 4 (2010) 35–45. doi:10.1007/s11740-009-0192-y.

[139] C.A. Brice, W.H. Hofmeister, *Determination of bulk residual stresses in electron beam additive-manufactured aluminum*, Metall. Mater. Trans. A Phys. Metall. Mater. Sci. 44 (2013) 5147–5153. doi:10.1007/s11661-013-1847-z.

[140] A. Hussein, L. Hao, C. Yan, R. Everson, *Finite element simulation of the temperature and stress fields in single layers built without-support in selective laser melting*, Mater. Des. 52 (2013) 638–647. doi:10.1016/j.matdes.2013.05.070.

[141] W. Shifeng, L. Shuai, W. Qingsong, C. Yan, Z. Sheng, S. Yusheng, *Effect of molten pool boundaries on the mechanical properties of selective laser melting parts*, J. Mater. Process. Technol. 214 (2014) 2660–2667. doi:10.1016/j.jmatprotec.2014.06.002.

[142] P. Vora, K. Mumtaz, I. Todd, N. Hopkinson, *AlSi12 in-situ alloy formation and residual stress reduction using anchorless selective laser melting*, Addit. Manuf. 7 (2015) 12–19. doi:10.1016/j.addma.2015.06.003.

[143] B. Cheng, S. Shrestha, K. Chou, *Stress and deformation evaluations of scanning strategy effect in selective laser melting*, Addit. Manuf. 12

(2016) 240–251. doi:10.1016/j.addma.2016.05.007.

[144] D.K. Kim, W. Woo, J.H. Hwang, K. An, S.H. Choi, *Stress partitioning behavior of an AlSi10Mg alloy produced by selective laser melting during tensile deformation using in situ neutron diffraction*, J. Alloys Compd. 686 (2016) 281–286. doi:10.1016/j.jallcom.2016.06.011.

[145] D. Dai, D. Gu, R. Poprawe, M. Xia, *Influence of additive multilayer feature on thermodynamics, stress and microstructure development during laser 3D printing of aluminum-based material*, Sci. Bull. 62 (2017) 779–787. doi:10.1016/j.scib.2017.05.007.

[146] L.S. Schadler, C. Galiotis, *Fundamentals and applications of micro Raman spectroscopy to strain measurements in fibre reinforced composites*, Int. Mater. Rev. 40 (1995) 116–134.

[147] I. De Wolf, *Micro-Raman spectroscopy to study local mechanical stress in silicon integrated circuits*, Semicond. Sci. Technol. 11 (1996) 139-154.

[148] S.J. Harris, A. O'Neill, J. Boileau, W. Donlon, X. Su, B.S. Majumdar, *Application of the Raman technique to measure stress states in individual Si particles in a cast Al-Si alloy*, Acta Mater. 55 (2007) 1681-1693. doi:10.1016/j.actamat.2006.10.028.

[149] S. Joseph, S. Kumar, V.S. Bhadram, C. Narayana, *Stress states in individual Si particles of a cast Al-Si alloy: Micro-Raman analysis and microstructure based modeling*, J. Alloys Compd. 625 (2015) 296–308. doi:10.1016/j.jallcom.2014.10.207.

[150] W. Qiu, C.L. Cheng, R.R. Liang, C.W. Zhao, Z.K. Lei, Y.C. Zhao, L.L. Ma, J. Xu, H.J. Fang, Y.L. Kang, *Measurement of residual stress in a multi-layer semiconductor heterostructure by micro-Raman spectroscopy*, Acta Mech. Sin. 32 (2016) 805–812. doi:10.1007/s10409-016-0591-1.

[151] P. Jannotti, G. Subhash, J. Zheng, V. Halls, *Measurement of microscale residual stresses in multi-phase ceramic composites using Raman spectroscopy*, Acta Mater. 129 (2017) 482–491. doi:10.1016/j.actamat.2017.03.015.

[152] E. Anastassakis, A. Pinczuk, E. Burstein, F.H. Pollak, M. Cardona, *Effect of static uniaxial stress on the Raman spectrum of silicon*, Solid State Commun. 8 (1970) 133–138.

[153] E. Anastassakis, E. Liarokapis, *Polycrystalline Si under strain: Elastic*

and lattice-dynamical considerations, J. Appl. Phys. 62 (1987) 3346-3352. doi:10.1063/1.339296.

[154] E. Anastassakis, A. Cantarero, M. Cardona, *Piezo-Raman measurements and anharmonic parameters in silicon and diamond*, Phys. Rev. B. 41 (1990) 7529–7535. doi:10.1103/PhysRevB.41.7529.

[155] Z. Iqbal, S. Veprek, A.P. Webb, P. Capezzuto, *Raman scattering from small particle size polycrystalline silicon*, Solid State Commun. 37 (1981) 993–996. doi:10.1016/0038-1098(81)91202-3.

[156] Y. Kanemitsu, H. Uto, Y. Masumoto, T. Matsumoto, T. Futagi, H. Mimura, *Microstructure and Optical Properties of Free Standing Porous Silicon Films: Size Dependence of Absorption Spectra in Si Nanometer-Sized Crystallites*, Phys. Rev. B. 48 (1993) 2827–2831.

[157] A.P. Meilakhs, S. V. Koniakhin, *New explanation of Raman peak redshift in nanoparticles*, Superlattices Microstruct. 110 (2017) 319–323. doi:10.1016/j.spmi.2017.08.010.

[158] Y. Gao, P. Yin, *Origin of asymmetric broadening of Raman peak profiles in Si nanocrystals*, Sci. Rep. 7 (2017) 43602. doi:10.1038/srep43602.

[159] J. Zi, H. Büscher, C. Falter, W. Ludwig, K. Zhang, X. Xie, *Raman shifts in Si nanocrystals*, Appl. Phys. Lett. 69 (1996) 200–202. doi:10.1063/1.117371.

[160] C. Ossadnik, S. Vepřek, I. Gregora, *Applicability of Raman scattering for the characterization of nanocrystalline silicon*, Thin Solid Films. 337 (1999) 148–151. doi:10.1016/S0040-6090(98)01175-4.

[161] M.N. Islam, S. Kumar, *Influence of crystallite size distribution on the micro-Raman analysis of porous Si*, Appl. Phys. Lett. 78 (2001) 715-717. doi:10.1063/1.1343494.

[162] G. Faraci, S. Gibilisco, P. Russo, A.R. Pennisi, S. La Rosa, *Modified Raman confinement model for Si nanocrystals*, Phys. Rev. B - Condens. Matter Mater. Phys. 73 (2006) 1–4. doi:10.1103/PhysRevB.73.033307.

[163] G. Irmer, *Raman scattering of nanoporous semiconductors*, J. Raman Spectrosc. 38 (2007) 634–646. doi:10.1002/jrs.1703.

[164] P. Alfaro, R. Cisneros, M. Bizarro, M. Cruz-Irisson, C. Wang, *Raman scattering by confined optical phonons in Si and Ge nanostructures*, Nanoscale. 3 (2011) 1246–1251. doi:10.1039/c0nr00623h.

[165] G. Amato, *Sructural and Electrophysical Properties of Porous Silicon*, in: G.S. Korotchenkov (Ed.), Porous Silicon From Form. to Appl., CRC Press, 2016: pp. 155–185.

[166] E.I. Ageev, D. V. Potorochin, D. V. Sachenko, G. V. Odintsova, *Generation of web-like structures and nanoparticles by femtosecond laser ablation of silicon target in ambient air*, Opt. Quantum Electron. 49 (2017) 40. doi:10.1007/s11082-016-0875-5.

[167] I.H. Campbell, P.M. Fauchet, *The Effects of Microcrystal Size and Shape on the One Phonon Raman Spectra of Crystalline Semiconductors*, Solid State Commun. 58 (1986) 739–741.

[168] X. Wang, P. Gong, K.F. Yao, *Mechanical behavior of bulk metallic glass prepared by copper mold casting with reversed pressure*, J. Mater. Process. Technol. 237 (2016) 270–276. doi:10.1016/j.jmatprotec.2016.06.023.

[169] C. Rong, B. Shen, *Nanocrystalline and nanocomposite permanent magnets by melt spinning technique*, Chinese Phys. B. 27 (2018). doi:10.1088/1674-1056/27/11/117502.

[170] A.G. Guy, J.J. Hren, *Elastic Behavior*, in: M. Cohen (Ed.), Elem. Phys. Metall., Third edit, Addison-Wesley Publishing Company, Reading, Massachussets, U.S.A., 1974: pp. 43–73.

[171] S.W. Yang, *Elastic constants of a monocrystalline nickel-base superalloy*, Metall. Trans. A. 16 (1985) 661–665. doi:10.1007/BF02814240.

[172] W.C. Oliver, G.M. Pharr, *An improved technique for determining hardness and elastic modulus using load and displacement sensing indentation experiments*, J. Mater. Res. 7 (1992) 1564–1583.

[173] L.J. Jacob, H.P. Deigner, *Nanoparticles and Nanosized Structures in Diagnostics and Therapy*, in: Precis. Med. Tools Quant. Approaches, Elsevier Inc., 2018: pp. 229–252. doi:10.1016/B978-0-12-805364-5.00010-X.

[174] H. Richter, Z.P. Wang, L. Ley, *The one phonon Raman spectrum in microcrystalline silicon*, Solid State Commun. 39 (1981) 625–629. doi:10.1016/0038-1098(81)90337-9.

[175] N. Brunetto, G. Amato, *A new line shape analysis of Raman emission in porous silicon*, Thin Solid Films. 297 (1997) 122–124.

[176] X. Dong, L. He, G. Mi, P. Li, *Two directional microstructure and effects of nanoscale dispersed Si particles on microhardness and tensile properties of AlSi7Mg melt-spun alloy*, J. Alloys Compd. 618 (2015) 609–614. doi:10.1016/j.jallcom.2014.08.228.

[177] T.G. Holesinger, J.S. Carpenter, T.J. Lienert, B.M. Patterson, P.A. Papin, H. Swenson, N.L. Cordes, *Characterization of an Aluminum Alloy Hemispherical Shell Fabricated via Direct Metal Laser Melting*, Jom. 68 (2016) 1000–1011. doi:10.1007/s11837-015-1798-5.

[178] J.H. Li, M. Albu, F. Hofer, P. Schumacher, *Solute adsorption and entrapment during eutectic Si growth in A-Si-based alloys*, Acta Mater. 83 (2015) 187–202. doi:10.1016/j.actamat.2014.09.040.

[179] R. Trivedi, F. Jin, I.E. Anderson, *Dynamical evolution of microstructure in finely atomized droplets of Al-Si alloys*, Acta Mater. 51 (2003) 289-300. doi:10.1016/S1359-6454(02)00226-4.

[180] H. Rao, S. Giet, K. Yang, X. Wu, C.H.J. Davies, *The influence of processing parameters on aluminium alloy A357 manufactured by Selective Laser Melting*, Mater. Des. 109 (2016) 334–346. doi:10.1016/j.matdes.2016.07.009.

[181] W.B. Pearson, *A handbook of lattice spacings and structures of metals and alloys*, Pergamon Press, 1967.

[182] H. Ichinose, H. Ino, *Lattice imaging analysis and Mössbauer spectroscopy of liquid-quenched Al-Fe alloy*, in: S. Steeb, H. Warlimont (Eds.), Rapidly Quenched Met., Elsevier Science Publishers B.V., 1985: pp. 933–936.

[183] V.A. Lubarda, *On the effective lattice parameter of binary alloys*, Mech. Mater. 35 (2003) 53–68. doi:10.1016/S0167-6636(02)00196-5.

[184] P. Van Mourik, E.J. Mittemeijer, T.H. De Keijser, *On precipitation in rapidly solidified aluminium-silicon alloys*, J. Mater. Sci. 18 (1983) 2706–2720. doi:10.1007/BF00547587.

[185] E. Brosh, G. Makov, R.Z. Shneck, *Application of CALPHAD to high pressures*, Calphad Comput. Coupling Phase Diagrams Thermochem. 31 (2007) 173–185. doi:10.1016/j.calphad.2006.12.008.

[186] P. Van Mourik, T.H. De Keijser, E.J. Mittemeijer, *Excess vacancies in rapidly quenched Aluminium alloys*, in: S. Steeb, H. Warlimont (Eds.), Rapidly Quenched Met., Elsevier Science Publishers B.V., 1985: pp.

899–902.

[187] M.F. Butman, L.S. Kudin, *A mass spectrometric study of thermal dissociation of Mg_2Si*, Russ. J. Phys. Chem. 77 (2003) 537–542.

[188] J. Lacaze, R. Valdes, *CALPHAD-type assessment of the Al-Mg-Si system*, Monatshefte Für Chemie. 136 (2005) 1899–1907. doi:10.1007/s00706-005-0385-9.

[189] H. Feufel, T. Gödecke, H.L. Lukas, F. Sommer, *Investigation of the Al-Mg-Si system by experiments and thermodynamic calculations*, J. Alloys Compd. 247 (1997) 31–42. doi:10.1016/S0925-8388(96)02655-2.

[190] M.J. Aziz, *Disspation-theory treatment of the transition from diffusion-controlled to diffusionless solidification*, Appl. Phys. Lett. 43 (1983) 552–554. doi:10.1063/1.94416.

[191] E. Gebhardt, K. Detering, *Über die Eigenschaften metallischer Schmelen. Die innere Reibung eutektischer Aluminiumlegierungen*, Z. Met. 50 (1959) 379–385.

[192] W. Kurz, D.J. Fisher, *Fundamentals of solidifications*, Third Edit, TRANS TECH PUBLICATIONS, 1992.

[193] M. Petrescu, *Liquid state atomic mobility of Silicon in the unmodified eutectic silumin*, Z. Met. 61 (1970).

[194] M. Keita, S. Steinemann, U. Künzi, *Measurement of Chemical Diffusion Coefficients in Liquid Binary Alloys*, Berichte Der Bunsen-Gesellschaft. 80 (1976) 722–725.

[195] J.T. McKeown, K. Zweiacker, C. Liu, D.R. Coughlin, A.J. Clarke, J.K. Baldwin, J.W. Gibbs, J.D. Roehling, S.D. Imhoff, P.J. Gibbs, D. Tourret, J.M.K. Wiezorek, G.H. Campbell, *Time-Resolved In Situ Measurements During Rapid Alloy Solidification: Experimental Insight for Additive Manufacturing*, JOM. 68 (2016) 985–999. doi:10.1007/s11837-015-1793-x.

[196] A. Aversa, F. Bosio, S. Marola, M. Lorusso, D. Manfredi, L. Battezzati, P. Fino, M. Lombardi, *Laser Single Scan Tracks of New Aluminium Alloys Compositions*, in: Proc. EURO PM2018, 2018: pp. 1–6. https://iris.polito.it/handle/11583/2715552.

[197] F. Bosio, A. Aversa, M. Lorusso, S. Marola, D. Gianoglio, L. Battezzati,

P. Fino, D. Manfredi, M. Lombardi, *A time-saving and cost-effective method to process alloys by Laser Powder Bed Fusion*, Mater. Des. 181 (2019) 107949. doi:10.1016/j.matdes.2019.107949.

[198] X.M. Pan, C. Lin, J.E. Morral, H.D. Brody, *An assessment of thermodynamic data for the liquid phase in the Al-rich corner of the Al-Cu-Si system and its application to the solidification of a 319 alloy*, J. Phase Equilibria Diffus. 26 (2005) 225–233. doi:10.1361/15477030523625.

[199] G. Riontino, A. Zanada, *Coupled formation of hardening particles on pre-precipitates in an Al-Cu-Mg-Si 2014 alloy*, Mater. Lett. 37 (1998) 241–245. doi:10.1016/S0167-577X(98)00099-8.

[200] K.Y. Lee, C.P. Hong, *Stochastic modeling of solidification grain structures of Al-Cu crystalline ribbons in planar flow casting*, ISIJ Int. 37 (1997) 38–46. doi:10.2355/isijinternational.37.38.

[201] S. Fries, H.L. Lukas, *COST 507 Definition of thermochemical and Thermochemical database for light metal alloys*, European Communities, 1998.

[202] S. Cui, I.H. Jung, *Thermodynamic modeling of the quaternary Al-Cu-Mg-Si system*, Calphad Comput. Coupling Phase Diagrams Thermochem. 57 (2017) 1–27. doi:10.1016/j.calphad.2017.02.002.

[203] G.K. Williamson, W.H. Hall, *X-Ray line broadening from filed Aluminium and Wolfram*, Acta Metall. 1 (1953) 22–31. doi:10.1016/0001-6160(53)90006-6.

[204] V.D. Mote, Y. Purushotham, B.N. Dole, *Williamson-Hall analysis in estimation of lattice strain in nanometer-sized ZnO particles*, J. Theor. Appl. Phys. 6 (2012). doi:10.1186/2251-7235-6-6.

[205] A. Guagliardi, N. Masciocchi, *Analisi di Materiali Policristallini Mediante Tecniche di Diffrazione*, Insubria University Press, Varese, 2007.

Appendix

Didactic activities

Presentations

- Oral presentation: *"Additive Manufacturing (AM) as a Rapid Solidification process: a study on Al-Si alloys"* – Marola S. – Annual Metallurgy Group Lab. Meeting – Italy, Vaie (TO), 6th July 2017.

- Oral presentation: *"Additive Manufacturing (AM) as a Rapid Solidification process: a study on Al-Si alloys"* – Silvia Marola, Diego Manfredi, Gianluca Fiore, Marco Gabriele Poletti, Mariangela Lombardi, Paolo Fino, Livio Battezzati – EUROMAT 2017 – Greece, Thessaloniki, 22nd September 2017.

- Poster presentation: *"Development of new Al alloys specifically designed for Additive Manufacturing"* – Silvia Marola, Diego Manfredi, Prashanth Konda Gokuldoss, Jürgen Eckert, Livio Battezzati – ISMANAM 2018 – Italy, Roma, 5th July 2018.

- Oral presentation: *"Development of Al Alloys Specifically Designed for Additive Manufacturing"* – Silvia Marola – Annual Metallurgy Group Lab. Meeting – Italy, Vaie (TO), 13th July 2018.

- Oral presentation: *"Solidificazione rapida di miscele di polveri AlSi10Mg + (Ag, Cu) mediante fusione laser di single trace e melt spinning: relazione con le microstrutture nelle tecnologie additive"* – Silvia Marola, Dario Gianoglio, Livio Battezzati, Massimo Lorusso, Diego Manfredi, Federico Bosio, Alberta Aversa, Mariangela Lombardi – Trentasettesimo Convegno Nazionale AIM – Italy, Bologna, 13th September 2018.

- Oral presentation: *"Rapid solidification processing of Al alloys and Selective Laser Melting"* – Silvia Marola – NIS COLLOQUIUM – Materials

and microstructures in Additive Manufacturing – Torino, Italy, 14th February 2019.

- Oral presentation: *"Residual stresses in AlSi10Mg alloy produced by Additive Manufacturing"* – Silvia Marola – Annual Metallurgy Group Lab. Meeting – Vaie (TO), Italy, 9th July 2019.

- Oral presentation: *"Designing new alloys thought for Laser Powder Bed Fusion process with Melt Spinning and Laser Single Scan Tracks"* – Silvia Marola, Dario Gianoglio, Federico Bosio, Alberta Aversa, Massimo Lorusso, Diego Manfredi, Mariangela Lombardi, Livio Battezzati – EUROMAT 2019 – Stockholm, Sweden, 3rd September 2019.

- Oral presentation: *"Aluminum alloys for Additive Manufacturing"* – Silvia Marola – Metallurgy Seminar – Turin, Italy, 25th November 2019.

PhD Schools attended

- *"Applicazioni della Spettroscopia Raman nelle Scienze Geologiche, Ambientali e Chimiche"*, Turin and Milan (Italy), 7th-11th January 2017.

Classes, Seminars and Conferences attended

Graduate School Courses

- *"Corso di formazione in radioprotezione"*, University of Turin, Department of Physics, February 2017.

- *"Getting the most from our Departmental Facilities"*, University of Turin, Department of Chemistry, March 2017.

- *"The "Energy Principle" in Green Chemistry"*, University of Turin, Department of Chemistry, May 2017.

- *"CrisDi School: Introduction to Crystallography"*, University of Turin, May-June 2017.
- *"CrisDi School: Electron Diffraction"*, University of Turin, May-June 2017.
- *"CrisDi School: X-Ray Diffraction"*, University of Turin, May-June 2017.
- *"CrisDi School: Instrumentation for X-Ray Diffraction"*, University of Turin, May-June 2017.
- *"CrisDi School: X-Ray Diffraction Methods: Single Crystal"*, University of Turin, May-June 2017.
- *"CrisDi School: X-Ray Diffraction Methods: Polycrystalline"*, University of Turin, May-June 2017.
- *"CrisDi School: In situ non-ambient Conditions Single Crystal X-Ray Diffraction Motivation – Single Crystal or Powder Diffraction?"*, University of Turin, May-June 2017.
- *"CrisDi School: The Rietveld Method"*, University of Turin, May-June 2017.
- *"CrisDi School: X-Ray Diffraction Applications on Materials Study"*, University of Turin, May-June 2017.
- *"Additive Metallurgy"*, Associazione Italiana di Metallurgia, Polytechnic of Milan, June 2017.
- *"The Vitreous State"*, University of Turin, Department of Chemistry, October 2017.

Seminars

- *Metallic materials for 3D printing* - Suman Das, Suresh Babu and Moataz Attallah -MRS Bulletin Webinar, 9th November 2016.

- *Structural and surface study of Metal nanoparticles-based catalyst and relative supports* - Andrea Lazzarini - University of Turin, Department of Chemistry, 10th January 2017.

- *In situ operando characterization of zeolite-based catalyst by means of Raman spectroscopy* - Matteo Signorile - University of Turin, Department of Chemistry, 10th January 2017.

- *Mixed Li-based Complex Hydrides for Energy Storage* - Anna Wolczyk - University of Turin, Department of Chemistry, 15th February 2017.

- *Heat effects of hydrogen interaction with Cu-Ni and Pt-NiZr metal/oxides systems* - Emanuele F. Marano - University of Turin, Department of Chemistry, 2nd March 2017.

- *Development of new high entropy alloys at the University of Turin* - Marco Gabriele Poletti - University of Turin, Department of Chemistry, 28th April 2017.

- *Experimental investigation and thermodynamic modelling of mixtures of borohydrides for energy storage* - Erika M. Dematteis - University of Turin, Department of Chemistry, 9th June 2017.

- Metallurgy Group Lab. Meeting, Italy, Vaie (TO), 6th July 2017.

- *Hydrogen as alternative fuel for environmental performance improvement* - Nadia Belmonte - University of Turin, Department of Chemistry, 24th July 2017.

- PhD Day, 2nd year PhD presentations (XXXI Cycle) – University of Turin, Department of Chemistry, 25th September 2017.

- *Biosensor and catalysis: applications of nanoporous gold – Federico Scaglione* – University of Turin, Department of Chemistry, 10th November 2017.

- *Gender equality: don't change women, change the system* – Silvia Casassa, Paola Rizzi, Erika Michela Dematteis – University of Turin, Department of Chemistry, 24th November 2017.

- *Effect of different processing routes on the properties of thermoelectric materials* – Francesco Aversano – University of Turin, Department of Chemistry, 19th January 2018.

- *Semiconducting oxides modification for photocatalytic applications* – Valeria Polliotto – University of Turin, Department of Chemistry, 30th January 2018.

- *Thermodynamics of Boron-based Complex Hydrides for Energy Storage* – Erika Michela Dematteis – University of Turin, Department of Chemistry, 19th October 2018.

- *Aluminum alloys for additive manufacturing and their thermal treatments* – Dario Gianoglio – University of Turin, Department of Chemistry, 18th January 2019.

- *Synthesis and Characterization of Ullmanite compounds* – Francesco Aversano – University of Turin, Department of Chemistry, 8th February 2019.

- *Enhancing the success in electrolytic preparation processes* – Holger Schuarr – Struers GmbH Webinar, 12th February 2019.

- *Selected metallic materials and technologies for aerospace industry* – Maciej Motyka – University of Turin, Department of Chemistry, 5th April 2019.

- *Low dimensional dense and nanostructured Fe-based alloys* – Matteo Cialone – University of Turin, Department of Chemistry, 12th April 2019.

- PhD Day, 2nd year PhD presentations (XXXIII Cycle) – University of Turin, Department of Chemistry, 26-27th September 2019.

- *Complex hydrides as solid-state electrolyte for Li-ion batteries* – Valerio Gulino – University of Turin, Department of Chemistry, 17th October 2019.

- *Metal powder for Additive Manufacturing* – Volker Uhlenwinkel – University of Turin, Department of Chemistry, 15th November 2019.

- *Origin of the photoactivity and role of defectivity in pure and mixed ZnO based systems* – Erik Cerrato – University of Turin, Department of Chemistry, 16th December 2019.

Conferences and Workshops

- *Il Trasferimento Tecnologico: un'opportunità per l'evoluzione della propria ricerca (Start-up)* - University of Turin, Doctoral Schools, 23rd September 2016.

- *Workshop sul trasferimento di conoscenze per dottorandi* - University of Turin, Doctoral Schools, 14th December 2016.

- Metallurgy Group Lab. Meeting, Italy, Vaie (TO), 6th July 2017.

- EUROMAT 2017 – European Congress and Exhibition on Advanced Materials and Processes – Greece, Thessaloniki, 17th-22nd September 2017.

- *Recent advances in biosensor technologies* – University of Turin & NIS, 22nd November 2017.

- ISMANAM 2018 – 25th International Symposium on Metastable, Amorphous and Nanostructured Materials – Italy, Roma, 1st-6th July 2018.

- Metallurgy Group Lab. Meeting, Italy, Vaie (TO), 13th July 2018.

- Trentasettesimo convegno nazionale AIM, Italy, Bologna, 12th-14th September 2018.

- PhD Workshop XXXII – University of Turin, Department of Chemistry, 24th-25th September 2018.

- *Additive Manufacturing e controlli non distruttivi* – Associazione Italiana Prove non Distruttive – Politecnico di Torino, 21st-22nd November 2018.

- *Le potenzialità del dottorato fuori dall'accademia* – University of Turin, Department of Chemistry, 18th December 2018.

- *Materials and microstructures in Additive Manufacturing* – NIS Colloquium and STAMP Dissemination – University of Turin, Department of Chemistry, 14th February 2019.

- Metallurgy Group Lab. Meeting, Italy, Vaie (TO), 9th July 2019.

- *Giornate del CrisDi: X-ray Powder Diffraction: a useful tool for Chemistry and Material Science* – Domenica Marabello – University of Turin, Department of Chemistry, 28th February 2019.

- EUROMAT 2019 – European Congress and Exhibition on Advanced Materials and Processes – Stockholm, Sweden, 1st-5th September 2019.

Didactic activities

- Laboratory assistance for the course “Materiali Metallici” of the bachelor degree in Scienza e Tecnologia dei Materiali (Prof. Paola Rizzi), Turin, 14th-22nd May 2018.

- Laboratory assistance for the course “Metallurgia” of the master degree in Chimica Industriale (Dott. Federico Scaglione), 14th-24th January 2019.

Periods abroad

- 31/01/2018-30/04/2018 –Montanuniversität of Leoben, Department of Materials Physics & Erich Schmid Institute of Materials Science, Austrian Academy of Sciences – Austria – Supervisor: Prof. Jürgen Eckert and Dr. Prashanth Konda Gokuldoss.

  Activities:

  - FESEM and EBSD measurements were performed on AlSi10Mg samples produced by L-PBF and MS in Turin.
  - Acquired knowledge on residual stress measurements determination through XRD; trials were performed on L-PBF and MS AlSi10Mg samples.
  - Acquired knowledge on how to prepare metallic samples for TEM by polishing, dimpling and ion milling.
  - TEM observations were carried out on the samples of AlSi10Mg produced by L-PBF and MS.
  - The applicability of some Al-Ni-Sm-Co metallic glasses with varying composition to the production of bulk objects through L-PBF was evaluated producing ribbons by MS. Characterization both in as spun conditions and after thermal annealing was carried out through XRD, DSC and nanoindentation tests.

Publications

- Silvia Marola, Diego Manfredi, Gianluca Fiore, Marco Gabriele Poletti, Mariangela Lombardi, Paolo Fino, Livio Battezzati "A comparison of Rapid Solidification and Selective Laser Melting (SLM) of Al-Si alloys", *Journal of Alloys and Compounds* **2018**, 742, 271-279.

- A. Aversa, F. Bosio, S. Marola, M. Lorusso, D. Manfredi, L. Battezzati, P. Fino, M. Lombardi, "Laser Single Scan Tracks Of New Aluminium Alloys Compositions", *Euro PM2018 Proceedings*, EPMA, Shewsbury, U.K. **2018**.

- F. Bosio, A. Aversa, M. Lorusso, S. Marola, D. Gianoglio, L. Battezzati, P. Fino, D. Manfredi, M. Lombardi, "A time-saving and cost-effective method to process alloys by Laser Powder Bed Fusion", *Materials & Design*, **2019**, 181, 107949.

- Silvia Marola, Dario Gianoglio, Federico Bosio, Alberta Aversa, Massimo Lorusso, Diego Manfredi, Mariangela Lombardi, Livio Battezzati "Alloying AlSi10Mg and Cu powders in Laser Single Scan Tracks, Melt Spinning and, Laser Powder Bed Fusion", *Journal of Alloys and Compounds,* **2020**, 821, 153538.

- Dario Gianoglio, Silvia Marola, Livio Battezzati, Alberta Aversa, Federico Bosio, Mariangela Lombardi, Diego Manfredi, Massimo Lorusso "Banded microstructures in rapidly solidified Al-3 wt% Er", submitted to *Intermetallics* **December 2019**.